On the Role of Pre-Pulses in Laser-Irradiation of Isolated Micro-Spheres at Relativistic Intensities

Felix Balling

München 2024

On the Role of Pre-Pulses in Laser-Irradiation of Isolated Micro-Spheres at Relativistic Intensities

DISSERTATION

an der Fakultät für Physik der

Ludwig-Maximilians-Universität München

vorgelegt von

Felix Balling

geboren in Weilheim i. OB

München, den 27. August 2024

Erstgutachter: Prof. Dr. Jörg Schreiber
Zweitgutachter: Prof. Dr. Ulrich Schramm
Tag der mündlichen Prüfung: 25. November 2024

Zusammenfassung

Die Beschleunigung von Teilchen in einem Plasma, durch einen ultrastarken Laserpuls, soll die nächste Generation von Teilchenbeschleunigern antreiben. Ein Schlüsselelement hierbei ist das Target, auf das der Laserpuls fokussiert wird und in dem die Ionen beschleunigt werden. Insbesondere isolierte massenlimitierte Targets mit einer Größe kleiner als der Laserfokus können hoch effiziente volumetrische Beschleunigungsregime erreichen.

In dieser Arbeit wird der Effekt von Vorpulsen auf die Plasmabedingungen kurz vor Beginn des Beschleunigungsprozesses untersucht. Motiviert durch frühere Arbeiten an verschiedenen nationalen und internationalen Forschungszentren wurden Experimente am ATLAS-3000 Laser in CALA durchgeführt. Ziel dieser Experimente war es festzustellen, ob ein zeitlicher Laser-Kontrast mit einem kurzen Vorpuls und einer moderat langen und intensiven ansteigenden Flanke vor dem Hauptpuls ausreichend und möglicherweise sogar vorteilhaft für die Beschleunigung von Protonen aus isolierten Polystyrol-Mikrokugeln ist. Durch die Analyse des transmittierten Laserlichts wurde die Position des Targets relativ zum Laserfokus rekonstruiert. Da dies eine systematische Verschiebung des Targets zu Bereichen niedrigerer Intensität offenbart, ist die Interpretation der Ergebnisse mehrdeutig und erfordert weitere Untersuchungen.

Zu diesem Zweck wurde ein einfaches Modell entwickelt, das numerisch gelöst werden kann, um die Plasmabedingungen zum Zeitpunkt des Hauptpulses aus dem experimentellen Laser-Kontrast zu berechnen. Dieses Modell wurde zur Verifizierung mit detaillierten radio-hydrodynamischen Simulationen verglichen. Während die Simulationen einige Merkmale offenbaren, die nicht im Modell enthalten sind, wie zum Beispiel eine prominente Schockwelle, die durch das Target propagiert, ist die Übereinstimmung bei gemittelten Dichten und Temperaturen bemerkenswert.

Auf Grundlage des Modells und der Simulationen wird geschlossen, dass die experimentell beobachtete Verschiebung zwischen Laserfokus und Target auf systematische Fehler zurückzuführen ist und der zeitliche Kontrast des ATLAS-3000 nahezu ideal zur Beschleunigung von Protonen aus diesen Targets geeignet ist. Weiterhin wird das Modell auf andere Lasersysteme angewandt und allgemeine Grenzen für den Laser-Kontrast für effiziente Beschleunigung aus isolierten Zielen werden extrahiert.

Abstract

The acceleration of particle in a plasma driven by an ultra-intense laser pulse holds promise to power the next generation of particle accelerators. A key element hereby is the target onto which the laser pulse is focused and from which the ions are accelerated. In particular isolated mass-limited targets with a size smaller than the laser focus can achieve highly efficient volumetric acceleration regimes.

In this thesis the effect of pre-pulses on the plasma properties just before the beginning of the acceleration process is investigated. Motivated by previous work at multiple national and international research facilities, experiments were performed at the ATLAS-3000 laser at CALA. The goal of these experiments was to determine whether a temporal laser contrast with a short pre-pulse and moderately long and intense rising edge before the main pulse is sufficient and possibly even beneficial for proton acceleration from isolated polystyrene micro-spheres. From the analysis of the transmitted laser light the position of the target with respect to the laser focus was reconstructed. As this reveals a systematic displacement of the target to areas of lower intensity, the interpretation of the results is ambiguous and requires further investigation. To this end a simple model was developed, which can be solved numerically to calculate the target conditions at the time of the main pulse from the experimental laser contrast. This model was compared to detailed radio-hydrodynamic simulations for verification. While the simulations reveal some features which are not included in the model, such as a prominent shock wave traveling through the target, the agreement on averaged densities and temperatures is remarkable.

Informed by the model and simulations, it is concluded that the experimentally observed offset between laser focus and target is due to systematic errors. The temporal contrast of the ATLAS-3000 is in fact expected to result in near-ideal conditions for proton acceleration from these targets. Further, the model is applied to other laser systems and general limits on the laser contrast for efficient acceleration from isolated targets are extracted.

Contents

List of Figures

List of Tables

Abbreviations

ASE Amplified Spontaneous Emission

ATI Above Threshold Ionization

ATLAS Advanced Titanium-sapphire LASer

ATLAS-3000 Advanced Titanium-sapphire LASer 3000

BSI Barrier Suppression Ionization

CALA Centre for Advanced Laser Applications

CMOS Complementary Metal-Oxide-Semiconductor

CPA Chirped Pulse Amplification

CSA Collisionless Shock Acceleration

CW Continuous Wave

DRACO Dresden Laser Acceleration Source

FFT Fast-Fourier-Transform

FI Field Ionization

FROG Frequency-Resolved Optical Gating

FWHM Full-Width at Half-Maximum

GSI Helmholtzzentrum für Schwerionenforschung

JETi JEnaer Ti-saphir laser

LION Laser-driven ION

LPA Laser-driven Plasma Acceleration

LTE Local Thermal Equilibrium

MLTs Mass-Limited Targets

MPI Multi-Photon Ionization

OAP Off-Axis Parabolic mirror

OPA Optical Parametric Amplification

PFS-pro Petawatt Field Sythesiser

PHELIX Petawatt Hoch-Energie Laser für SchwerIoneneXperimente

PIC Particle-In-Cell

PMT Photo-Multiplier Tube

PS Polystyrene

PSF Point-Spread-Function

PSD Position-Sensitive Diode

RALEF Radiative Arbitrary Lagrange-Eulerian Fluid dynamics

RF Radio Frequency

RHD Radiation-Hydro-Dynamic

RPA Radiation Pressure Acceleration

SFG Sum-Frequency Generation

SHG Second Harmonic Generation

SPIDER Spectral Phase Interferometry for Direct Electric-field Reconstruction

SRSI Self-Referenced Spectral Interferometry

SSI Solid-State Ionization

THG Third Harmonic Generation

Ti:Sa Titanium:Sapphire

TNSA Target Normal Sheath Acceleration

TOAC Third-Order Auto Correlator

TPW Texas PetaWatt

WASP Wide Angle SPectrometer

XPW Cross-Polarized Wave

ZEUS Zinths Extremely Useful Superlaser

1. Introduction

1.1. Particle Acceleration with High-Power Lasers

Particle accelerators based on Radio Frequency (RF) fields have revolutionized science and enabled new technologies from material manufacturing to cancer therapy. The acceleration typically takes place inside microwave cavities made of copper. This limits the field gradients available for the acceleration by the breakdown of the cavity material. Therefore, acceleration to higher particle energies requires ever larger accelerators, with the biggest scientific accelerators, such are CERN, SLAC, or the Euopean-XFEL, already spanning multiple kilometers. To overcome this limitation, acceleration inside a plasma has been proposed [1]. As the plasma is already broken down into its constituents, it can sustain much larger electric fields and thereby reduce the necessary acceleration distances by multiple orders of magnitude.

Simultaneously with the fast development of new laser technologies, the field of laser-driven particle acceleration has grown rapidly in the last decades. New ultra-short (few fs) pulse laser technology provides ever higher peak power up to the multi-PW range and increasing repetition rates in the Hz regime [2–5].

The interaction of these lasers with the respective targets depends strongly on the density of the created plasma. The relevant density scale is the critical density, at which the oscillations of the laser field with wavelength λ_L are in resonance with the plasma oscillations. For densities lower than the critical density the laser can propagate through the target, at higher densities it is reflected or absorbed and can not propagate. The critical density can be calculated as

$$n_c = 1.1 \cdot 10^{21}\,\mathrm{cm}^{-3} \left(\frac{\lambda_\mathrm{L}^2}{\mu\mathrm{m}^2}\right). \tag{1.1}$$

Utilizing the powerful drivers, many different branches and applications of laser-driven particle accelerators have developed. A first classification can be made by the primary particle that is created. Electron acceleration can occur efficiently at low density targets, such as gas jets or capillary discharges, in the laser-wakefield regime [1, 6–9]. The most simple mechanism to create X-Ray radiation is to directly irradiate a high-Z solid

material with the laser and use the typical Bremsstrahlung and line radiation spectrum. Monochromatic and potentially coherent X-ray sources can be produced from accelerated electrons by betatron oscillations in the plasma wave [10, 11], in magnetic undulators [12], or by collision with a counter-propagating laser pulse via Thomson scattering [13–15]. Heavy and light ions are typically accelerated from thin solid targets or foams [16–21].

For the different particle species and acceleration modalities many potential applications are envisioned. Laser-driven electron sources could provide compact drivers for free-electron lasers [22] or electron-positron colliders. X-rays created from these electron bunches are expected to provide imaging with unprecedented temporal and spatial resolution [23–28]. At very high energies and fluence these X-rays can also be used to investigate fundamental QED effects [29]. Energetic ions are promising for bio-medical applications [30–33], material science and radiography [34–37], warm dense matter research [38, 39], injectors for conventional accelerators [40], and inertial confinement fusion [41–44]. Neutrons, which are created either directly in a suitable target [45] or a subsequent converter [46–48], could enable mobile non-invasive imaging of solid structures like bridges, buildings or shipping containers [49, 50].

1.1.1. Ion Acceleration

The acceleration of ions in a plasma has been investigated since the 1990s. Initially, the expansion of a plasma from a solid transitioned into the Target Normal Sheath Acceleration (TNSA) regime [19, 20]. Hereby, a thin (few µm) foil target is irradiated with a highly energetic laser pulse. On the front side the laser heats the plasma electrons to high temperatures. The hot electrons propagate through the otherwise undisturbed target to the back side and form a sheath there. This structure is maintained by the charge separation field between the electrons and the plasma ions, the bulk of which remains stationary because of their higher mass. The separation field pulls the electrons back, so that a dense electron layer forms at the return point. This quasi-stationary field reaches MV/µm strength and ionizes ions from the top layer of the target back, which are subsequently accelerated by the field. Due to the high charge-to-mass ratio, protons, which are present as surface contamination on any target, are preferentially accelerated. The spectrum of the accelerated ions has a thermal shape with an exponential decay towards higher energies up to a cut-off, which is defined by the separation field strength and scales with the square root of the laser intensity [51]. As the laser is coupled to the accelerating field by the rear side sheath, the emission is always normal to the target plane and depends only weakly on the laser angle of incidence. The regime is very robust

and easily accessible with the first generation of PW-class laser systems, which are based on glass amplifiers and deliver $\sim 1\,\mathrm{ps}$ long pulses with hundreds of joules pulse energy.

Other acceleration mechanism developed from TNSA with different target and laser properties. The goal was to achieve ion bunch properties which differ from the TNSA case. For example could a peaked spectrum increase the conversion efficiency when requiring a particular ion energy e.g. for ion therapy or transport through an energy selective beamline. Also a stronger scaling than with the square root of the intensity for the cut-off would allow to reach higher maximum ion energies, which are required for some applications to have sufficient penetration depth.

For example Radiation Pressure Acceleration (RPA) [52, 53] or Collisionless Shock Acceleration (CSA) [54–56] can result in peaked ion spectra, but have higher demands on the laser parameters. In particular the temporal shape and contrast of the laser pulse has to be well controlled while at the same time high intensities are required. Because of these requirements experiments have so far not been able to match the expectations set by simulations.

An easier accessible regime is at the relativistic transparency threshold [44, 57–60]. Here the target is expanded by the leading edge of the laser pulse to reduce the electron density to the relativistic critical density. This means the laser can propagate deeper into the target than in the TNSA case and the electron bulk is heated instead of just the surface layer. This dramatically increases the coupling efficiency of the laser into hot electrons and thereby improves the ion acceleration.

Combining contributions from different acceleration mechanisms, it was first possible to reach proton energies up to 150 MeV using laser pulses with 22.4 J energy in 30 fs focused to $6.5 \cdot 10^{21}\,\mathrm{W/cm^2}$ peak intensity [61]. This is the first experimental demonstration of proton energies beyond the 100 MeV barrier [62, 63], and is within reach of the ∼200 MeV required for cancer treatment in humans.

1.1.2. Target Geometry

The targets typically used for laser driven ion acceleration are thin foils, either made of polymers or metals, due to the ease in handling and well understood physics. However, other target geometries have also been investigated in simulations and experiments.

A group of targets of particular interest are so called Mass-Limited Targets (MLTs). The volume of these targets is of the order of the focus and the target is (partially) isolated. This simplifies the physical picture, as only the peak intensity of the laser interacts with the target and no transfer of heat or particles with non-irradiated parts of

the target can occur.

Target systems implementing MLTs include liquid and cryogenic jets, droplets [64–66], and small foils held on thin structures [67, 68]. A system available to provide truly isolated targets with sizes smaller than the laser focus is a Paul trap [69, 70]. The fact that it can provide spherical targets smaller than the laser focus is what makes this system unique.

Here charged targets are freely levitated inside oscillating electric quadrupole fields. This allows ion acceleration from a wide range of otherwise unavailable target parameters [69]. While it is in principle possible to use non-spherical targets, only spherical targets will be considered in the following, as they are more convenient experimentally and the spherical geometry is a simpler case study.

Possible mechanisms for ion acceleration from MLTs are sketched in Figure 1.1. On the top the interaction geometry of the laser with the target is schematically shown. The target is a few times smaller than the laser spot size and the laser impinges on the target from the left. In the most rudimentary case, a short laser pulse strips a large number of electrons from the plasma leaving a positively charge spherical plasma (**a**). This then rapidly expands symmetrically in all directions due to the Coulomb forces, giving it the name Coulomb explosion. If the laser does not strip a significant number of electrons from the target but mainly heats them, they will expand away from the slowly moving ion bulk until they are stopped by the charge separation field (**b**). Ions are then accelerated normal to the target surface similar to the case of TNSA in planar geometry. Driven by the radiation pressure of the laser pulse a shock will be launched into the target (**c**). Ions downstream of the shock can reflect off of it and be accelerated to twice the shock velocity. In an experiment the mechanisms overlap and for example a shock is launched and the sheath of hot electrons is offset towards the target rear by the radiation pressure (**d**). If they initial spherical symmetry is broken, e.g. by a shock, the emission can become directed into the forward direction.

One promising acceleration mechanism is a combination of enhanced volumetric heating of electrons and a shock driven by the laser, creating a directed acceleration with low divergence in the laser direction [71, 72]. Such properties could be of particular interest for injection into magnetic ion optics, as are often employed in radiation therapy for beam guiding.

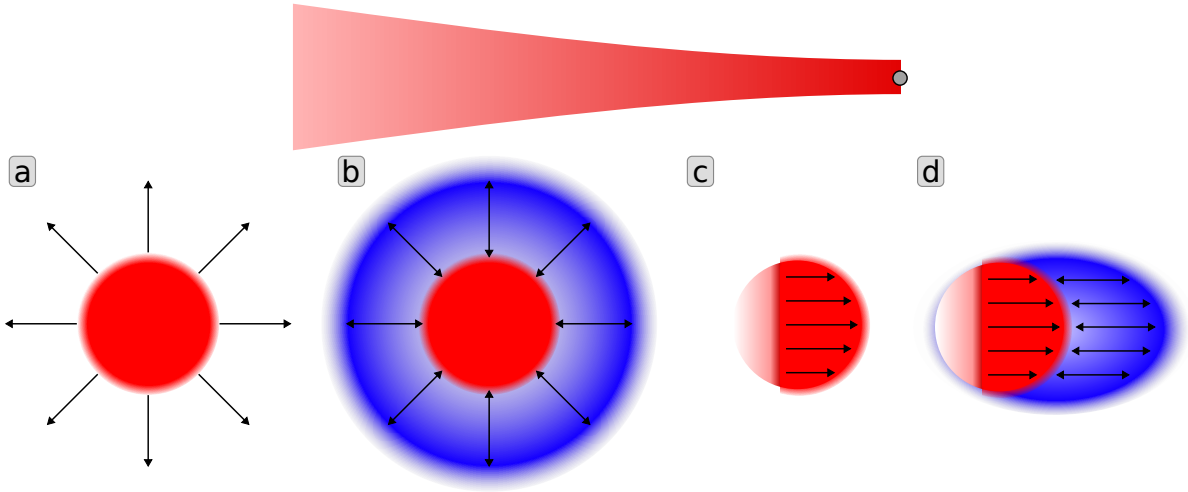

Figure 1.1.: **Acceleration Mechanisms in MLTs**
Schematic illustration of Coulomb explosion (**a**), TNSA equivalent (**b**), shock-driven (**c**), and combined (**d**) ion acceleration mechanisms in MLTs. The top illustrates the laser impinging on the target, with a focus larger than the target cross-section.

1.2. Mass Limited Targets for Laser-Driven Ion Acceleration

Such mass limited targets, in particular freely levitating in a Paul trap, have been investigated for more than a decade [69, 71–75]. During this time, experiments have been performed at a number of national and international laser facilities with a wide range of laser and target parameters. The laser systems differ mainly in their temporal pulse shape, which includes the duration of the main pulse as well as the temporal contrast on a timescale of hundreds of ps, which is shown in Figure 1.2.

1.2.1. Previous Work

While the first experiments demonstrated the fundamental usability of the system and highlighted the wide range of accessible target parameters [69, 73], in particular the three most recent campaigns at Petawatt Hoch-Energie Laser für SchwerIoneneXperimente (PHELIX), Zinths Extremely Useful Superlaser (ZEUS), and JEnaer Ti-saphir laser (JETi) are of interest for the optimization of the acceleration process. The results of these experiments are therefore summarized in the following, before conclusions are drawn from their observations to the design of further experiments.

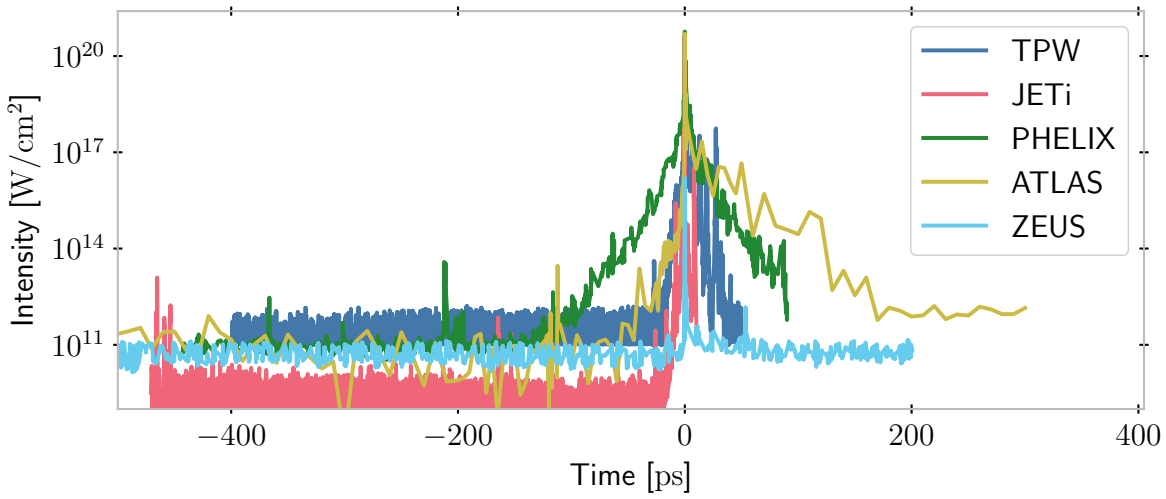

Figure 1.2.: **Temporal Contrast Comparison**
Temporal contrast of the laser systems at which experiments with the PaulTrap were performed. TPW: Texas PetaWatt [76], JETi: JEnaer Ti-saphir laser [71], PHELIX: Petawatt Hoch-Energie Laser für SchwerIoneneXperimente [74], ATLAS: Advanced Ti:saphir LASer, ZEUS: Zinths Extremely Useful Superlaser [75]

PHELIX

One of the first large champaigns was performed at the PHELIX at the Helmholtzzentrum für Schwerionenforschung (GSI) [74]. In this experiment, it was first discovered that the transmitted laser light can be a powerful diagnostic of the plasma conditions at the time of the main pulse (see Figure 1.3) in a variation of inline holography. The observed ring-like diffraction pattern is characteristic of the plasma density distribution and can be compared to numerical calculations for an assumed density model, in this case a Gaussian distribution. Spatial extent and absolute density change the spacing and modulation depth of the rings. From this the peak plasma density was derived as slightly below the critical density ($0.5\,n_c$-$1\,n_c$) around 500 fs prior to the main pulse. The acceleration mechanism is then a volumetric acceleration, so the laser pulse interacts with a large part of the target volume. Due to the long pulse duration of the PHELIX, the target was already depleted of electrons when the intensity peak arrived the acceleration was only driven during the early part of the laser pulse.

These conclusions were underlaid by Particle-In-Cell (PIC) simulations, which showed good agreement with the experimental findings. Of particular interest was the fact, that the acceleration was moderately directed and the spectrum showed a clearly peaked structure. It was extrapolated that maintaining the acceleration over the whole pulse

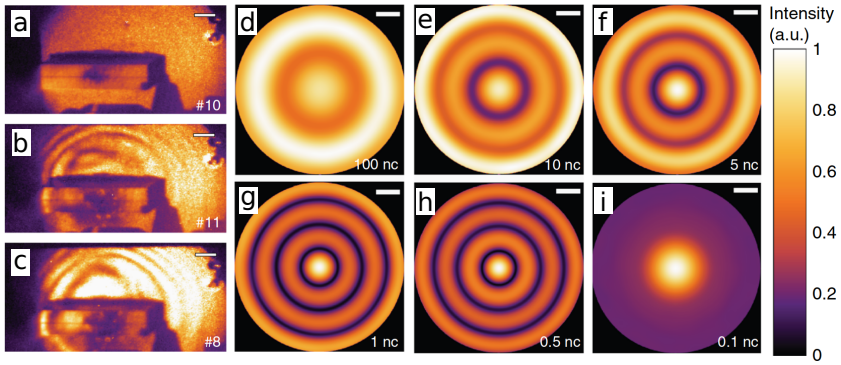

Figure 1.3.: **Transmission Images at PHELIX**
Transmission images for an empty shot (a) and two target shots (b, c) recorded during the experiments at PHELIX. The right side shows simulated transmission images for Gaussian plasma density distributions with different central densities (d-i). Figure copied from Ref. [74] under CC-BY 4.0.

duration could result in protons with a peaked spectrum with more than 150 MeV kinetic energy.

This experiment first triggered interest in the expansion of the plasma prior to the main pulse and potential optimization of the acceleration by tailoring of the plasma conditions. The PHELIX temporal contrast (Figure 1.2) exhibits a short pre-pulse ~ 210 ps prior to the main pulse, which is likely to ionize a target into the plasma state. Already 110 ps prior to the main pulse the rising edge of the pulse begins with an exponential increase of laser intensity. This means a significant amount of energy arrives at the target before the peak intensity, which can drive plasma dynamics that change the density distribution.

In this case the expansion of the plasma already reduced the density to such a low value, that only a small part of the laser energy could be used for the acceleration. However, the peaked spectral features and high stability demonstrated the potential to shape the density distribution of mass limited targets to optimize ion acceleration.

ZEUS

Follow up experiments to investigate the plasma expansion triggered by short pulses were performed at the 3 TW laser system ZEUS at the Centre for Advanced Laser Applications (CALA) [75]. Here a pump-probe setup was used to probe the plasma at different times after the interaction with a moderately intense ($I \approx 10^{16}\,\mathrm{W/cm^2}$) short pulse, like it might occur as a pre-pulse at a PW class laser. As only low intensity arrived at the target before the main pulse (cp. Figure 1.2), it is expected that the interaction is strongly dominated by the main pulse without significant pre-expansion.

The plasma at the time of the interaction with the pump pulse was diagnosed by the diffraction patterns in the transmitted laser profile, similar to the transmission analysis performed at PHELIX. The technique was improved by use of more efficient methods for the pulse propagation calculation and a more sophisticated plasma model. This model incorporates a symmetric shock that is driven by the pulse. A single Gaussian distribution, which was used as density model in the PHELIX analysis, was here not able to reproduce the observed patterns accurately. The addition of the shock increased the area in which the plasma density remained above the critical density, resulting in different diffraction patterns. This highlights the high sensitivity of the method to the plasma density distribution.

Probing was realized by an other inline holographic setup, where the diffraction pattern of the probe pulse was recorded on a screen. This diffraction pattern was evaluated by forward simulation of the probe pulse through the plasma, the same way that the transmission images were evaluated. It revealed that, while the shock is relevant for times shortly after the interaction with the pump pulse, at later times the plasma can be well approximated by a three dimensional Gaussian distribution.

From the retrieved density distributions at different times after the pump pulse, the expansion velocity could be calculated. It could also be seen that the plasma only showed a small degree of asymmetry and mostly expanded spherically in all directions.

The experimental observations were affirmed by Radiation-Hydro-Dynamic (RHD) simulations of the interaction and subsequent expansion.

JETi

Taking the results from ZEUS as input, ion acceleration experiments with dedicated pre expansion were first performed at the JETi [71, 72]. The JETi is a 200 TW system with very clean temporal contrast due to an inline plasma mirror (see Figure 1.2). It is focused to 2 µm diameter, resulting in a peak intensity of $2.8 \cdot 10^{20}\,\mathrm{W/cm^2}$. A dedicated pre-pulse was introduced downstream of the plasma mirror and the timing of the pre-pulse scanned for optimum ion acceleration performance.

It was shown that in the optimum expansion case, the maximum proton energies could be increased by up to a factor of 2 (see Figure 1.4), while too much expansion led to a significant reduction of the energy cut-off, as well as particle numbers. Optimum proton acceleration was achieved, when the plasma expanded to just above the relativistic critical density γn_c. For an intensity of $I \sim 10^{21}\,\mathrm{W/cm^2}$ the relativistic factor is $\gamma \sim 15$. Scaling the accelerations in simulations to PW-level laser systems, which deliver a few

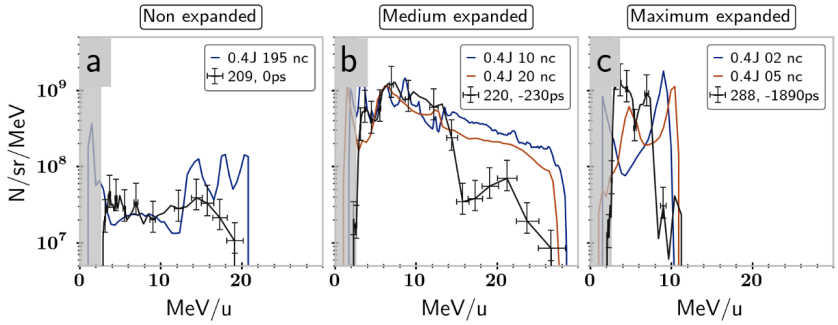

Figure 1.4.: **Proton Spectra at JETi**
Experimental (black lines and symbols) and simulated (colored lines) proton spectra for different levels of pre-expansion (**a**, **b**, **c**) from the JETi experiment. The optimum expansion is shown in the middle, no and too much expansion on the left and right respectively. Figure adapted with permission from Ref. [71, Fig. 5.1].

10 J energy on target, maximum proton energies in excess of 150 MeV can be expected. The experiments impressively demonstrate the potential of deliberately pre-expanding the plasma to reach the relativistic critical density at the time of the intensity peak. The underlying acceleration mechanism was investigated in PIC simulations. In the initial phase the ions are accelerated by a shock driven by radiation and ablation pressure. During this time electrons are leaving the target to the back and are transversely confined by the ponderomotive potential of the laser. This creates a charge separation field which can store some percent of the laser pulse energy. After the laser peak has passed, this separation field discharges, further accelerating the ions in the quasi-static potential.

While the process can generate high proton energies, in the experiments significant shot-to-shot fluctuations were observed, mainly due to jitter in the overlap between target and laser focus.

The use of plasma mirror and pick-off for the pre-pulse reduced the laser energy on target significantly. To reach the peak intensity of $2.8 \cdot 10^{20}\,\mathrm{W/cm^2}$, 4 J laser energy before compression were necessary. In a perfect Gaussian pulse in temporal and spatial domain, this would require only 0.4 J.

1.2.2. Conclusions for Further Experiments

The previous experiments contributed important experience for the design of future experiments.

The campaign at PHELIX first demonstrated the diagnostic potential that lies in

measuring the the transmitted laser beam profile. As confirmed in the ZEUS experiments, this diagnostic allows to gain insight into the plasma conditions at the time of the main pulse without additional probe setups.

Furthermore, the experiments at PHELIX showed that it is possible to achieve a rather stable proton acceleration from a sub-critical density plasma, albeit at a low proton energies. It can be concluded that a better pulse contrast is necessary when aiming for highest proton energies. For the plasma dynamics before arrival of the main pulse two elements of the temporal contrast are of particular importance. The pre-pulse triggers the transition into the plasma state and the target will begin to expand. After this, the exponentially rising edge of the pulse, which contains orders of magnitude more energy than the pre-pulse, will drive further dynamics. The final density distribution which the main pulse interacts with is determined by the interplay of both effects.

These observations suggest that future experiments aiming for high proton energy cut-offs require a better pulse contrast than the PHELIX system. This includes in particular a rising edge which begins later and contains less energy and ideally no pre-pulses. However, quantified predictions the necessary contrast improvements can not be made from this data.

In the other extreme, the experiments at JETi showed that a very good pulse contrast cleaned by a plasma mirror is not optimal for proton acceleration from isolated micro-plasmas either. On the contrary, a rather significant expansion of the target to about one tenth of its initial density is necessary to reach the optimum acceleration condition. If this condition is met, the proton energies and number of accelerated particles in the laser direction increase significantly.

From these observations of the target expansion at PHELIX and JETi, it can be concluded that a somewhat imperfect pulse contrast can be tolerated and might help yielding the best acceleration results. This could allow designing experiments without plasma mirror, increasing the efficiency of the laser itself.

Moreover, the strong shot-to-shot fluctuations that were observed at JETi make the experiments cumbersome and inhibit translation of this source towards applications for irradiation experiments with ions. A straightforward approach to reduce the fluctuations due to residual motion of the target is to increase the focus diameter. This can be achieved by focusing the laser more loosely with a larger f-number optic. Additionally, this would reduce spatial aberrations due to alignment errors, as larger f-number optics are less sensitive to the laser angle of incidence. However, this obviously reduces the peak intensity, so a higher power laser system is required.

The Laser-driven ION (LION) beamline of the Advanced Titanium-sapphire LASer 3000 (ATLAS-3000) system at CALA, which is described in detail in Section 2.3, was considered a perfect candidate for follow up studies. The intermediate contrast is much better than at PHELIX (see Figure 1.2). A synthetic variable short pre-pulse was added to enable additional expansion of the target, if the intrinsic contrast was found to be insufficient to reach optimal conditions. Maximum proton energies in the 100 MeV range are expected at this system, if optimum conditions can be reached [77].

1.3. Research Questions

The PHELIX campaign leaves the question of how low the temporal contrast can be. In particular, it is not known whether an expansion over a long time during the rising edge of the pulse results in different plasma conditions than arise from a single short pulse. Besides experimental investigation, the development of a model for the plasma creation and dynamics would allow to close this gap in the parameter space. Such a model could also be of use in identifying other interesting parameter regimes, in particular to support expensive experiments.

This thesis therefore tries to answer the questions

- How do the plasma dynamics change in a high-power system with intermediate temporal contrast compared to JETi and PHELIX?
- Is a slowly rising edge beneficial or detrimental for proton acceleration from sub-focus MLTs?
- Is it possible to estimate the plasma behavior to allow for predictions at arbitrary laser systems and identification of parameter sets of interest?

To this end experiments were performed at the CALA using the ATLAS-3000. A numeric model of the plasma creation and dynamics during the early times of the laser pulse was developed to understand and explain the experimental observations. This model is verified also against previous experiments and new RHD simulations, which shed more light into the small-scale dynamics during the interaction.

In Chapter 2 first the fundamental aspects of laser-driven ion acceleration are described along with the key parameters and how they are determined. Then the setup employed in the experiments is delineated and some of the experimental pit-falls and challenges are elaborated upon. Finally the results are discussed taking into account the different

diagnostics and hypotheses to explain the observations are formulated. A key result of the experiments is the realization that no proton acceleration could be observed with an optimum overlap between target and focus. The maximum proton energies of 12 MeV are in the expected range for the reconstructed target positions, but well below the anticipated 100 MeV for the best conditions. One hypothesis to explain this is an insufficient temporal contrast, destroying any target placed perfectly in the focus. This motivates further investigation of the plasma dynamics driven by the laser before arrival of the main pulse.

As a basis for the numeric model a more comprehensive theoretical description of the interaction of laser pulses with matter is given at the beginning of Chapter 3. This includes a model for the transition of dielectric solids to a plasma, which is adapted for the experimental laser and target parameters. Building on this, a simplified model for the expansion is developed, taking into account short pre-pulses as well as a slowly rising edge and a constant intensity pedestal. This model is directly verified against RHD simulations which were performed in the context of the experiments at ZEUS and model the interaction and subsequent expansion after a short pulse of moderate intensity. For an experimental validation the temporal contrast of the Advanced Titanium-sapphire LASer (ATLAS) and PHELIX systems is used and the resulting plasma condition checked for consistency with the experimental observation.

To provide further benchmarking and test the simplifying assumptions of the model, simulations of these systems were performed using the same RHD code. These simulations, which are described in Chapter 4, yield insight into the more complex dynamics of the plasma, like shock formation. In order to enable comparability, averaged quantities are derived from the simulation data.

Experiments, model, and simulations are brought into context in Chapter 5. While small scale features like shock of the simulation are not included in the simple model, the agreement on large scale phenomena and averaged quantities is good. Furthermore, the model reproduces the results obtained at PHELIX and provides a good explanation of the results at ATLAS. This motivates confidence in the ability of the model to fill the so far blank parts of the parameter space and provide predictions for other laser systems.

Finally, Chapter 6 provides a summary of the thesis and an outlook into further applications.

2. Experiments

2.1. Generation of Ultrashort High-Power Laser Pulses

LASER principle

The driving principle behind any laser is Light Amplification through Stimulated Emission of Radiation, which was first experimentally realized by Maiman in 1960 [78]. A laser requires a gain medium with at least three energy states, the intermediate of which is metastable. Pumping energy into the gain medium, a population inversion is reached, where the metastable state is more populated then the ground state. If a photon with the correct transition energy passes through the medium, it can stimulate the emission of a photon by transition into the ground state. Seed photons can be generated in the gain medium itself by spontaneous emission. When the medium is placed inside an optical cavity with high quality, photons pass through the material many times and stimulate emission with each pass, hence amplifying the light. As stimulated emission is a coherent process, the photons will be spawned in phase with the seed photons, generating coherent radiation.

If continuously pumped, this process generates Continuous Wave (CW) radiation. In order to generate pulses, electro-optical effects (e.g. polarization rotation) can be used to switch the cavity open and closed [79]. This allows generation of ns short pulses, limited by the rise and fall times of high voltage sources. Another possibility is mode-locking, for which there are many active and passive approaches (for more information see Ref. [80, Chapter 2] and references therein). It allows generation of very short pulses (fs) oscillating inside the cavity. These pulses are no longer monochromatic, but have a broad spectrum. Modern ultra-short laser oscillators often use the optical Kerr effect [81, 82] inside the gain medium as passive mode-locking mechanism. The Kerr effect is a change in the refractive index of a material caused by a strong electric field. In this case, the field of the laser pulse itself provides this electric field, resulting in an intensity dependent refractive index. For a Gaussian spatial beam profile, this provides a lensing effect. If the cavity is tuned correctly this leads to a higher amplification at higher intensity and therefore short pulses are better amplified than CW radiation. The pulses are coupled out of the oscillator using an appropriate partially transmissive output coupler.

Chirped Pulse Amplification

High power laser systems typically consist of a short-pulse oscillator followed by multiple amplification stages. For short pulses the damage threshold of the laser medium ($\sim$1 J/cm^2-10 J/cm^2 for Titanium:Sapphire (Ti:Sa) [83]) is quickly reached and the beam diameter has therefore to increase. A way around this limitation was introduced by the invention of the Chirped Pulse Amplification (CPA) technique [84], for which Mourou and Strickland received the Nobel price in 2018. In this technique the initially short pulse is temporally dispersed by changing the optical path length of the different constituent wavelengths. With modern grating stretchers this allows to stretch 10 fs pulses to more than 1 ns. These longer pulses can then be amplified from μJ to $\sim$100 J before being re-compressed to fs duration. This allows to keep the beam diameter small during the amplification stages. Temporal compression is then done in vacuum with a large beam diameter (e.g. 30 cm at ATLAS with 3 PW).

Peak intensities of up to $5 \cdot 10^{22}$ W/cm^2 with laser systems with up to 10 PW peak power with few fs pulse duration have now been demonstrated [85].

2.2. Temporal and Spatial Characteristics of Ultrashort Pulses

2.2.1. Temporal Pulse Shape

While a laser pulse is often idealized as a Gaussian temporal envelope, a real pulse consists of different features distributed over many orders of magnitude in time and power, which are shown in Figure 2.1. Below the main pulse (**a**) with peak power P_{max}, which can usually be reasonably well approximated by a Gaussian, lies a ns long pedestal (**b**) with many orders of magnitude lower power (for modern high contrast systems typically $10^{-10}\,P_{max}$-$10^{-12}\,P_{max}$). This pedestal originates from Amplified Spontaneous Emission (ASE) in the laser amplifiers. In particular, regenerative amplifiers using a cavity design and being operated at high gain are known to generate high ASE levels. The ASE level can be reduced by usage of alternative amplifier technologies, e.g. Optical Parametric Amplification (OPA) [86].

On the scale of a few hundred ps up to a few ps prior to the main pulse often short pre-pulses exist (**c**). These are copies of the original pulse originating from multiple reflections at surfaces normal to the beam propagation. In particular, it is also possible that initial copies which are delayed to the main pulse (post-pulses) are converted by

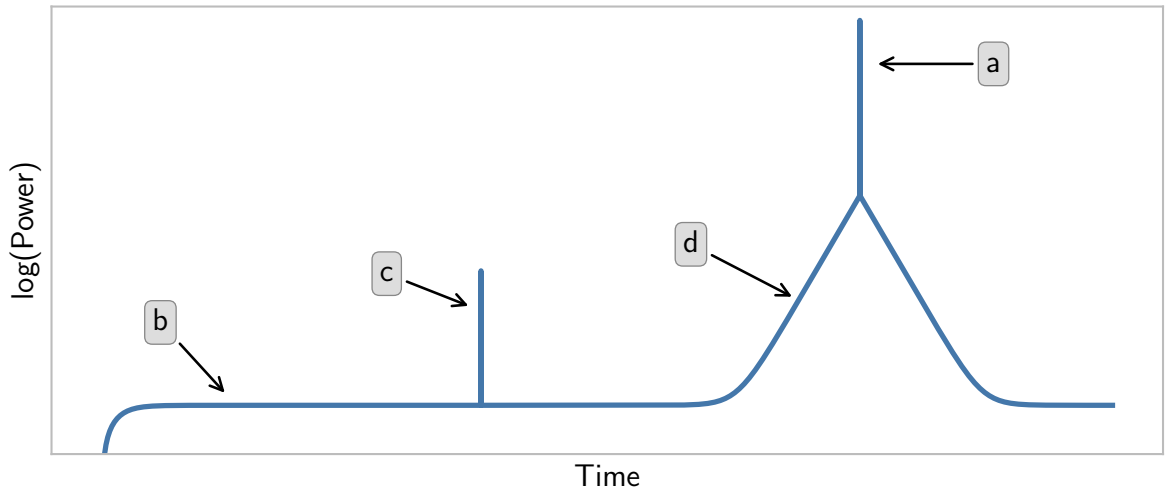

Figure 2.1.: **Schematic Temporal Pulse Shape**
Sketch of main pulse (**a**), ASE (**b**), pre-pulse (**c**) and coherent rising edge (**d**) contributions to a short laser pulse on a logarithmic power and linear time scale.

non-linear effects during the amplification into pre-pulses [87, 88]. However, by careful consideration of all optical components, these pre-pulses can be largely eliminated.

And lastly, rising from the ASE pedestal to the beginning of the main pulse is the so called coherent contrast (**d**). This exponentially rising edge originates from imperfections in the CPA process, most often in the pulse stretcher but also possibly in the compressor. The rise time can vary between a few ps up to a hundred ps. Imperfections on optics in the dispersed beam can create an overlap between spectral components due to scattering. This overlap is then not compensated by the compressor, leading to imperfect compression. Use of high quality optics or changes to the stretcher design can reduce this effect [89].

Furthermore, non-linear effects like frequency doubling [90] or plasma mirrors [91] can be employed to improve the temporal contrast once re-compressed.

The temporal shape of a laser pulse can be measured by different devices on different time and accuracy scales. To determine the shape of the main pulse in the few ten fs up to ps range with a few orders of magnitude dynamic range spectral domain methods are used, as no direct measurement of such processes is possible. Frequency-Resolved Optical Gating (FROG)[92] is often used. It can for example utilize Second Harmonic Generation (SHG) as a second-order non-linear process to determine spectrum and spectral phase of a short pulse. The temporal pulse shape is then reconstructed in an iterative algorithm utilizing the connection of temporal and spectral domain by Fourier transforms. An

other commonly used technique is Self-Referenced Spectral Interferometry (SRSI)[93, 94], which relies on Cross-Polarized Wave (XPW) generation to create a reference pulse with a broader spectrum. Reference and test pulse are then spectrally interfered. Spectral amplitude and phase are extracted by filtering the spectrogram in the time domain. This technique has the advantage that it often allows direct feedback to a spectral shaper in the front-end of the laser to optimize the spectral phase in order to achieve optimal pulse parameters. Other techniques rely on spectral shearing (Spectral Phase Interferometry for Direct Electric-field Reconstruction (SPIDER)[95]), Sum-Frequency Generation (SFG) between a pulse to test and frequency doubled copies [96], OPA with a frequency doubled copy of the initial pulse as pump [97], or a combination of OPA and SFG [98]. Most of these techniques are used in delay-scanning devices, where a pulse copy is variably delayed against the other and a temporal trace is obtained by taking data at multiple points. Some of the these techniques are also adapted into single-shot devices where the delay between two copies is typically created by spatial shearing. Such single-shot devices are of particular importance for laser systems with low repetition rates or low shot-to-shot stability.

For measurement of the temporal contrast over more than ten orders of dynamic range and up to few ns temporal range, scanning Third-Order Auto Correlator (TOAC) devices are employed (e.g. Tundra, Ultra-Fast Innovation; Sequoia, Amplitude Technologies) [99, 100], utilizing Third Harmonic Generation (THG) as a third order non-linear process. Here the input pulse is split after a variable attenuation and one of the pulse copies is variably delayed before being frequency doubled. The fundamental and doubled pulse are then overlapped in a SFG crystal to create the third harmonic, which constitutes the autocorrelation signal. This very low signal is then detected by a Photo-Multiplier Tube (PMT) with variable amplification voltage. By changing the attenuation of the input beam and the voltage of the PMT, the dynamic range of more than ten orders of magnitude can be achieved. The autocorrelation signal $G^3(\tau)$ is described by the third order correlation function [100]

$$G^3(\tau) = \int_{-\infty}^{\infty} I(t-\tau)I^2(t)dt. \tag{2.1}$$

From this it can be seen, that any feature occurring at the leading edge of the pulse will also generate a signal at the trailing edge and vice versa. In particular, short pre-pulses will also generate a short pulse signal after the main pulse and post-pulses a signal before the main pulse. These signals can be differentiated by the third order asymmetric nature of the autocorrelation, which means the signal amplitude at the real position of the pulse

is the square of the amplitude at the mirrored 'ghost' position.

The pulse shape on the fs level is not well resolved, because of the limited resolution of the scanning stages on the order of 10 fs and the intrinsic signal broadening by the autocorrelation process. But information on the ASE level, the position and relative amplitude of short pre- and post-pulses, and the shape of the rising edge of the pulse become accessible.

It is also important to note that the TOAC only measures the temporal power contrast, that is it integrates over the spatial beam profile. As the different parts of the laser contrast can have different spatial modes, and for example different focal spot sizes, the measurement can not be transferred directly to the intensity in the focus, and this translation should always be considered with care.

2.2.2. Laser Focus and Aberrations

In experiments for laser ion acceleration the laser is typically focused by a short focal length Off-Axis Parabolic mirror (OAP) to a diffraction limited spot size of a few µm. As shown in Appendix A, this focusing corresponds to a Fourier transform of the nearfield laser profile in paraxial approximation. For an ideal laser with a flat-top spatial profile in the nearfield, the focus shape is then given by an Airy disk.

However, imperfections of optics as well as alignment errors can introduce deviations from this ideal focus. These deviations are usually expressed by the spatial phase of the nearfield, the so called wavefront. In order to quantify the aberrations from the ideal, flat, wavefront, it is typically decomposed into Zernike polynomials, which span a basis of 2D harmonic functions. The lowest order Zernike polynomials correspond to the alignment error of the focusing optic, i.e. tip/tilt and astigmatism. Higher order polynomials originate mainly from large scale deformations of optics and can not be compensated by simple alignment.

To achieve a diffraction limited focus with smallest size, fast focusing and adaptive optics are often employed. These consist of a deformable mirror, typically a thin membrane with dozens of actuators distributed on the backside, and a wavefront measurement (e.g. Shack-Hartmann sensor [101] or lateral shearing interferometry [102]). An optimization is performed by iteratively measuring the wavefront and moving the actuators in the deformable mirror until the measurement has converged to its target. Generally, this target wavefront is flat for an optimum focus, but it can be adapted to achieve arbitrary aberrations.

A major problem in this scheme is the fact that it is not easy to measure the wavefront

of the beam at full power. Only strongly attenuated copies of the focus are available for the adaptive optic optimization. However, any aberrations introduced by the attenuation are then overcompensated and remain with inverted sign in the real focus. This can in principle be corrected by careful measurement of the individual components, but is in reality complicated to compensate.

The correct and reliable determination of the focus shape in all three dimensions (two spatial and one temporal) is still a significant challenge for high power laser systems and an active field of research.

2.3. Experimental Setup at CALA

The experiments presented in this work were performed at the CALA in Garching near Munich [103]. The mission of CALA dedicated to research the use of laser sources for different bio-medical applications, with a particular focus on cancer diagnostic and treatment. One pillar of this mission is the use of field-resolved broadband infrared spectroscopy (BIRD) for early detection of cancer. This method promises to provide a risk-free, minimally invasive, and cost effective screening technology. Another pillar is the generation of hard X-rays, which can then be used for high resolution and high contrast imaging. The last pillar of CALA is to investigate Laser-driven Plasma Acceleration (LPA) of protons and carbon ions with the goal to provide compact accelerators for tumor irradiation. Beside these three central pillars, research is also conducted in fundamental questions of quantum- and astro-physics.

The high intensity activities circle around two laser systems: the Petawatt Field Sythesiser (PFS-pro) [104] as a research and development system towards high average power and repetition rate plasma acceleration and the ATLAS-3000 with a peak power of 3 PW to drive experiments now. The ATLAS is connected to multiple end stations dedicated to different aspects of the overall research goal. The experiments aiming at acceleration of protons and carbon ions are performed in the LION experimental area.

Other areas are dedicated to electron acceleration and subsequent X-ray generation (ETTF), heavy ion acceleration and high field experiments (HF), and investigation of photon-photon scattering (LUX). SPECTRE will be used to investigate the generation of hard X-rays at kHz repetition rate driven by the PFS-pro system.

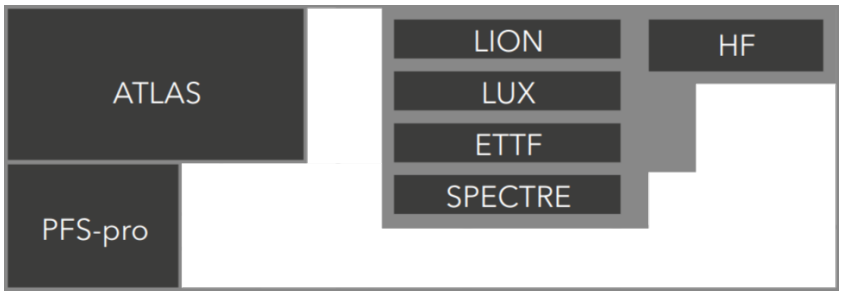

Figure 2.2.: **CALA Layout**
CALA houses two laser systems (ATLAS and PFS-pro), which are connected to five experimental end stations (LION, HF, LUX, ETTF, SPECTRE).

2.3.1. The ATLAS-3000 Laser

The ATLAS laser is a CPA system with titanium doped sapphire (Ti:Sa) as active medium. At full amplification it provides pulses of 90 J before compression at 1 Hz repetition rate. After compression the pulses have a duration of ∼25 fs and the beam diameter is 28 cm. Taking into account the transmission of the compressor and beam delivery, up to 60 J pulse energy can be delivered to the experimental areas.

Pulse compression is measured by FROG (FROG, Swamp Optics) and SRSI (WIZZLER, Fastlite). Measurement of the spectral phase by the WIZZLER is fed back to a spectral shaper in the front-end (DAZZLER, Fastlite) to minimize the pulse duration. Figure 2.3 shows an exemplary measurement of the temporal pulse shape by both devices (**a, b** WIZZLER, **c** FROG). The spectrum has a full width of 80 nm with a nearly constant phase over the relevant wavelengths, resulting in a pulse duration of 28 fs (averaged over 60 shots). The flat-top like spectral shape results in the side lobes visible in **b**.

Temporal contrast is key for ion acceleration and has to be measured over ns range in time and more than eleven orders of magnitude in intensity for a peak intensity of $\sim 10^{21}\,\mathrm{W/cm^2}$. This is achieved by TOAC (TUNDRA, Ultra-Fast Innovations GmbH [99], cp. Section 2.2.1) is used. Figure 2.4 shows three example contrast curves, marking significant points in the development. The green curve recorded on 06.03.2023 represents the intrinsic contrast during the experiments, the red curve from 09.03.2023 shows an example with artificial pre-pulse. To illustrate the progress in the contrast development, the blue curve of 08.05.2024 shows the contrast that was achieved after completion of the experiments reported here. The pre-pulse at −112 ps which can be seen in the red and green curves with a relative amplitude of $>10^{-8}\,\mathrm{P_{max}}$ was removed after the final experiments and is no longer visible in the blue curve. It originated from a post-pulse that was created in the first multi-pass amplifier crystal and then turned into a pre-pulse by

non-linear conversion caused by the large B-integral in the subsequent amplifier crystals [87, 88]. In the measurements performed in 2023 (red and green) the ASE level is at $10^{-10}\,\mathrm{P_{max}}$, in 2024 (blue) at $10^{-9}\,\mathrm{P_{max}}$. This change is likely due to the removal of the spatial filter in front of the measurement device. As mentioned in Section 2.2.1, the TOAC integrates over the incident beam profile. If ASE and main pulse have different spatial modes, this can result in a different transmission through the spatial filter. If the ASE component focuses to a larger spot, its transmission is lower and the level recorded by the TOAC will also be lower.

The rising edge of the pulse begins to rise above the ASE level 100 ps before the main pulse and rises exponentially up to $\sim 10^{-7}\,\mathrm{P_{max}}$. In the last few ps the pulse shape is then dominated by the short main pulse.

In the red curve the artificial pre-pulse can be seen at ~ -300 ps at a level of $10^{-6}\,\mathrm{P_{max}}$. Both timing and amplitude of this pulse can be varied deliberately.

A parametrization of the ATLAS pulse is shown as gray line. In general, a laser pulse with such a shape can be parametrized by a sum of the contributions of ASE, coherent contrast (CC), main pulse (MP), and potential pre-pulses (PP):

$$I(t) = I_{\mathrm{ASE}}(t) + I_{\mathrm{CC}}(t) + I_{\mathrm{MP}}(t) + \sum_i I_{\mathrm{PP},i}(t), \tag{2.2}$$

with

$$I_{\mathrm{ASE}}(t) = I_{\mathrm{ASE},0}, \tag{2.3a}$$
$$I_{\mathrm{CC}}(t) = I_{\mathrm{CC},0} e^{t/\tau_{\mathrm{CC}}}, \tag{2.3b}$$
$$I_{\mathrm{MP}}(t) = I_{\mathrm{MP},0} e^{-t^2/2\tau_{\mathrm{MP}}^2}, \tag{2.3c}$$
$$I_{\mathrm{PP},i}(t) = I_{\mathrm{PP},0,i} e^{-(t-t_{\mathrm{PP}})^2/2\tau_{\mathrm{PP},i}^2} \tag{2.3d}$$

where τ_x are the different characteristic times and $I_{x,0}$ the corresponding relevant intensities. Both are parameters intrinsic to the specific systems and have to fitted accordingly.

2.3.2. The LION experimental area

Figure 2.5 shows the layout of the target chamber, with components relevant for this work highlighted. **a-d** contain diagnostics which are used to determine the laser focus position and shape. The target system is shown in more detail in **a1** and **a2**. **e** is the

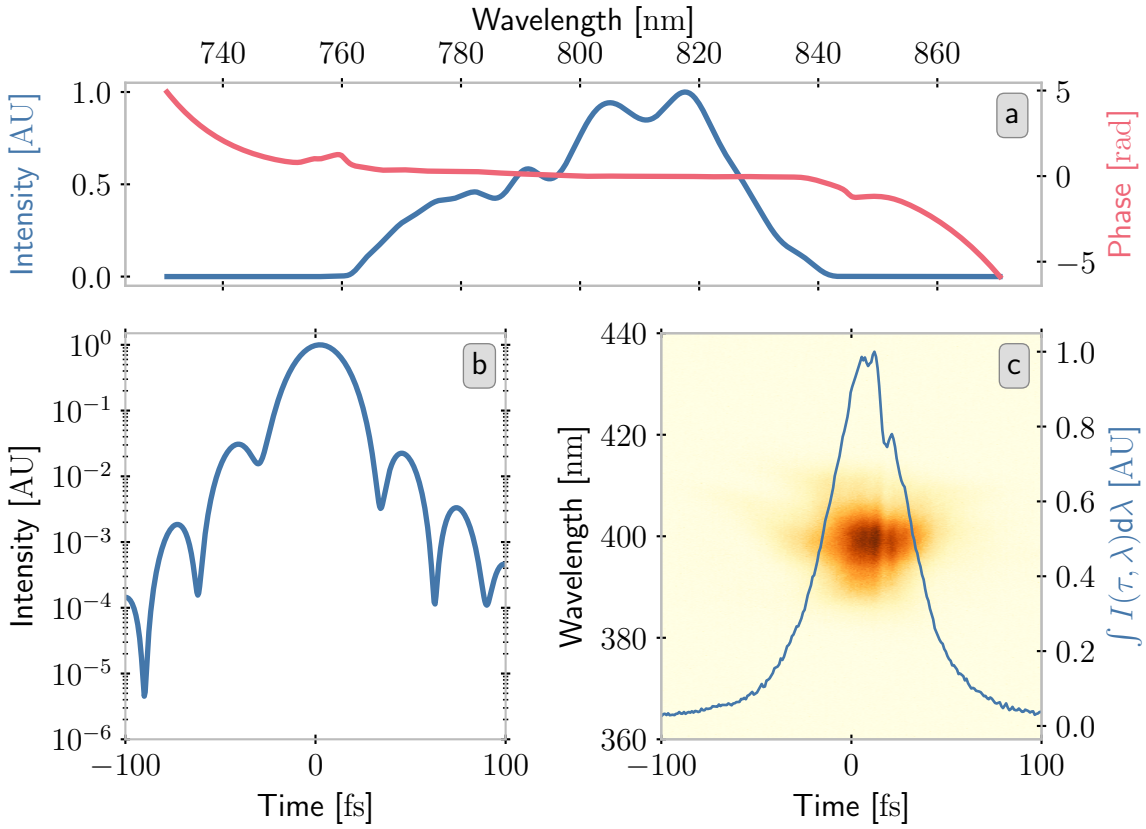

Figure 2.3.: **ATLAS Temporal Pulse Shape**
Spectral-temporal pulse measurement performed with WIZZLER (**a**, **b**) and FROG (**c**) on 09.03.2023. **a** shows the retrieved spectral intensity and phase from the WIZZLER measurement and **b** the corresponding temporal pulse shape calculated by Fourier transform. **c** shows the raw data of the FROG measurement in the spectral-temporal plane (color-scale) and projection on the time axis (blue line).

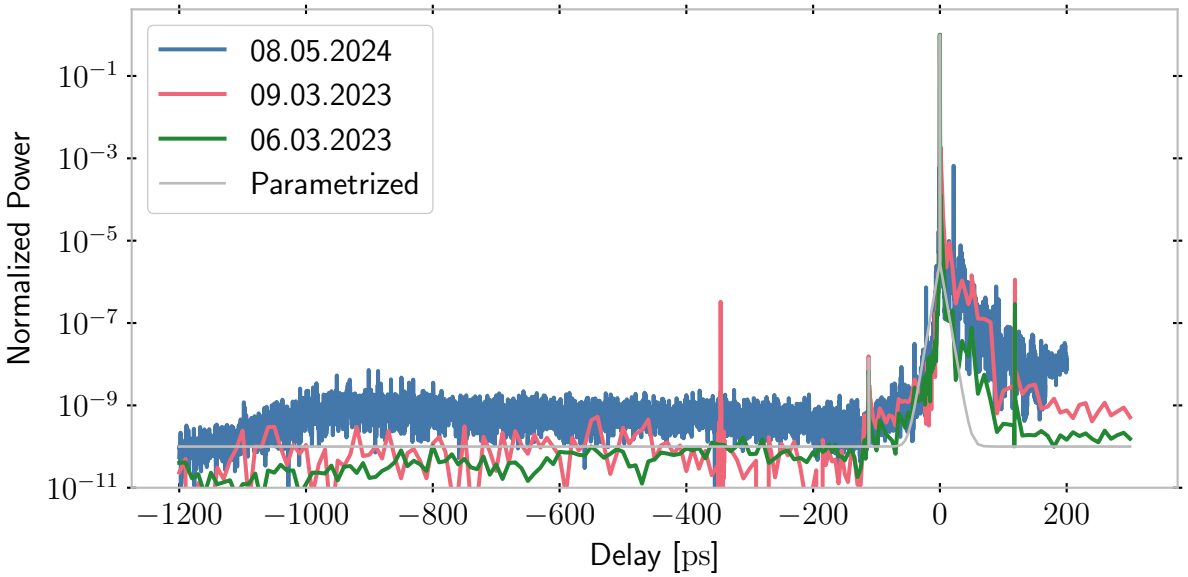

Figure 2.4.: **ATLAS Temporal Contrast**
TUNDRA measurements of the ATLAS-3000 contrast at different stages of development.

diagnostic for the transmitted laser beam profile and **f** the ion spectrometer.

Laser Focus

To monitor laser focus and target a vacuum microscope can be moved into the beam (**a**). It images the focus and target plane on two cameras with magnifications of 10x and 1.5x. Another arm images the nearfield of the laser close to the OAP. Additionally, a Shack-Hartmann wavefront sensor [101] measures the wavefront incident on the OAP. This measurement is fed back to an adaptive mirror in the beam delivery to compensate for distortions and create a diffraction limited focal spot with an attenuated beam.

The direct image of the focal plane is used to position target and focus for best overlap in all three spatial dimensions.

As the position of the laser focus is of particular importance to the experiment, different approaches were investigated to determine and monitor the position of the focus for the full energy pulse. A diagnostic for the incoming beam outside the vacuum chamber (**b**) utilizes the central part of the leakage through a mirror, which is focused with a long focal-length lens and split for different diagnostics. For the position most relevant is a camera just in the focus. When the pointing of the incoming laser changes, both the real laser focus as well as the copy will move by the same number of focus diameters. The correlation between both positions was studied in detail in the Bachelor's thesis

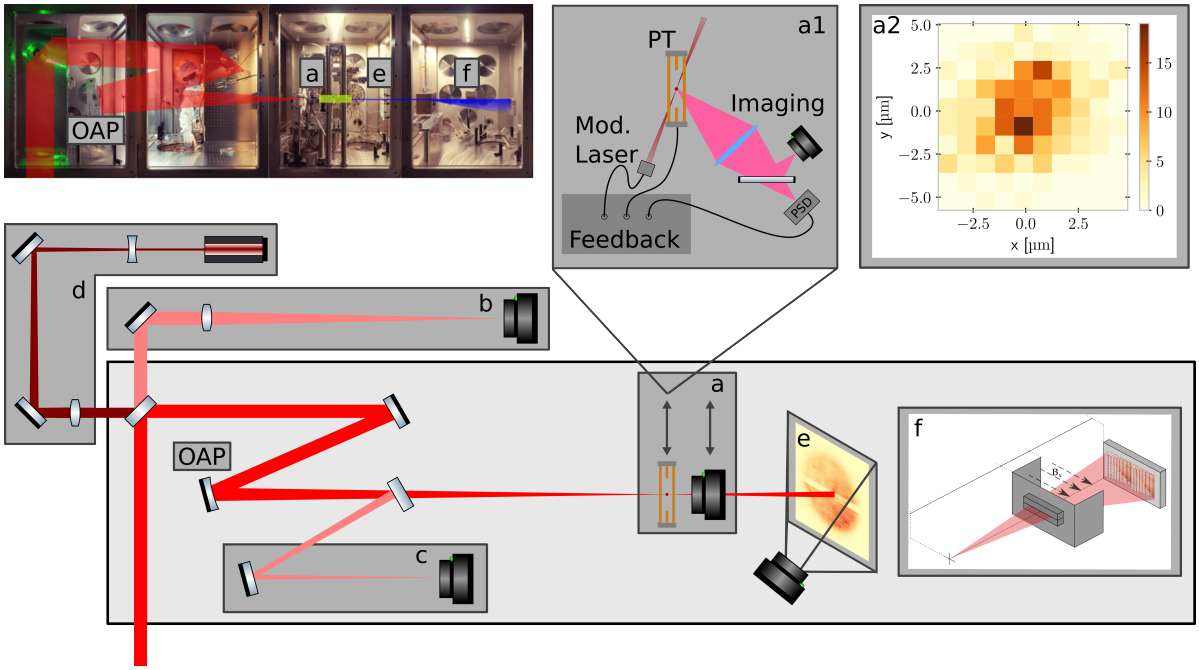

Figure 2.5.: **LION Experimental Area**
Schematic view of the LION end station. The ATLAS pulse (bright red) enters the vacuum chamber (light gray) from the floor, passes two turning mirrors, and is focused by the OAP to the target position (**a**), where the Paul-Trap and a microscope can be moved into the beam. Details of the Paul-Trap setup are shown in (**a1**) and the particle stability in (**a2**). Leakage of the first mirror is used to monitor incoming beam parameters like pulse energy and pointing by focusing the pulse with a long focal length lens (**b**). A copy of the real focus created by the reflection from a thin foil is imaged with a separate microscope (**c**). For calibration of the different diagnostics and to provide a position reference for the target, a Helium-Neon laser is expanded to a third of the original beam diameter (**d**) and coupled into the optical path through the backside of the first mirror. Laser light transmitted around and through the target is caught by a sandblasted glass screen and imaged by a camera (**e**). Through a slit in the screen, ions enter the magnetic dipole spectrometer (**f**). The inset on the upper left shows an image of the vacuum chamber with key components marked. (**f**) is copied from [105] under CC-BY-NC-ND 4.0.

of Christine Frank [106]. While this diagnostic shows a good correlation of large scale long term drifts, the shot-to-shot fluctuations are not well captured, as the top of the chamber vibrates differently then the breadboard inside the chamber. We therefore create an attenuated copy of the laser focus inside the chamber downstream of the OAP (**c**). In a first iteration the initial copy was created destructively by moving an AR-coated substrate inside the beam path. Due to the thickness, size and mounting of the substrate the transmitted laser light was not usable for experiments. In a second iteration a larger pellicle with 20 cm diameter and 2 µm thickness was used to couple out a few percent of the laser light. Due to the very thin material, the transmitted laser was not significantly perturbed and the diagnostic could be used during the real shot onto the target. The copy of the focus is observed by a separate microscope with a 5x magnification imaging onto a camera. To transfer the information of the position from the copy to the real focus position a diode laser was coupled into the chamber through a mirror upstream of the OAP (**d**). With this pilot beam going the same path inside the chamber it could be positioned to overlap with the real laser in the copy and then be observed with the vacuum microscope in the real focus plane.

In the LION area the laser pulses delivered by ATLAS are focused by an OAP with a focal length of 1.5 m, giving a f/5.4 focusing. Assuming a perfect spatial 'flat-top' profile, the resulting diffraction-limited focus has a Full-Width at Half-Maximum (FWHM) of 5 µm. Similar to the temporal contrast, the spatial focus shape is in reality never diffraction limited, but using the adaptive optic loop, a nearly diffraction-limited focus can be achieved. Figure 2.6 shows the focal spot and nearfield of the attenuated beam as captured by the microscope. The ratio between the real peak intensity and the diffraction limited value is known as Strehl ratio. For its accurate determination, it is important to measure the focus with several orders of dynamic range [107]. When doing this for LION we obtain a value of 0.56 [108], i.e. the real focus has only half of the peak intensity that could be reached theoretically.

It is important to note that a several orders of magnitude attenuated copy of the pulse has to be used for these measurements. This copy is created by an attenuator in the ATLAS laser just before compression. It reduces the pulse energy by about eight orders of magnitude by reflecting it from uncoated substrates and can be attenuated further with optional additional filters.

This means the attenuated laser pulse is passing a different beam path than the real pulse and it is reflected by additional optics. Imperfections in these optics result in wavefront aberrations which the real pulse does not have. Also the attenuated pulse

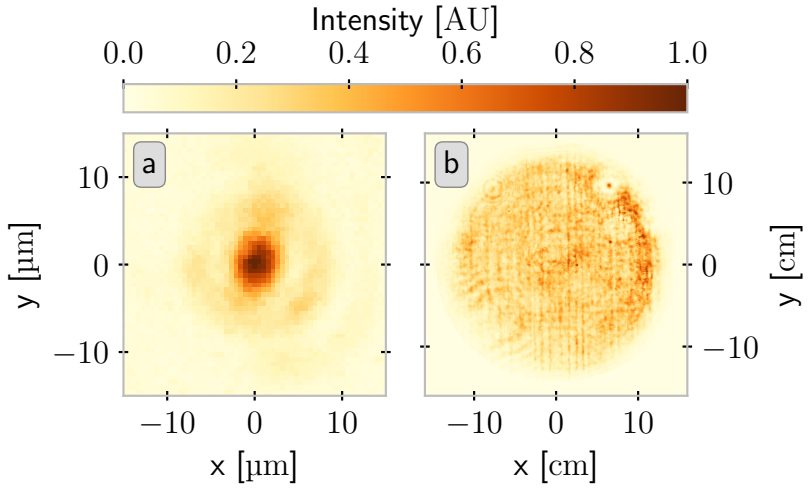

Figure 2.6.: **Spatial Beam Parameters**
Normalized intensity distribution of the focal spot after wavefront optimization with the adaptive optic (left) and the nearfield (right). The images are recorded with an attenuated beam. The small ring patterns visible in the nearfield are caused by dust particles in the microscope and are not part of the real beam profile.

will never be coupled back into the chain on exactly the same axis as the real pulse. This is subject to the fine adjustment capabilities of the individual experimentalist and the stability of the opto-mechanical setup. These two effects result in an attenuated focus that differs from the real one not only in energy but also in the wavefront. To investigate this effect, a diode laser, which is coupled into the amplification chain of the ATLAS and fills the full beam aperture, can be used. The results of this test are shown in Figure 2.7**a** and **b**. Major aberrations introduced by the attenuator are a defocus and a 0° astigmatism, in addition to a small pointing difference. These errors can reduce the peak intensity by more than a factor of three, if they are not compensated. The standard compensation procedure is to record the aberration effect using the diode and then use this to define a corrected target wavefront for the adaptive optic loop.

Another problem is the correct determination of the real focus position and its drifts over many hours. As described above, the attenuated focus is not necessarily at the same position as the real focus. Using the pilot diode, the offset can be minimized, quantified and compensated. However, the focus position is subject to different temporal variations. Firstly, the focus position varies randomly from shot to shot due to vibrations that couple through the building into various parts of the optical system. This variation is typically on the order of a few focus diameters and a typical position distribution is shown in

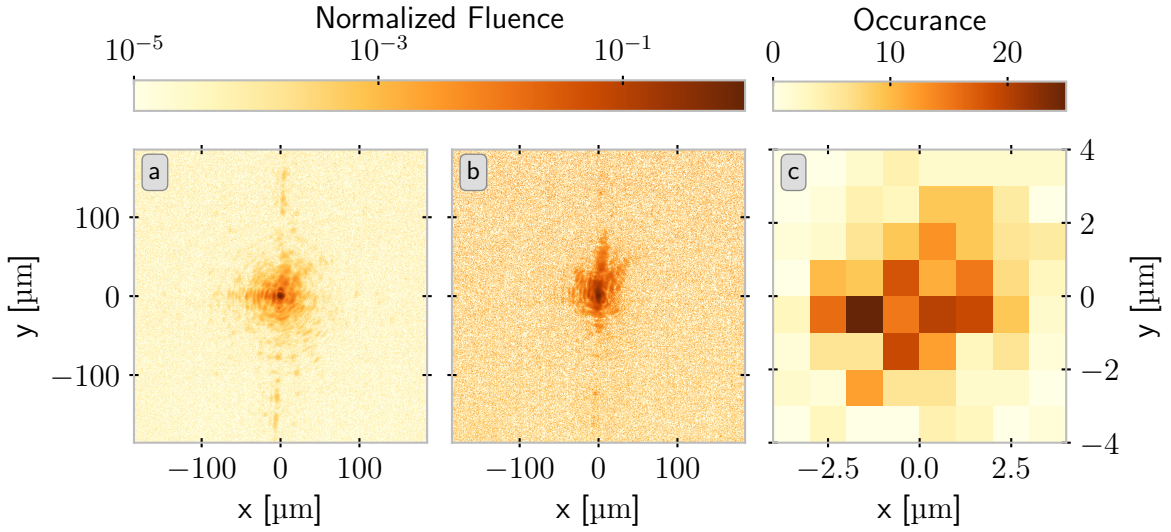

Figure 2.7.: **Focus Jitter and Attenuator Aberrations**
(**a**) Histogram of the center of mass of the focal spot recorded over 386 shots. (**b**), (**c**) High-dynamic range focus fluence distribution for an optimum focus and taking into account attenuator aberrations respectively. The high-dynamic range focus images were provided by Paul Schäfer [108].

Figure 2.7**c**. On longer timescales of tens of minutes to a few hours, thermalization processes in the laser lead to directed drifts of the laser focus with up to tens of focus diameters per hour. An example of the focus drift over four hours in shown in Figure 2.8**a**. These drifts stabilize somewhat after several hours, when all components have thermalized. Using the different diagnostic approaches described above, it was attempted to monitor and compensate these movements as good as possible. One challenge was that it took minutes to position and characterize the target before the shot. During this time, the laser position can not be monitored and therefore minute drifts could not be corrected for.

In addition to the drift in position, also the shape of the focus changes. The dominant variation is here the defocus term. For a fixed plane of observation where the focus is initially optimized, the variation of the peak intensity expressed by the Strehl ratio is shown in Figure 2.8**b**. In the worst case the peak intensity is reduced by nearly a factor of three, because the actual focus plane shifted by $\sim$1.5 Rayleigh lengths.

The timescales and behavior of the different drifts indicate that they originate from thermalization processes in the laser amplifiers and the lab in general, which was meanwhile confirmed.

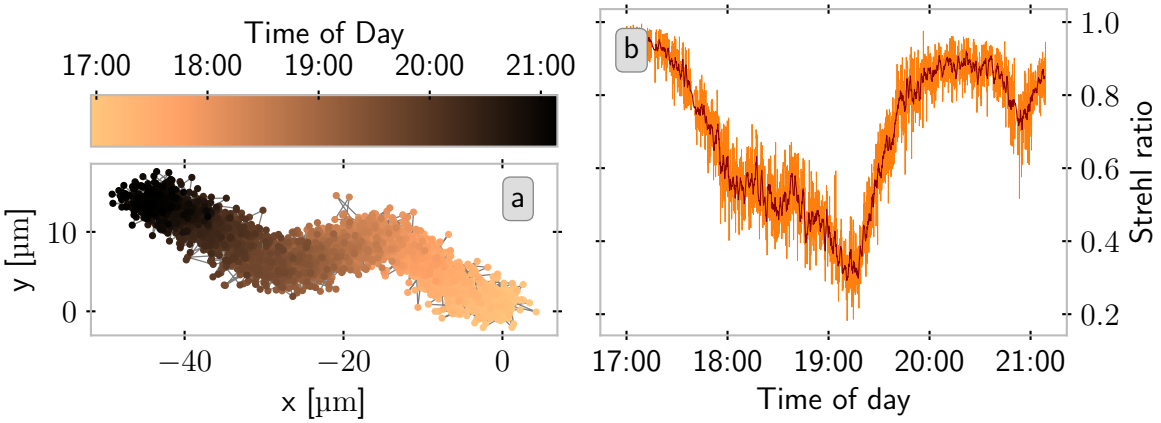

Figure 2.8.: **Focus Drift**
Drift of the focus position (**a**) and Strehl ratio (**b**) over time for an exemplary day. Each dot in (**a**) is a single laser shot. The darker line in (**b**) is a 60 s moving average. Data was provided by Noel Ruhland.

Paul Trap Target System

The target system for the microscopic mass limited targets is described in detail in Ref. [69]. A sphere falling trough the trap is charged by an ion source to have it interact with the trap. An oscillating voltage applied to four rod electrodes generates an alternating quadrupole field, which keeps the sphere contained in two dimensions. Containment in the third dimension is achieved by a constant potential applied to two more electrodes. As the target is charged while already inside the potential it does not have sufficient energy to escape. Its residual motion is first reduced by collisions with a buffer gas at up to 10^{-3} mbar pressure. After this first damping, its residual amplitude can be reduced to a few µm by an active feedback loop modifying the applied voltages to counteract the motion. To account for the geometry in the LION vacuum chamber small modifications mainly to the imaging system of the active feedback were done. Instead of two lenses generating a 1:1 image of the target on air, a single lens was used to create a 1:10 magnified image outside the chamber. This image was then additionally magnified by a microscope onto the Position-Sensitive Diode (PSD) that feeds back into the active damping. A schematic of the setup is shown in Figure 2.5 **a1**. The target is illuminated by a diode laser modulated by 100 kHz. This modulation is used to synchronize the signal from the PSD with the active damping. To position the target in the laser focus and to monitor the residual motion the vacuum microscope is used. Figure 2.5 **a2** shows the residual target movement. The particle position is determined from images taken every second over several minutes and a two-dimensional histogram formed. In order to

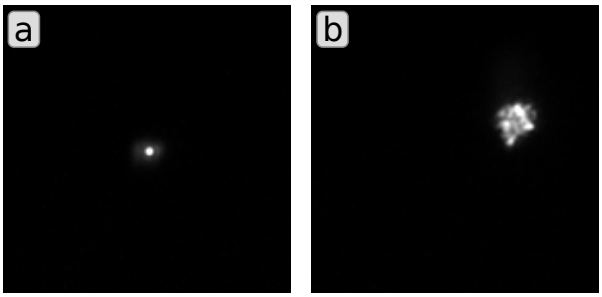

Figure 2.9.: **Target Classification**
Example of microscope images of a single target (**a**) and a cluster (**b**) inside the Paul Trap.

verify the stability and position of the target up to the shot, the imaging onto the PSD is split onto a camera.

Polystyrene (PS) spheres with $(1.01 \pm 0.02)\,\mu m$ diameter served as targets. Due to the strong electrostatic adhesion that can build up between such small dielectrics, sometimes clusters were captured in the trap instead of single particles. To differentiate between clusters and single spheres, the brightness of the images obtained by the high magnification microscope or other cameras observing the target volume is used. An example of a single target and a cluster imaged by the microscope is shown in Figure 2.9. While the resolution of the microscope is not sufficient to resolve a single 1 µm particle, clusters were visible as larger and brighter with multiple maxima. In contrast, single particles show a single maximum and the light distribution follows the Point-Spread-Function (PSF) of the microscope.

Transmission Images

In particular when trying to shoot onto mass-limited targets, the diagnostic of the transmitted laser light is important. The total amount of energy transmitted provides information about the size of the target during the interaction, while the spatial intensity distribution is connected to the spatial position of the target with respect to the laser focus. A screen of sandblasted glass placed 90 cm downstream of the target monitors the transmitted laser profile (**e**). The screen consists of two glass panes with a $\sim$1.5 cm slit in between to let the ions pass into the spectrometer. The screen is imaged by a camera inside the vacuum chamber.

As a key scalar quantity that is easily accessible from this diagnostic is the integral over the transmitted laser profile. The ratio between the integral of a shot with target and an empty shot, that is one without target, yields the transmission or extinction ratio.

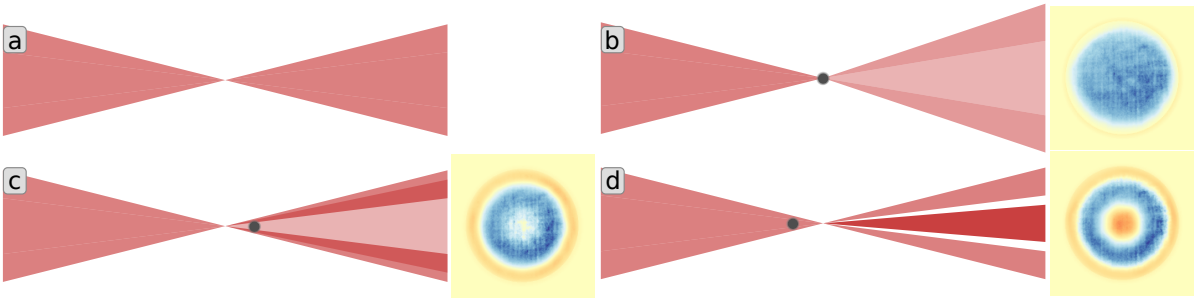

Figure 2.10.: **Transmission Effects**
Schematic representation of different transmission scenarios: no target (**a**), target in focus (**b**), target downstream of focus (**c**), and target upstream of focus (**d**).

This quantity gives an estimate how much laser energy interacted with the target, being either absorbed or scattered outside the acceptance angle of the scatter screen.

More difficult to access is the information on the relative position of target and laser focus. We aim to predict the pattern by simulating the effect of the plasma on the transmitted laser profile.

In a simplified consideration of a collisionless plasma, the plasma can have two effects on a laser pulse. If the electron density n_e is above the critical density n_c, the laser pulse will be absorbed or reflected and the transmission is essentially zero (assuming the plasma is significantly thicker than the skin depth). On the other hand, if the density is below the critical density, the plasma acts as a pure phase object. For spherical geometries this results in an effective lensing effect. This behavior of the plasma can be described by the complex refractive index η for a collision-less plasma

$$\eta = \sqrt{1 - \frac{n_e}{n_c}}. \tag{2.4}$$

As the refractive index is always smaller than one, any convex plasma structure (e.g. spherical symmetric) will have the effect of a negative lens, refracting light beams away from the optical axis.

A realistic target density distribution will always contain at least an outer part below the critical density. We characterize the thickness of the underdense layer by an exponential decay with a scale length l. This means that there exists always some contribution from the lensing effect, even for a plasma with a high central density.

These assumptions yield insights about the target conditions when looking at a typical transmission image (cp. Figure 2.10).

First, asymmetries in the transmission pattern result from asymmetries in the laser-target interaction. This could be an asymmetric target shape, an offset of the target from the optical axis, or an asymmetrical laser focus.

Second, different positions along the laser axis result in different diffraction patterns. To illustrate this, the incoming laser can be divided in an inner cone which interacts with the target and an outer cone-shell which passes the target to the side undisturbed (see Figure 2.10). The final transmission image is the coherent superposition between both cones. If no target is placed in the beam, the profile remains unaffected (**a**). A target placed perfectly in the laser focus (**b**), diffracts light away from the center of the beam and a lot of light is refracted out of the original beam profile, resulting in a low transmission into the original beam diameter. If the target is placed downstream of the focus position (**c**), the divergence angle of the inner light cone in increased and light is diffracted from the center of the beam towards the edge. On the other hand, when placing the target upstream of the focus (**d**), the focus of the inner cone is shifted downstream and the opening angle of the cone is reduced. This results in an increase of light towards the center of the image.

In order to retrieve quantitative information and strengthen the qualitative reasoning, numerical simulations of the transmission image formation were performed.

In general, this could be done by directly solving the Fresnel-Kirchhoff diffraction integrals for propagation of the beam into a certain plane, then applying the effect of the target (amplitude and phase modulation) and solving the integrals again for the propagation to the screen. However, as the Fresnel-Kirchhoff integrals are computationally expensive, it is beneficial to employ the commonly used Fresnel and Fraunhofer approximations, depending on the desired propagation distance, in a numerically favorable implementation. The details of the implementation can be found in Appendix A.

As a simplification, the target is modeled as a three dimensional Gaussian density distribution with spherical symmetry. By specifying the peak electron density n_p, the width of the distribution d is given by conservation of the particle number N_e, assuming a fully ionized sphere of equal parts hydrogen and carbon atoms at initial mass density of $\rho_0 = 1\,\mathrm{g/cm^3}$ ($n_e = 3.3 \cdot 10^{23}\,\mathrm{cm^{-3}}$) and diameter $d_0 = 1\,\mu\mathrm{m}$. This distribution is then converted into a refractive index distribution (Equation (2.4)) before being projected along the propagation axis to yield a two dimensional phase term. The distance between target and focus plane is z and the target center has a transversal shift x from the beam axis.

The simplification of projecting the refractive index distribution onto a single plane

greatly reduces the computational effort of the simulation. As the typical extent of the target is $d \sim \sqrt[3]{n_0/n_p} \cdot 1\,\mu\text{m}$ and much smaller than the Rayleigh range of the laser of $\approx 25\,\mu\text{m}$ for a f/5 focusing, this procedure is considered a good approximation.

The beam profiles shown in Figure 2.10 are simulation results for Gaussian plasma density distributions with $n_p = 10\,\text{n}_\text{c}$ central density placed $z \in \{0, +100, -100\}\,\mu\text{m}$ from the focus on the laser axis ($x = 0$).

Nevertheless, a direct reconstruction of the experimental transmission images was not successful. Therefore we performed first a set of simulations with central density $n_p \in \{0.01, 0.1, 1, 10, 100\}\,\text{n}_\text{c}$, up-/downstream positions $z \in \{-100, -75, -50, -25, 0, 25, 50, 75, 100\}\,\mu\text{m}$, and lateral offset $x \in \{0, 2, 4\}\,\mu\text{m}$. These images are shown in Appendix A.5. This data base allows to select suitable initial conditions from which we iteratively optimized the parameters until a satisfactory agreement with the experimental observation was achieved. Due to different complications in the experimental data (perspective distortion, noise, missing data from the spectrometer entrance) the fit is done qualitatively until a good visual similarity is reached and the observed and calculated transmission ratio agreed.

Estimating the uncertainty of this error is not easy, but the transmission ratio can help defining an error margin. We chose a relative transmission of $\pm 5\,\%$. The error of each parameter n_p, z, x, which defines the target state on interaction, is then bound.

Ion Spectrometer

For characterization of the ion spectra a magnetic dipole spectrometer Wide Angle SPectrometer (WASP) [105] with a Complementary Metal-Oxide-Semiconductor (CMOS) chip detector (Radicon Imaging) is used 1.6 m downstream of the target (**f**) [109, 110]. Ions are deflected in the 10 cm long magnetic field by the Lorentz force, where faster ions experience less deflection than slower ions. The ions are therefore dispersed in one dimension by the dipole field. To increase the spatial spread the ions drift distance of 68 cm between the magnet and the detector. To calibrate the energy map on the detector aluminum strips of varying thickness (PABLONE) are placed in front of the detector. Depending on the energy of an incident proton, it can penetrate a certain thickness of aluminum and be detected or not. The resulting cut-off lines correspond to the energies required for penetrating Aluminum with this respective thickness. A slit with a 200 µm wide opening is placed in front of the dipole. As the measured spectrum is the convolution of the magnetic deflection with the slit opening, the thickness of the slit can be used to optimize the trade-off between signal strength and energy resolution. A smaller slit results in a higher resolution but lower signal level, as less ions pass through

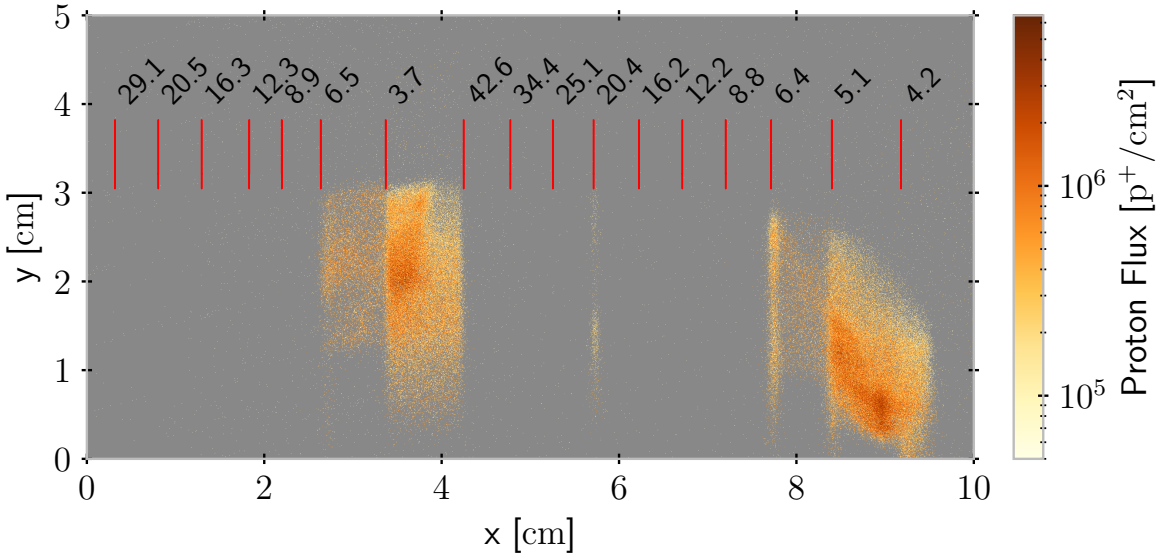

Figure 2.11.: **Spectrometer Signal**
Example image recorded by the ion spectrometer. The cut-offs by the aluminum phantom are clearly visible and the energies necessary to penetrate a certain thickness are marked on the top in MeV.

it and can be detected. The other way around, a wider slit lets a larger number of ions pass onto the detector, resulting at a higher signal level at the cost of lower resolution. An example of the signal recorded by the detector is shown in Figure 2.11. The cut-off lines are marked by the energy necessary for a proton to penetrate the corresponding thickness of Aluminum.

If the proton numbers are low and only coarse information is sufficient the slit can be removed. Then the entrance is 1 cm wide. The magnetic field will still deflect the ions, but the energy resolution is basically limited to the observation of the cut-off lines. The latter configuration was used in nearly all experiments presented here, as otherwise the number of detected protons was too low.

The number of protons is estimated by integrating over the area behind the 3.7 MeV cut-off. To convert the raw signal of the detector to a proton number, an empirically determined conversion factor of 33 ADU/MeV is used.

The proton acceleration of a single shot is characterized by the two metrics of maximum energy determined by the cut-off lines and estimated proton number.

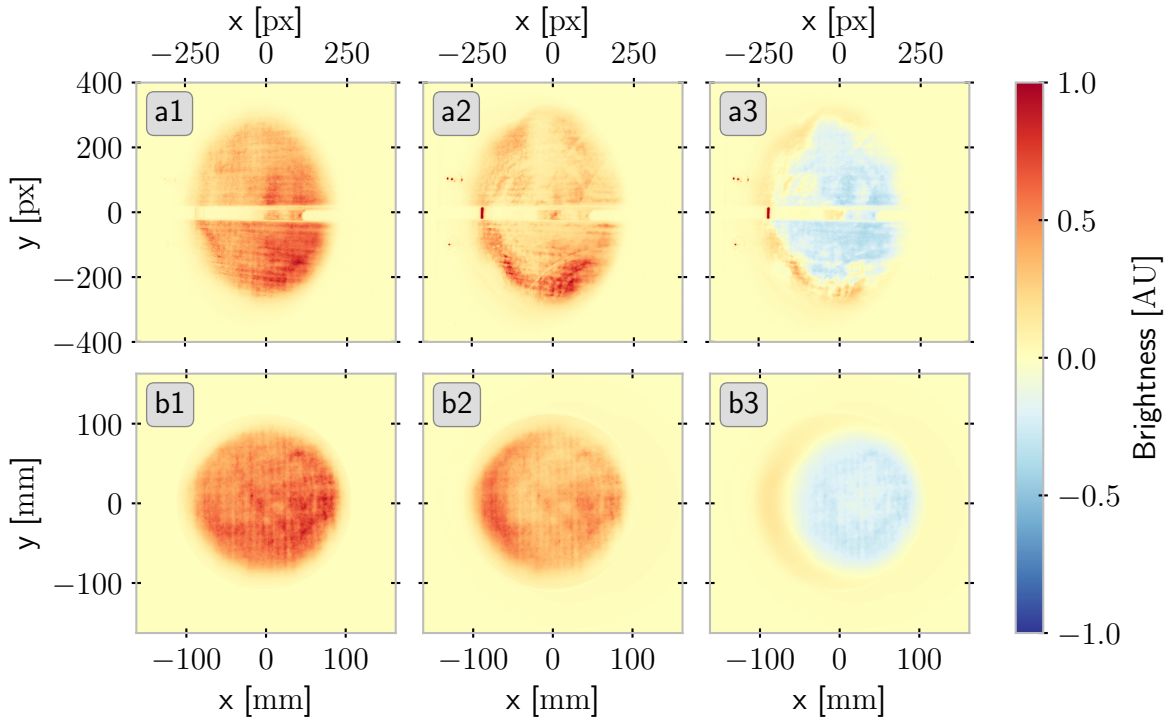

Figure 2.12.: **Transmission Images**
Example for experimental (**a1-a3**) and simulated (**b1-b3**) transmission images. The left column (**a1, b2**) shows the respective transmission without target, the central column (**a2, b2**) with target, and the right column (**a3, b3**) the difference between both.

2.4. Results and Discussion

In the time between November 2021 and April 2023 two experimental campaigns of approximately six months each were performed. During this time 494 shots on targets were carried out with varying settings of laser energy, focus optimization and temporal contrast. In order to enable a quantitative comparison of the acquired data, a few key observables were defined.

Transmission Analysis

An example for the recorded transmission image is shown in Figure 2.12 **a1-a3**. It is clearly visible that the intensity in the central part of the beam is reduced, while a single relatively broad ring is visible on the edge of the beam profile. This indicates that the target was placed downstream of the focus. The fact that the ring is not closed further implies that the target was positioned off the optical axis.

In Figure 2.12 **b1-b3** the simulation creating the best agreement with this experimental image is shown. For this simulation the Gaussian target density distribution had a central density of $n_p = (30 \pm 20)\,\mathrm{n_c}$ and was placed $z = \left(65^{+20}_{-10}\right)$ µm downstream of the focus and $x = (2.5 \pm 0.5)$ µm from the optical axis. The total simulated transmission of 76.3 % is in very good agreement with the experimental value of 76.7 %. There is also a remarkably good qualitative agreement in the spatial distribution. The simulation reproduces the open ring pattern very well with similar contrast as the experiment.

Shot Selection Criteria and Classification

As there is a large fluctuation in the shot quality and parameters over the 494 shots, some selection criteria have to be applied for interpretation. The first criterion is selecting only shots which have produced a significant signal on the proton spectrometer. This selection is realized by filtering out only images which contain a significant number of protons with signal beyond the 3.7 MeV cut-off region and reduces the number of shots to 104.

In order to correlate the ion production with the shot quality, it is necessary to evaluate the transmission image. Therefore, the second criterion is an interpretable transmission image, a corresponding dark reference, no significant saturation of the image and a clear pattern that can be reproduced by the simulations. As the manual fitting routine for the parameters is too involved to be performed for each single image, the image is manually compared to parameter-scan simulations and classified to the next best fitting case. This criterion further reduces the number of analyzable shots to 56. The shots are classified in their position (z, x) relative to the laser focus.

The selection still contains results from single targets as well as clusters of undetermined size. While it is possible to determine the relative position of these targets with acceptable accuracy, no information about the expansion is available, as the initial size is unknown. Selecting only shots which can be identified from the target diagnostics to be performed on single spheres reduces the number of shots to 22.

Shot Quality and Position

In order to understand the observations of low hit rate (21 %) and relatively low proton energies ($E_{max} \leq 8.9\,\mathrm{MeV}$) it is instructive to compare the reconstructed shot positions with the spatial intensity distribution of the laser. On the top of Figure 2.13, the target position, reconstructed from the transmission image, of each shot in the r-z-plane is overlaid with the laser intensity distribution for a maximum of $5 \cdot 10^{20}\,\mathrm{W/cm^2}$

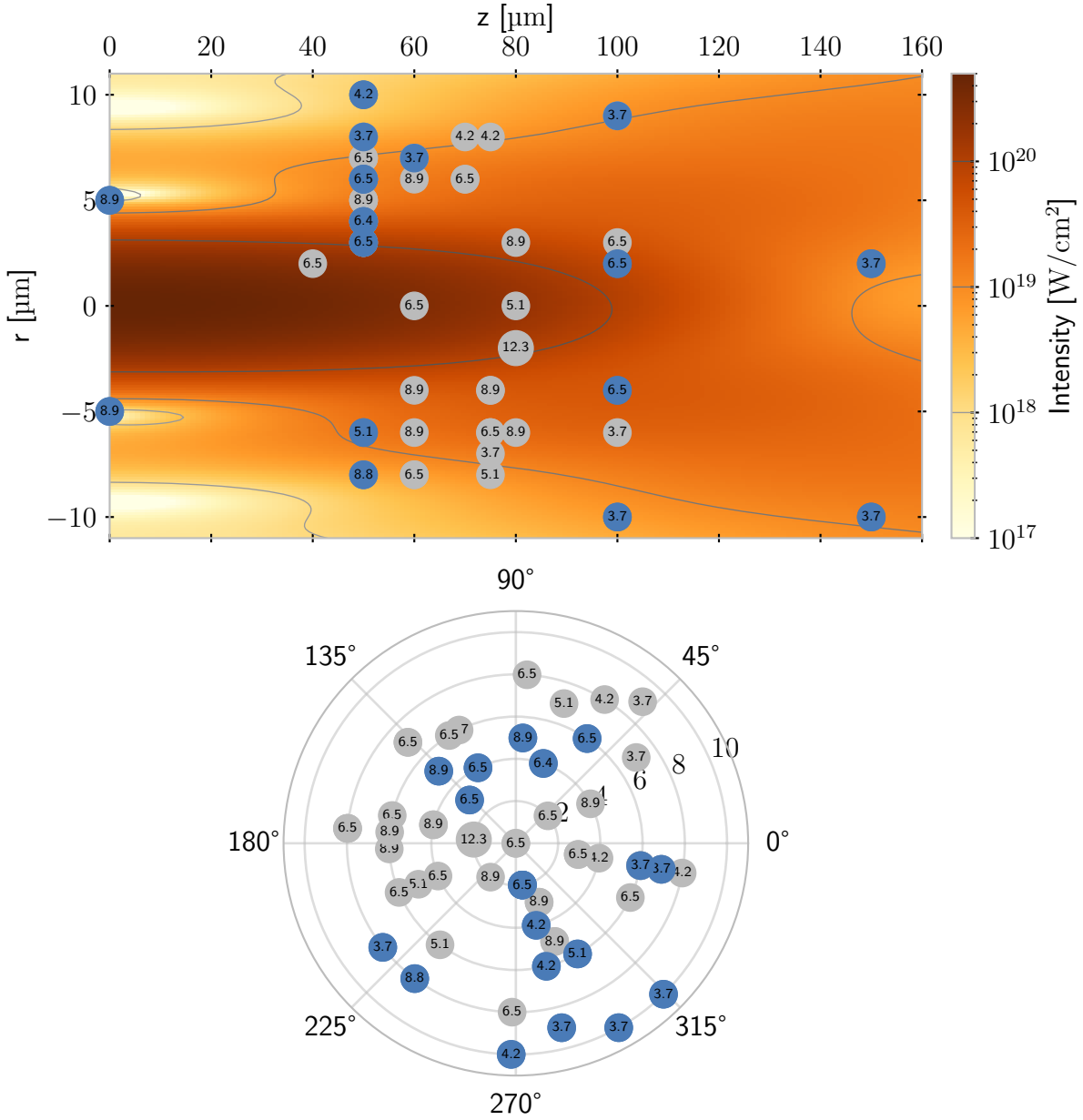

Figure 2.13.: **Shot Positions**
The circles mark the position of each shot with at least 7 J on target that produced protons with more than 3 MeV and an interpretable transmission image in the r-z-plane (top) and r-θ-plane normal to the laser axis (bottom). The color-scale indicates the laser intensity distribution assuming a peak intensity of $5 \cdot 10^{20}\,\mathrm{W/cm^2}$ with the gray lines indicating iso-intensity lines. Blue markers indicate shots from single targets, gray markers from clusters or undetermined parameters. The values inside the markers give the maximum proton energy in MeV.

(corresponding to the best achievable focus with 7 J on target). All shots which produced ions were located in the volume where the intensity is below $\sim 10^{20}\,\mathrm{W/cm^2}$ downstream of the focus. They cluster in the volume 50 µm-100 µm behind the optimum focus and tend to be $\sim 5\,\mu\mathrm{m}$ from the beam axis. In the radial dimension (bottom of Figure 2.13), the distribution is uniform around the laser axis. Numbers represent the maximum proton energies in MeV. The energies are in the expected range of 5 MeV-10 MeV for the intensities between $10^{19}\,\mathrm{W/cm^2}$-$10^{20}\,\mathrm{W/cm^2}$ that actually interact with the target at its respective position. At lower intensities the acceleration is insufficient for the protons to pass the detection limit of 3.7 MeV.

For the clustering of the targets downstream of the focus, a few explanations are possible.

First, the distribution of the target positions suggests that radiation pressure effects as in an optical tweezer [111, 112] could be responsible for a premature displacement. This hypothesis can be tested by a quick estimation of the radiation pressure effect. The force exerted by the radiation is

$$F_{\mathrm{rad}} = \frac{2qP}{c}\frac{A_{\mathrm{targ}}}{A_{\mathrm{las}}}, \tag{2.5}$$

with efficiency $q \approx 0.1$, target and laser cross section area A_{targ} and A_{las}, and speed of light c. The ratio of the cross sections is $\frac{A_{\mathrm{targ}}}{A_{\mathrm{las}}} \approx \frac{1}{25}$.

Assuming the ASE irradiates the target with a constant power of $P \approx 10^{-10} P_{\mathrm{peak}} \approx 10^5\,\mathrm{W}$ for 1 ns duration, the force is $F_{\mathrm{rad}} \approx 10^{-5}\,\mathrm{N}$ and the acceleration $a = \frac{F_{\mathrm{rad}}}{m_{\mathrm{targ}}} \approx 2 \cdot 10^{10}\,\mathrm{m/s^2}$. Here the target mass is $m_{\mathrm{targ}} \approx 5 \cdot 10^{-16}\,\mathrm{kg}$. The resulting displacement after $t = 1\,\mathrm{ns}$ acceleration, assuming the target is initially at rest, is $\Delta z = \frac{1}{2}at^2 \approx 10^{-8}\,\mathrm{m}$. This is six orders of magnitude less than observed and five orders of magnitude less than the target size. It can therefore be assumed, that radiation pressure effects, by light arriving before the main pulse can not displace the target significantly.

Also, photophoretic forces, which are often orders of magnitude larger than radiation pressure, can not occur, as they require a substantial background pressure [113]. Pressure from ablation is also typically magnitude larger than the radiation pressure at non-relativistic intensities ($I < 10^{18}\,\mathrm{W/cm^2}$) [114, Chapter 1.4][115, Chapter 9.1.6].

It is created by the outflow of hot plasma generating pressing against the critical surface in a rocket effect. To estimate the effect of the ablation pressure, we assume a temperature of the outflow of $k_{\mathrm{B}}T_e \approx 1\,\mathrm{keV}$ and a duration of $\Delta T \approx 40\,\mathrm{ps}$, as this process only begins once the plasma is created. The pressure P_{abl} can be calculated as [115, Eq. 9.43]

$$P_{\mathrm{abl}} = \mathrm{n_c}\left(1 + \frac{1}{Z}\right) k_{\mathrm{B}} T_e \approx 2 \cdot 10^{11}\,\frac{\mathrm{N}}{\mathrm{m}^2}. \tag{2.6}$$

Here $\mathrm{n_c} \approx 10^{21}\,\mathrm{cm}^{-3}$ is the critical density and $Z \approx 3$ the charge state. Multiplying the pressure with the target cross-section $A_{\mathrm{targ}} \approx 8 \cdot 10^{-13}\,\mathrm{m}^2$ yields the ablation force of $F_{\mathrm{abl}} = P_{\mathrm{abl}} A_{\mathrm{abl}} \approx 1.6 \cdot 10^{-1}\,\mathrm{N}$. For the target mass of $m_{\mathrm{targ}} \approx 5 \cdot 10^{-16}\,\mathrm{kg}$, this results in an acceleration of $a_{\mathrm{abl}} \approx 3 \cdot 10^{14}\,\mathrm{m/s}^2$ and a displacement of $\Delta z = \frac{1}{2} a_{\mathrm{abl}} (\Delta t)^2 \approx 3 \cdot 10^{-7}\,\mathrm{m}$.

While this displacement is of the same scale as the target diameter, it is still two orders of magnitude less than the experimental observation.

2.5. Experiment Conclusions

Analysis of the transmission images allowed us to reconstruct the target positions relative to the laser focus. This revealed that in any shots which resulted in significant proton acceleration, the target was systematically displaced from the focus position (see Figure 2.13). As we can exclude the laser pushing the target out of the focus prior to the main pulse, two hypotheses to explain this observation remain.

One possible explanation are systematic offsets. As mentioned in the discussion of the laser focus in Section 2.3.2, there are significant uncertainties regarding the position of the high-power focus. While it was attempted to compensate these effects, there might be remaining issues with defocus drifts or aberrations introduced in the attenuator and its filters. As the area in which acceleration becomes possible also increases significantly this far from the focus, it further becomes much more likely to hit a target when the laser shows drifts and jitter in the position. This could lead to a bias, as shots which were positions in the correct plane were less likely to hit the target. This hypothesis is hard to test directly and can only be proven by exclusion principle.

Another explanation could be an insufficient contrast of the laser system. If, for example, the ASE radiation is too intense at the highest focus intensity, it could destroy any target positioned there before the main pulse arrives. This would explain the absence of hits in the volume with intensities above $10^{20}\,\mathrm{W/cm}^2$. With our current understanding, we consider this explanation most likely.

Therefore, the following chapters are dedicated to develop a simple understanding and a numerical model that describes the interaction of the laser pulse with a microscopic target, starting from initial ionization.

3. Expansion Model

3.1. Interaction of High-Power Laser Pulses with Matter

The physics involved in the interaction between light, matter, and plasma is complex and comprehensive descriptions are given for example in Refs [116–118]. In this work the interaction will be considered to start with the initial ionization and subsequent interaction of a high power laser pulse with isolated atoms or initially solid targets up to relativistic intensities. An often used natural baseline is the intensity necessary to separate the electron from the proton in the Bohr model of the Hydrogen atom by overcoming the electric field E_a between both charges. This gives the atomic intensity

$$I_a = \frac{\epsilon_0 c E_a^2}{2} \approxeq 3.51 \cdot 10^{16}\,\mathrm{Wcm}^{-2}, \tag{3.1}$$

where ϵ_0 is the vacuum permittivity and c the speed of light in vacuum.

At higher intensities field ionization of materials is very likely. Other atoms have lower first ionization potentials than Hydrogen, resulting in faster ionization. Further, the high ion density in solids can alter the binding energy, giving also lower ionization potentials. However, even far below this threshold ionization can occur due to multi-photon effects.

3.1.1. Ionization of Isolated Atoms

Depending intensity, different ionization mechanisms play a dominant role. If the photon energy is larger than the ionization potential, ionization can occur via the photoelectric effect. This is only rarely the case at optical wavelengths interacting with non-metals. Instead, multi-photon effects are dominant. Hereby a single electron absorbs multiple photons until it is lifted out of the potential well. This is the classical Multi-Photon Ionization (MPI). If the electron absorbs even more photons (which is more likely at higher intensity), it leaves the potential with significant kinetic energy. This process is then called Above Threshold Ionization (ATI).

The excess energy of the electron E_f can be calculated by an extended version of Einstein's formula [117, Chapter 2]:

$$E_f = (N + s)\hbar\omega - E_{\text{ion}} \tag{3.2}$$

with the number of photons necessary for MPI N, excess number of photons absorbed s, laser frequency ω, and ionization potential E_{ion}.

The onset of MPI occurs already at intensities below $10^{12}\,\text{Wcm}^{-2}$ [119]. The ionization rate scales with the laser intensity to the power of N, so MPI rates grow very quickly with the intensity. Whether the MPI or field ionization mechanism is dominant can be estimated by the Keldysh Parameter $\gamma = \omega_L\sqrt{m_e E_{\text{ion}}}/eE_L$ [120], where ω_L is the laser frequency, m_e the electron mass, E_{ion} the ionization potential of the material, e the elementary charge, and E the cycle averaged electric field of the laser. For $\gamma \gg 1$ the ionization is MPI dominated, for $\gamma \ll 1$ it is dominated by tunneling of the electrons through the potential barrier. This tunneling occurs when the laser field deforms the binding potential sufficiently, that the electrons have a significant probability to pass through the barrier.

Ionization cross-sections for MPI can be estimated from the Keldysh formalism [120]. Keldysh introduces an effective ionization potential $\tilde{E}_{\text{ion}}$ for a material with ionization potential E_{ion}

$$\tilde{E}_{\text{ion}} = \frac{2}{\pi}E_{\text{ion}}\frac{\sqrt{1+\gamma^2}}{\gamma}E\left(\frac{1}{\sqrt{1+\gamma^2}}\right). \tag{3.3}$$

Here E is the complete elliptic integral of the second kind defined as $E(x) = \int_0^{\frac{\pi}{2}}\sqrt{1 - x^2\sin^2\theta}d\theta$. Applying the MPI limit of $\gamma \gg 1$ allows for a simplified expression:

$$\frac{\sqrt{1+\gamma^2}}{\gamma} \approx 1 \tag{3.4a}$$

$$\frac{1}{\sqrt{1+\gamma^2}} \approx 0 \tag{3.4b}$$

$$E\left(\frac{1}{\sqrt{1+\gamma^2}}\right) \approx 1.6 \tag{3.4c}$$

$$\tilde{E}_{\text{ion}} \approx \frac{2\cdot 1.6}{\pi}E_{\text{ion}} \approx E_{\text{ion}} \tag{3.4d}$$

This means that in the MPI limit the effective ionization potential is just the standard ionization potential, as expected. The Keldysh expression for the ionization rate w is

$$
\begin{aligned}
w =& \frac{2}{9\pi}\omega_L \left(\frac{m_e\omega_L}{\hbar}\right)^{3/2} \Phi\left[\left(2\left\langle\frac{E_{\text{ion}}}{\hbar\omega_L}+1\right\rangle - \frac{2E_{\text{ion}}}{\hbar\omega_L}\right)^{1/2}\right] \\
& \exp\left\{2\left\langle\frac{E_{\text{ion}}}{\hbar\omega_L}+1\right\rangle\left(1-\frac{e^2E_L^2}{4m_e\omega_L^2E_{\text{ion}}}\right)\right\}\left(\frac{e^2E_L^2}{16m_e\omega_L^2E_{\text{ion}}}\right)^{\langle E_{\text{ion}}/\hbar\omega_L+1\rangle}.
\end{aligned}
\tag{3.5}
$$

$\langle x\rangle$ is in Keldysh's notation the integer part of x (i.e. rounding to the next lower integer), which means that $\left\langle\frac{E_{\text{ion}}}{\hbar\omega_L}+1\right\rangle$ is just the number of photons N necessary for the MPI process. With the definition of the Keldysh parameter, the second term in the exponential can be simplified as $\frac{e^2E_L^2}{4m_e\omega_L^2E_{\text{ion}}} = \frac{1}{4\gamma^2} \approx 0$. $\Phi(x) = e^{-x^2}\int_0^t e^{-t^2}dt$ is the Dawson function [121] and has to be evaluated numerically. With these simplifications the ionization rate is

$$
w = \frac{2}{9\pi}\omega\left(\frac{m\omega}{\hbar}\right)^{3/2}\Phi\left[\left(2N-\frac{2E_{\text{ion}}}{\hbar\omega}\right)^{1/2}\right]\exp\{2N\}\left(\frac{e^2F^2}{16m\omega^2E_{\text{ion}}}\right)^N. \tag{3.6}
$$

Using $I = \frac{1}{2}cn\epsilon_0E_L^2$, with speed of light c and refractive index n of the surrounding medium, the last term can be rewritten as

$$
\left(\frac{e^2E_L^2}{16m\omega^2E_{\text{ion}}}\right)^N = \left[8m\omega^2E_{\text{ion}}cn\frac{\epsilon_0}{e^2}\right]^{-N}I^N. \tag{3.7}
$$

Writing the ionization rate in the form of $w = \sigma_N I^N$ with an intensity independent cross-section σ_N, allows to finally identify

$$
\sigma_N = \frac{2}{9\pi}\omega\left(\frac{m\omega}{\hbar}\right)^{3/2}\Phi\left[\left(2N-\frac{2E_{\text{ion}}}{\hbar\omega}\right)^{1/2}\right]\exp\{2N\}\left[8m\omega^2E_{\text{ion}}cn\frac{\epsilon_0}{e^2}\right]^{-N}. \tag{3.8}
$$

As an example, Figure 3.1 shows the MPI ionization rates for two-, three-, and four-photon ionization of polystyrene calculated by this formula for typical laser intensities. The ionization potential of polystyrene is 4.05 eV [122].

For even higher intensities, approaching I_a, the laser field deforms the potential that confines the electron substantially. The electron can then tunnel through the potential well into free space, giving this process the name tunneling ionization. As mentioned above, the transition to this regime can be estimated by the Keldysh parameter $\gamma \ll 1$. The Keldysh parameter can also be written in terms of the intensity as

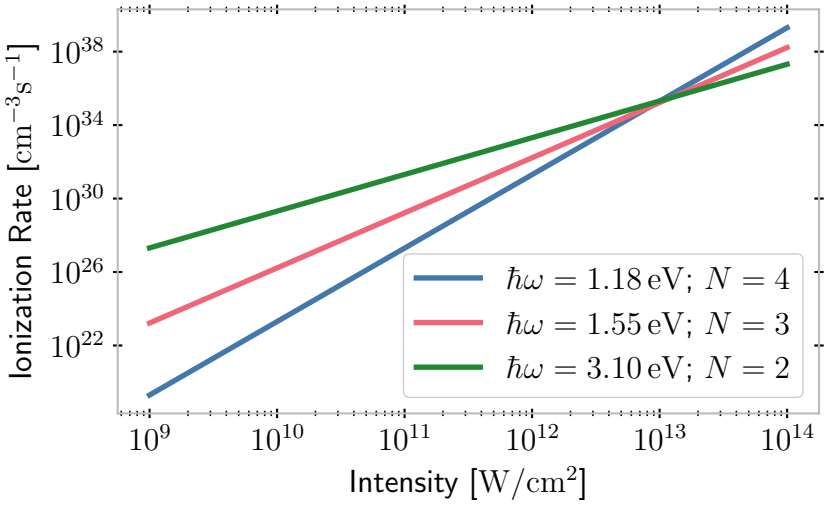

Figure 3.1.: **MPI Rates**
MPI rates calculated from the cross-section Equation (3.8) for a solid Polystyrene target ($E_{\mathrm{ion}} = 4.05\,\mathrm{eV}$ [122]) irradiated by three different laser wavelengths corresponding to two-, three-, and four-photon absorption.

$$\gamma = \omega_L \sqrt{\frac{2E_{\mathrm{ion}}}{I_L}} \sim \sqrt{\frac{E_{\mathrm{ion}}}{\Phi_{\mathrm{pond}}}} \tag{3.9}$$

with the ponderomotive potential

$$\Phi_{\mathrm{pond}} = \frac{e^2 E_L^2}{4m\omega_L^2}. \tag{3.10}$$

The ponderomotive potential is the cycle averaged kinetic energy of a free electron in a harmonic laser field with frequency ω_L and amplitude E_L.

For even higher intensities the laser field will become stronger than the field binding the electron to the nucleus. Tunneling ionization is then called Barrier Suppression Ionization (BSI) or Field Ionization (FI). Equating the electric field of the laser with the Coulomb barrier, the effective appearance intensity to create ions with charge state Z can be calculated as [117, Equation 2.9]

$$I_{\mathrm{app}} \simeq 4 \cdot 10^9 \left(\frac{E_{\mathrm{ion}}}{eV}\right)^4 Z^{-2}\mathrm{Wcm}^{-2} \tag{3.11}$$

For very short ($\sim 100\,\mathrm{fs}$) pulses and low density targets the BSI model shows very good agreement with experiments. At longer pulse durations ATI also plays a significant role. For high density matter (e.g. solids), collisional avalanche ionization quickly becomes dominant, as soon as a sufficiently large number of electrons is freed by MPI, ATI,

or BSI. In avalanche ionization the free electrons are accelerated in the laser field to energies above the ionization potential and then collide with bound electrons, freeing them. The growing number of free electrons then ionizes even more quickly, resulting in an exponentially rising ionization, similar to an avalanche.

In the regime of a high density plasma with sufficient initial ionization degree where a Local Thermal Equilibrium (LTE) is reached, the collisional ionization is described by the Saha-Boltzmann equation [117, Chapter 5]:

$$\frac{n_e n_{Z+1}}{n_Z} = \frac{g_{Z+1}}{g_Z} \frac{2m_e^3}{h^3} \left(\frac{2\pi T_e}{m_e}\right)^{3/2} \exp\left(-\Delta E_{Z+1}/T_e\right). \tag{3.12}$$

n_{Z+1}, n_Z are the ion densities of the charge states $Z+1$ and Z respectively, g_{Z+1}, g_Z are the statistical weights representing the degeneracy of the charge states, n_e the electron density, $\Delta E_{Z+1} = E_{\text{ion},Z+1} - E_{\text{ion},Z}$ the energy required to remove the $(Z+1)$th electron, m_e the electron mass, T_e the electron temperature, and h the Planck constant. A numerical solution of the Saha-Boltzmann equation is shown in Figure 3.2 for a hydro-carbon plasma at solid density.

The Saha-Boltzmann equation describes the ionization equilibrium which is established by the statistical collisions of the randomly moving electrons with the ions. For a non-LTE plasma, the description is more complex. In practice it is however still useful to employ the simplified model.

3.1.2. Laser-Induced Breakdown of Solids

When a laser pulse is interacting with a solid material rather than a low-density gas, the ionization can no longer be described by the single atom models. In a solid the atomic density is high enough, that the overlapping coulomb potentials significantly change the potential structure. In solid state physics this collective behavior is described by the band structure.

The different phenomena that occur after the interaction of a short laser pulse with a solid target are depicted in Figure 3.3. This behavior changes somewhat when the pulse duration becomes longer, as the mechanisms overlap.

For the optical properties of a solid the population density of electron in the conduction-band is decisive. In metals the fermi level lies above the conduction-band energy and the conduction-band is populated. The electrons in the conduction-band interact with electromagnetic radiation like quasi-free charges, so that metals interact with a laser similar to a plasma with strong reflection and absorption. In a metal the laser can

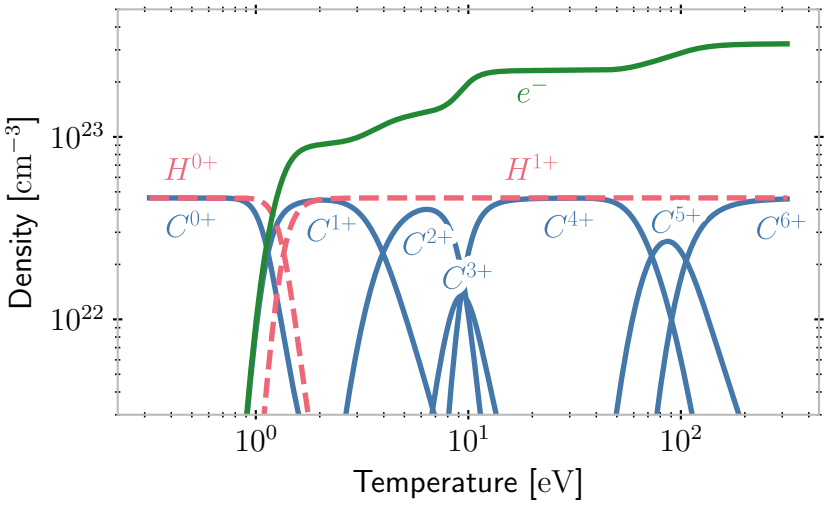

Figure 3.2.: **Ionization Equilibrium**
Ionization states calculated from the Saha equation. The material is an equal mixture of hydrogen and carbon atoms at 1 g/cm^3 mass density. The blue lines show the density of the different carbon charge states, the red dashed lines the density of hydrogen and the solid green line the total density of free electrons. Ionization potentials and statistical weights are taken from the CHIANTI [123, 124] database.

therefore directly drive conduction-band electrons which then transfer their energy to the lattice leading to a melting of the material [125].

In dielectrics on the other hand the conduction-band in the ground state is empty and separated from the valance-band by the so-called band-gap. Similar to the case of isolated atoms at moderate intensities, tunneling ionization and MPI [126] can populate the conduction band. Actual breakdown is typically defined as the point, where the density of (quasi-)free electrons reaches the critical density for the respective laser wavelength [122]. At this point the optical properties change abruptly and the target changes into a plasma state. This happens very shortly after the collisions with lattice ions heat the ions sufficiently to destroy the lattice and melt the target. For large enough electric fields, the ionization from MPI and tunneling only provides the initial seed electrons. The major contribution to the breakdown then comes from avalanche (impact) ionization. Electrons in the conduction-band are accelerated by the laser field to kinetic energies above the band-gap. They can then cause further ionization by collisions with valence electrons, causing an avalanche effect and increasing the electron population in the conduction band exponentially.

The most extensively studied material regarding the laser-induced breakdown of

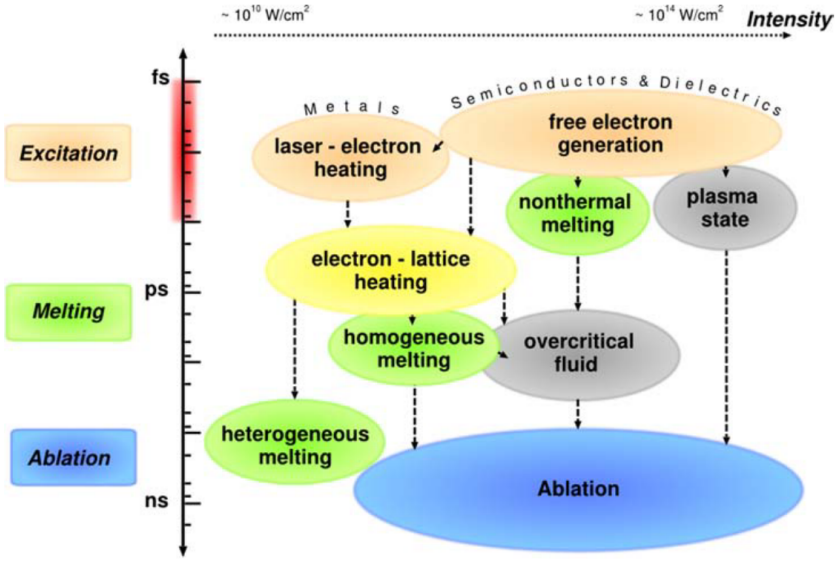

Figure 3.3.: **Laser-Induced Breakdown**
Typical phenomena occurring after the interaction of a solid with a short ($\sim 100\,\mathrm{fs}$) laser pulse (marked in red at the time scale) at different intensity and time scales. Figure copied from Ref. [125] under CC-BY 3.0.

dielectrics is fused silica (SiO_2) [127–131]. It has a band-gap of 9.0 eV. For long pulse durations τ>10 ps, the damage fluence increases approximately with the square root of the pulse duration. At short pulses, the experimental data deviates from this scaling law towards higher damage fluence. However, the breakdown always occurs at lower fluence then would be expected from just FI, also when taking into account the heating of the electrons by the laser once they are freed (see Figure 3.4). This gives experimental evidence, that the collisional avalanche ionization plays a crucial role in the breakdown.

When considering dielectric targets in ion acceleration experiments, the breakdown occurs either during a short pre-pulse or at some point during the rising edge of the laser pulse [132]. As the MPI rate depends on the properties of the material, it is not trivial to extrapolate damage fluence from one material to the next. In Table 3.1 the ionization cross-sections for MPI of different materials and wavelengths calculated from Equation (3.8) are listed.

A numerical model of the transition of a dielectric to a plasma (Solid-State Ionization (SSI)) has been developed by Duchateau et. al. [122] in the context of inertial confinement fusion. While this model has later been refined [133] to take into account chemical decomposition of the target, a better description of electron collisions, and more accurate equations of state, the simple original model provides a good estimate of breakdown

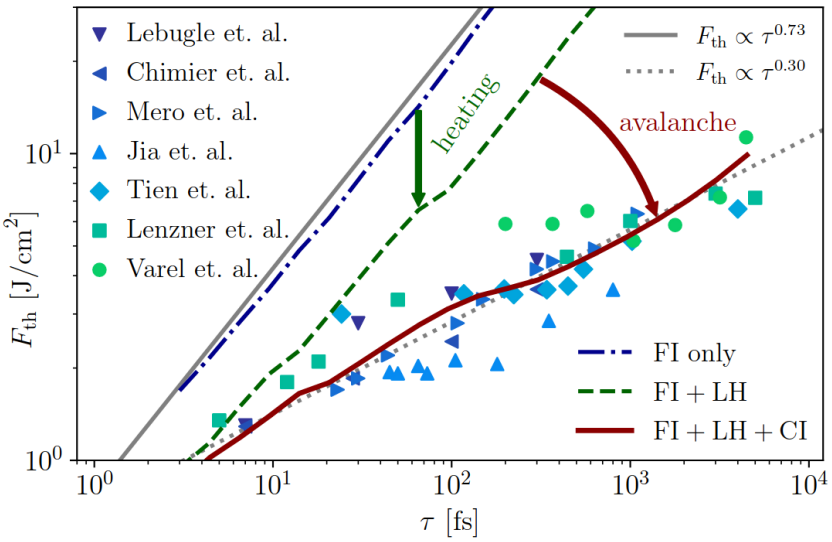

Figure 3.4.: **Breakdown Thresholds of SiO_2**
Breakdown fluence of fused silica compiled from multiple publications (markers) as well as different ionization models (lines) for a 800 nm pump laser. FI is field ionization, LH laser heating, and CI collisional ionization. Figure copied with permission from Ref. [131].

Wavelength [nm]	H (10.9 eV)	SiO_2 (9 eV)	Formvar (5.5 eV)	Polystyrene (4.05 eV)
1054 (1.18 eV)	$1.02 \cdot 10^{-101}\,I^{10}$	$1.67 \cdot 10^{-73}\,I^{8}$	$2.06 \cdot 10^{-31}\,I^{5}$	$2.09 \cdot 10^{-17}\,I^{4}$
527 (2.35 eV)	$3.86 \cdot 10^{-35}\,I^{5}$	$1.64 \cdot 10^{-20}\,I^{4}$	$1.49 \cdot 10^{-5}\,I^{3}$	$3.29 \cdot 10^{9}\,I^{2}$
351 (3.53 eV)	$8.17 \cdot 10^{-22}\,I^{4}$	$8.55 \cdot 10^{-7}\,I^{3}$	$9.68 \cdot 10^{8}\,I^{2}$	$1.62 \cdot 10^{9}\,I^{2}$
800 (1.55 eV)	$7.75 \cdot 10^{-76}\,I^{8}$	$2.51 \cdot 10^{-47}\,I^{6}$	$1.34 \cdot 10^{-18}\,I^{4}$	$1.74 \cdot 10^{-4}\,I^{3}$
400 (3.10 eV)	$1.91 \cdot 10^{-21}\,I^{4}$	$9.65 \cdot 10^{-7}\,I^{3}$	$1.09 \cdot 10^{9}\,I^{2}$	$2.09 \cdot 10^{9}\,I^{2}$
267 (4.64 eV)	$1.77 \cdot 10^{-7}\,I^{3}$	$1.42 \cdot 10^{8}\,I^{2}$	$5.81 \cdot 10^{8}\,I^{2}$	$3.20 \cdot 10^{23}\,I^{1}$

Table 3.1.: **Multi-Photon Ionization**
MPI rates in units of $cm^{-3}s^{-1}$ for typical target dielectrics at common laser wavelengths. H is here representing cryogenic hydrogen [126]. The wavelengths correspond to fundamental, second, and third harmonic of Nd:Glas and Ti:Sa corresponding to the PHELIX and ATLAS lasers respectively. The photon energies are given in the brackets of the left column and the bandgaps of the materials in the top row. To calculate the ionization rate the cross section is multiplied by the intensity to the power of number of photons necessary.

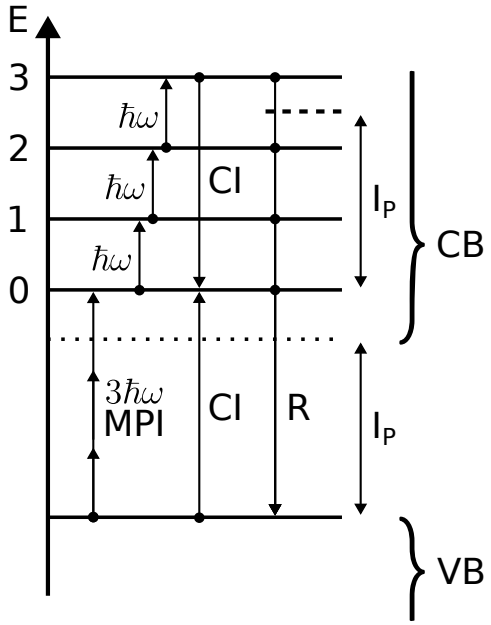

Figure 3.5.: **SSI Model**
Visualization of the band system and transition channels of the SSI model for four conduction band (CB) levels (0-3). The ionization potential I_P separates the valence (VB) and conduction bands. The lowest CB level (0) is reached by MPI of three photons ($3\hbar\omega$) from the VB. Subsequent levels (1-3) are spaced by $\hbar\omega$. The highest level (3) lies more than the ionization potential over level 0 and electrons in this level have sufficient energy to free new electrons by collisional ionization (CI). From any CB level recombination (R) is possible.

thresholds and describes the transition behavior. Its band structure and excitation and decay channels are sketched in Figure 3.5. Ionization from the valence band (VB) to the conduction band (CB) in this model is described on the one hand by the MPI cross-sections calculated by Equation (3.8). On the other hand, electrons in the conduction band can gain energy to ionize further valence electrons by collisional ionization (CI). To calculate the rate, the conduction band is modeled as a multi-level system, where each level $i = 0, ..., N$ is separated by the energy of a single photon $\hbar\omega$. The highest level N is separated from the lowest level 0 by more than the ionization potential I_P, so that electrons in this level have sufficient energy to free further electrons from the valence band by collisional ionization. Electrons are promoted from one level to the next by single-photon absorption. Recombination (R) can remove electrons from all levels and return them to the valence band. In addition to the electron density in the valence and conduction bands, the model also incorporates a two-temperature description of the electron and ion (lattice) temperatures. Here it is assumed that the ions are confined to a lattice up to a temperature of 0.1 eV, where the material is assumed to melt, destroying the lattice structure. The transition to the plasma state is defined as the point where the density of quasi-free electrons in the conduction band rises above the critical density for the applied laser.

For the case of a PS target irradiated by a 800 nm, $\hbar\omega = 1.55\,\text{eV}$ laser, the conduction band is described by rate equations for a four-level system:

$$\frac{\partial n_0}{\partial t} = AW_{\mathrm{MPI}} + 2A\tilde{\alpha}n_3 - W_1 n_0 - n_0/\tau_r, \tag{3.13a}$$

$$\frac{\partial n_1}{\partial t} = W_1 n_0 - W_1 n_1 - n_1/\tau_r, \tag{3.13b}$$

$$\frac{\partial n_2}{\partial t} = W_1 n_1 - W_1 n_2 - n_2/\tau_r, \tag{3.13c}$$

$$\frac{\partial n_3}{\partial t} = W_1 n_2 - A\tilde{\alpha}n_3 - n_3/\tau_r. \tag{3.13d}$$

The electron density in level $i = 0, 1, 2, 3$ is n_i and the total free electron density (i.e. number of electrons in the conduction band) $n_{\mathrm{fe}} = \sum_i n_i$. The factor $A = (n_{\mathrm{vb0}} - n_{\mathrm{fe}})/n_{\mathrm{vb0}}$ accounts for the depletion of the valence band with the initial density in the valence band $n_{\mathrm{vb0}} = 3 \cdot 10^{22}\,\mathrm{cm}^{-3}$. $W_1 = 2.3 \cdot 10^{-6}\,(\mathrm{V/m})^{-2}\mathrm{s}^{-1}E_L^2$ is the single photon absorption rate, $W_{\mathrm{MPI}} = \sigma_3 I^3 = 1.67 \cdot 10^{-4}\,\mathrm{s}^{-1}\mathrm{cm}^{-3}(\mathrm{W/cm}^2)^{-3}I^3$ the three-photon ionization rate, and $\tau_r = 1\,\mathrm{ps}$ the recombination time. The collision rate between free and valence electron is estimated as $\tilde{\alpha} = 10^{14}\,\mathrm{s}^{-1}$. The numerical values of the parameters are taken from [122], where the choices are motivated in detail. With these parameters the rate equations can be integrated numerically to yield the evolution of the free electron density for a given laser intensity profile.

The two-temperature model for the free electron and ion populations is used as described in Ref. [122] and the references therein. It is composed of two coupled equations for electron and ion temperatures

$$C_e \frac{dT_e}{dt} = \frac{\partial U}{\partial t} - \frac{3}{2}k_B \frac{dn_{\mathrm{fe}}}{dt}T_e - G(T_e - T_{il}), \tag{3.14a}$$

$$C_{il} \frac{dT_{il}}{dt} = G(T_e - T_{il}). \tag{3.14b}$$

$C_e = 3n_{\mathrm{fe}}k_B/2$ and $C_{il} = 3n_a k_B/2$ are the heat capacities for the electrons and ions. The additional term $3k_B\frac{dn_{\mathrm{fe}}}{dt}T_e/2$ is the change in heat capacity due to the increasing electron density in the conduction band. $G = C_e\nu_c m_e/m_{il}$ accounts for the heat transfer between electrons and ions due to collisions. As long as the material remains solid, heat transfer is mediated by electron-phonon collisions. In this case the collision frequency is $\nu_c^{\mathrm{sol}} = \nu_{\mathrm{ph}} = \nu_{\mathrm{ph0}}T_{il}/T_0$, where $\nu_{\mathrm{ph0}} = 10^{14}\,\mathrm{s}^{-1}$ is the collision frequency at room temperature $T_0 = 300\,\mathrm{K}$ [122]. For the full plasma state the Spitzer expression for the electron-ion collision frequency $\nu_{ei} = \frac{4\sqrt{2\pi}}{3}\frac{n_e e^4 Z \ln\Lambda}{m_e^2 v_e^3}$ [134, Eq. 5.10] is used. v_e is the

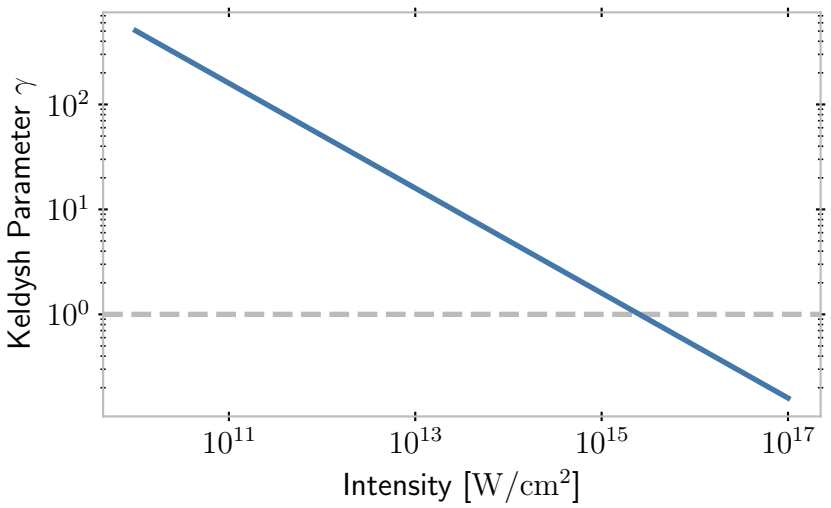

Figure 3.6.: **Keldysh Parameter**
Keldysh Parameter for Polystyrene ($E_g = 4.05\,\mathrm{eV}$) and $\hbar\omega = 1.55\,\mathrm{eV}$ photons for a range of intensities. The gray dashed line marks $\gamma = 1$.

thermal velocity of the electrons, Z the number of free electrons per atom, and $\ln\Lambda$ the Coulomb logarithm. As approximation $Z\ln\Lambda = 10$ is used. In the transition regime, the collision frequency is dominated by the mean free path length and an upper bound can be given as $\nu_{mpf} = v_e n_a^{1/3}$. $n_a = 3\cdot 10^{22}\,\mathrm{cm}^{-3}$ is the atomic density. Both regimes can be interpolated as $\frac{1}{\nu_c^{\mathrm{plas}}} = \frac{1}{\nu_{mfp}} + \frac{1}{\nu_{ei}}$ [122]. The mass ratio is $m_e/m_{il} = 1/1836$. The absorbed laser energy is calculated as [122]

$$\frac{\partial U}{\partial t} = \frac{e^2 n_{\mathrm{fe}} \nu_c}{m_e(\omega^2 + \nu_c^2)} E_L^2. \tag{3.15}$$

As the model relies on MPI as dominant ionization process, it is only valid for a Keldysh parameter $\gamma \gg 1$. Figure 3.6 shows that the Keldysh parameter for a polystyrene target irradiated with an 800 nm is > 1 for intensities as high as $10^{15}\,\mathrm{W/cm^2}$.

We model the laser rising edge as $I_{\mathrm{ASE}} + I_0\exp(t/\tau)$ (cp. Equation (2.2)) with $I_0 = 1.45\cdot 10^{15}\,\mathrm{W/cm^2}$ and $\tau = 4.8\,\mathrm{ps}$ the evolution of the free electron density is shown in Figure 3.7**a** for three different ASE intensities $I_{\mathrm{ASE}} = 1\cdot 10^{11}, 3.5\cdot 10^{11}, 5\cdot 10^{11}\,\mathrm{W/cm^2}$. Two extreme cases can be seen in the figure. For low ASE intensity, the MPI rate is balanced by recombination and the free electron density reaches an equilibrium below the critical density until the onset of the rising edge of the laser pulse, at which point the target quickly ionizes to a plasma state. For high ASE intensity, the target transitions directly at the onset of the ASE to a plasma state. In a narrow intermediate intensity range around $I_{\mathrm{ASE}} \sim 3.5\cdot 10^{11}\,\mathrm{W/cm^2}$ the ionization process takes a few hundred ps. This

indicates the existence of a sharp transition, where a small change in ASE intensity can have an immense impact on the ionization dynamics and subsequent plasma expansion. In Figure 3.7**b** the temperatures of the free electron population and the ion lattice are shown as calculated from the two-temperature model for the same intensity distributions. The melting point of PS is around $T_{il} = 0.1\,\mathrm{eV}$, so that for an ASE intensity of $1 \cdot 10^{11}\,\mathrm{W/cm^2}$ the lattice structure is expected to stay intact, while for higher intensities the material is melting already within the first few ps of the ASE. Comparing the temperatures with the free electron densities of Figure 3.7**a** it becomes apparent that the melting of the material happens before the free electron population reaches the critical density. However, as this parameter regime is very narrow, it is highly unlikely to achieve an experiment where the electron density stays below the critical density during the interaction with the ASE but the material is already molten. In practice it can therefore be assumed that the ASE either leaves the target structure intact or directly transitions it into the plasma state.

To quantify this transition, the equilibrium densities of free electrons that are reached after 400 ps of only ASE irradiation are calculated. They are shown in Figure 3.8 for two laser configurations, corresponding to the ATLAS and PHELIX systems. The relevant difference between the systems is here the wavelength of 800 nm and 1054 nm, respectively. This results in three-photon ionization for the ATLAS case and four-photon ionization for the PHELIX case. For the calculation of the four-photon ionization an additional intermediate level is introduced in the conduction band model, to account for the lower photon energy. Both configurations result in a similar form, with the transition intensity changing from $3.5 \cdot 10^{11}\,\mathrm{W/cm^2}$ to $4.8 \cdot 10^{11}\,\mathrm{W/cm^2}$ when changing from three- to four-photon ionization.

The SSI model can be compared to experimental observations of breakdown intensities. Wang et al. [135] measured damage thresholds for multiple materials irradiated by 800 nm laser pulses of varying pulse duration. To compare this data to the ASE threshold prediction of the model, Formvar and SiN targets irradiated with FWHM = 200 ps long pulses are considered. The measured breakdown intensities are $1 \cdot 10^{11}\,\mathrm{W/cm^2}$ and $2 \cdot 10^{10}\,\mathrm{W/cm^2}$ respectively, and the SSI model predicts $4.8 \cdot 10^{11}\,\mathrm{W/cm^2}$ and $3.2 \cdot 10^{11}\,\mathrm{W/cm^2}$. Here the model overestimates the breakdown intensity. On the other hand, the breakdown prediction of $1 \cdot 10^{12}\,\mathrm{W/cm^2}$ for cryogenic hydrogen is in good agreement with the measured value of Bernert et al. [126] of $2.4 \cdot 10^{12}\,\mathrm{W/cm^2}$ for a 6.4 ps long pulse. The overestimation is therefore not systematic for the model but more likely due to insufficient accuracy in the modeling the material properties and MPI process. However, the SSI model can still estimate the right order of magnitude for the breakdown

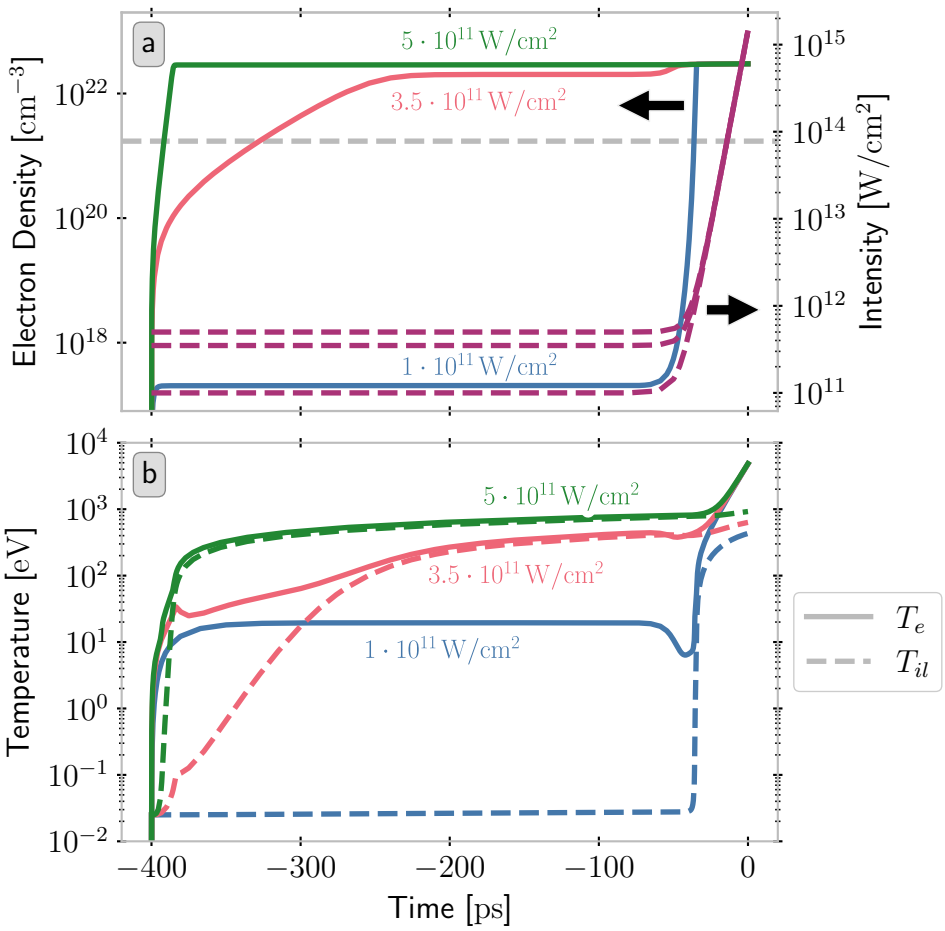

Figure 3.7.: **Free Electron Density and Temperatures of the SSI Model** Solution of the SSI model for three different ASE levels with otherwise constant laser and target parameters. The target is PS and the laser has a photon energy of $\hbar\omega = 1.55\,\mathrm{eV}$. In **a** the free electron density (solid lines, left axis) and laser intensity profile (violet dashed lines, right axis) is shown, in **b** the temperature of electrons (T_e, solid lines) and the ion lattice (T_{il}, dashed lines). The gray dashed line in **a** marks the critical density.

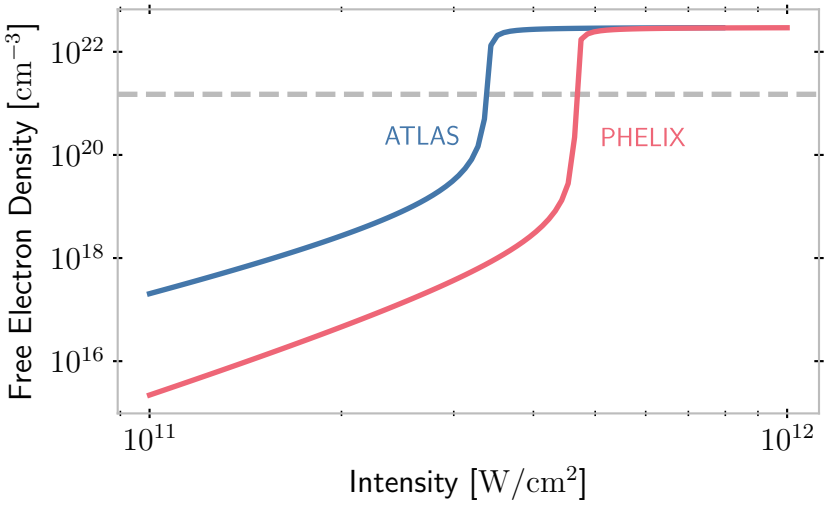

Figure 3.8.: **Equilibrium Electron Densities from the SSI Model**
Equilibrium free electron densities calculated for two different wavelengths of 800 nm (ATLAS) and 1054 nm (PHELIX). The gray dashed line indicates the critical density. The target is PS with a band-gap of 4.05 eV.

thresholds, in particular in configurations, where no experimental data exists.

In order to compare the expected breakdown intensity to real laser systems, it is overlaid over the measured temporal contrast of the ATLAS and PHELIX systems in Figure 3.9. For both systems the ASE level is below the threshold extracted from the SSI model. The rising edge of the ATLAS system passes the breakdown intensity at −40 ps before the main pulse, PHELIX at −100 ps. The rising edge of PHELIX furthermore extends to three orders of magnitude higher intensities, resulting in more than three orders of magnitude higher fluence accumulated on the target during this time.

Furthermore, both systems have short pre-pulses of similar intensity which might ignite a plasma. The one at ATLAS is 112 ps prior to the main pulse, the one at PHELIX at −211 ps. The intensity of these pre-pulses is of the order of the experimentally observed damage threshold for short pulses [135].

These considerations suggest that that in both laser systems the plasma will ignite earliest at the time of the short pre-pulse and latest at the beginning of the rising edge of the main pulse.

3.1.3. Plasma Collisions and Free Path Lengths

Collisions between plasma electrons and ions are necessary to achieve a thermalization of the different constituents. The rate with which these collisions occur in a large ensemble

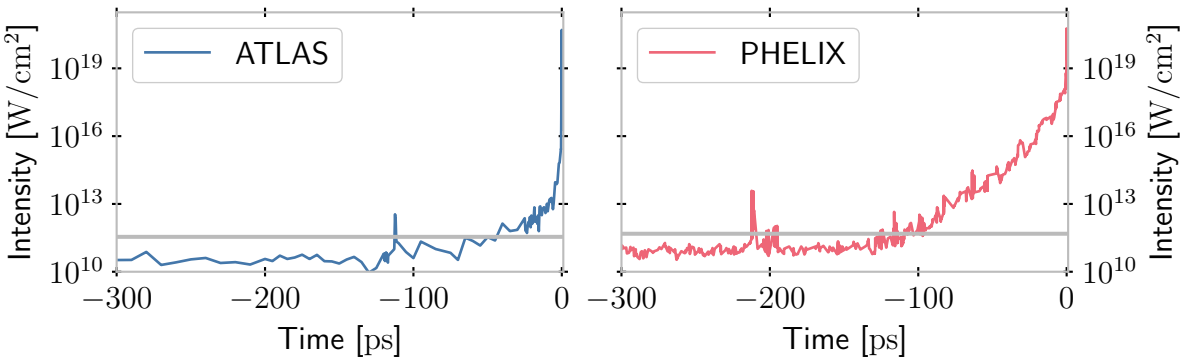

Figure 3.9.: **Temporal Contrast and Breakdown Thresholds**
Temporal contrast of two laser systems (ATLAS and PHELIX) measured by a third-order auto-correlator. The solid gray lines mark the breakdown intensity for PS as calculated in Section 3.1.2 with the SSI model for 800 nm and 1054 nm, corresponding to ATLAS and PHELIX wavelengths respectively. The peak intensities are $5.8 \cdot 10^{20}\,\mathrm{W/cm^2}$ for PHELIX and $5 \cdot 10^{20}\,\mathrm{W/cm^2}$ for ATLAS.

is described by the free path length l_e between collisions and collision frequency ν_{ei}.

The mean free path l_a of a particle a is determined by the cross section σ_{ab} of this particle to collide with a particle b with density n_b:

$$\mu_a = \frac{1}{l_a} = \sum_b n_b \sigma_{ab}. \tag{3.16}$$

The absorption coefficient μ_a is an equivalent quantity to the mean free path.

The collision frequency ν_{ab} depends additionally on the velocity $v_{ab} = |\vec{v_a} - \vec{v_b}|$ of particle a with respect to b.

$$\nu_{ab} = n_b \sigma_{ab} v_a = \frac{v_{ab}}{l_{ab}} \tag{3.17}$$

In a plasma the collisions are dominated by the Coulomb interaction between the charged constituents, mainly between electrons and ions. For electrons with a thermal Maxwellian velocity distribution, the thermal velocity is $v_{th,e} = \sqrt{2 k_\mathrm{B} T_e / m_e}$.

An estimate for the cross section can be made by using the classical closest approach l_{ca} defined by

$$\frac{Z e^2}{l_{ca}} = k_\mathrm{B} T_e. \tag{3.18}$$

The collision cross section is then approximated as

	Electron-Proton	Electron-Carbon
Mean Free Path l_{ei} [cm]	$4.41 \cdot 10^{-9}$	$4.91 \cdot 10^{-10}$
Collision Frequency ν_{ei} [s^{-1}]	$4.25 \cdot 10^{16}$	$3.82 \cdot 10^{17}$

Table 3.2.: **Collision Parameters**
Mean free path l_{ei} and collision frequency ν_{ei} of a H-C plasma at $k_\mathrm{B}T = 10\,\mathrm{eV}$.

$$\sigma_{ei} \approx \pi l_{ca}^2 = \frac{\pi Z^2 e^4}{(k_\mathrm{B}T_e)^2} \tag{3.19}$$

and the corresponding electron ion collision frequency as

$$\nu_{ei} \approx \frac{\sqrt{2}\pi Z^2 e^4 n_i}{\sqrt{m_e}(k_\mathrm{B}T)^{3/2}}. \tag{3.20}$$

From a more thorough treatment, a more accurate value can be derived [116]

$$\nu_{ei} = \frac{4(2\pi)^{1/2} Z^2 e^4 n_i \ln\Lambda}{3\sqrt{m_e}(k_\mathrm{B}T)^{3/2}} \approx 2.9 \cdot 10^{-6} \frac{Z^2 n_i[\mathrm{cm}^{-3}] \ln\Lambda}{(T_e[\mathrm{eV}])^{3/2}}\ [\mathrm{s}^{-1}] \tag{3.21}$$

The Coulomb logarithm $\ln\Lambda$ accounts for the limits of the scattering cross section b_{min} and b_{max}:

$$\Lambda = \frac{b_{max}}{b_{min}} = \lambda_D \frac{k_B T_e}{Ze^2} = \frac{9N_D}{Z}, \tag{3.22}$$

where $\lambda_D = \left(\frac{k_B T_e}{4\pi n_e e^2}\right)^{1/2} = \frac{v_{te}}{\omega_P}$ is the Debye length and $N_D = \frac{4\pi}{3}\lambda_D^3 n_e$ is the number of electrons in the Debye sphere.

For most plasma the Coulomb logarithm can be approximates as $\ln\Lambda \approx 10$.

As an example Table 3.2 shows the collision rates of electrons with a temperature of $k_\mathrm{B}T = 10\,\mathrm{eV}$ in a solid density ($1\,\mathrm{g/cm^3}$) hydro-carbon plasma (H:C = 1:1). The mean charge state of carbon at these conditions is C^{3+} (cp. Section 3.1.1). The ion density is $n_p = n_C \approx 4.63 \cdot 10^{22}\,\mathrm{cm}^{-3}$.

3.1.4. Absorption Mechanisms

Once the free electron density reaches the critical density, different mechanisms lead to absorption of laser light into the plasma. On a microscopic scale the plasma electrons interact with the field of the laser and transfer energy to the ions by collisions and

collectively formed electric fields. To estimate the absorption and differentiate between different regimes the following macroscopic descriptions of the interaction are useful.

At low to moderate intensities the dominant mechanism is collisional absorption [134, Chapter 5]. This process depends strongly on plasma density, temperature, and the quiver velocity $v_{os} = \frac{eE_0}{m_e \omega_L}$ [117, Eq. 2.19] of the electrons in the laser field. It is important to differentiate between the oscillation energy of the electrons, which already reaches 1 keV for $I\lambda^2 = 10^{16}\,\mathrm{W/cm^2 \mu m^2}$, and the thermal (random) motion $v_{th} = \sqrt{\frac{3k_\mathrm{B}T_e}{m_e}}$ due to the electron temperature, which is much smaller. The parameter determining collisional absorption is the electron ion collision frequency ν_{ei} of Equation (3.21).

Normalizing the collision frequency on the frequency of the laser ω: $\tilde{\nu} = \nu_{ei}/\omega$, the dielectric constant ϵ or the refractive index n is given for a spatially varying density profile as:

$$\epsilon(x) = n^2(x) = 1 - \frac{n_0(x)/n_c}{1 + i\tilde{\nu}(x)} \tag{3.23}$$

For some special density profiles a direct form for the absorption dependent on the scale length L can be given. Otherwise numeric integration is also a viable option.

For example, in the long scale length limit the absorption in an exponential density profile with angle of incidence θ is [136, Chapter 5]

$$\eta = 1 - \exp\left(-\frac{8\nu_{ei}L}{3c}\cos^3\theta\right). \tag{3.24}$$

Already at $I \sim 10^{15}\,\mathrm{W/cm^2}$ the collisional absorption starts to become ineffective, as the plasma temperature rises [137]. The laser then penetrates up to or further than the critical density. Depending on the scale length of the plasma density gradient, mechanisms become dominant.

For a very short scale length and high intensities the plasma is heated by the interaction of the laser with the surface electrons. This process was first described by Brunel in 1987 [138]. In a plasma irradiated by p-polarized light with very sharp density gradients $L < v_{os}/\omega$, electrons at the boundary are torn out of the plasma by the intense light field and fired back inside. As the laser field only penetrates a short skin depth $\sim c/\omega_p$, the electrons escape the decelerating field and can propagate far into the plasma where their energy is eventually absorbed by collisions. As the absorption happens at the plasma-vacuum interface, this process is often called vacuum heating.

Assuming these electrons are completely escaping the laser field into the solid, a fractional absorption rate of

$$\eta_a = \frac{4}{\pi} a_0 \frac{\sin^3\theta}{\cos\theta} \tag{3.25}$$

can be calculated [117, Eq. 5.66] with $a_0 = v_{os}/c$. Without corrections, this expression would predict absorption of more than 100 % for large enough angle of incidence or laser intensity $I\lambda^2 \propto a_0^2$.

In the limit of low intensity ($a_0 \ll 1$), the absorption η can be expressed with the correction factor $f = 1 + (1 - \eta_a)^{1/2}$ as [117, Eq. 5.69]:

$$\eta^{low} = \frac{a_0}{2\pi} f^3 \frac{\sin^3\theta}{\cos\theta} \tag{3.26}$$

In a strongly relativistic limit ($a_0 \gg 1$), the absorption is [117, Eq. 5.70]

$$\eta^{rel} = \frac{4\pi\alpha'}{(\pi + \alpha')^2} \tag{3.27}$$

with $\alpha' = \sin^2\theta/\cos\theta$.

In resonant absorption a p-polarized laser field excites a plasma wave resonantly at the critical surface. The wave is then damped by collisions or wave breaking. A laser incident with an oblique angle is actually reflected before it reaches the critical surface. However, part of the field tunnels up to the critical surface where it excites the wave. After more detailed treatment [117, Chapter 5], the absorption can be calculated in a self-similar parameter $\xi = (kL)^{1/3}\sin\theta$ with $k = 2\pi/\lambda$, $L^{-1} = \frac{d}{dx}\log N_e|_{x=x_c}$ and angle of incidence θ.

The absorption is then

$$\eta = \frac{1}{2}\Phi^2(\xi) \tag{3.28}$$

with

$$\Phi \approx 2.3\xi \exp\left\{-2\xi^3/3\right\}. \tag{3.29}$$

The peak absorption is typically in the range of $\eta = 0.5 - 0.6$. In Ref. [139] a comprehensive simulation overview over absorption at different intensity and length scales is given. The peak value is at 75 % for $L/\lambda = 0.1$ and $I\lambda^2 = 10^{16}\,\mathrm{W/cm^2\mu m^2}$.

As the dominant absorption mechanism changes with intensity and scale length and the absolute value of absorption varies strongly with intensity, polarization, and angle of incidence, it is practically impossible to calculate the expected absorption for realistic laser parameters and geometries in a macroscopic picture. In order to get quantitative

absorption values, microscopic simulations are necessary.

3.1.5. Thermodynamic Equilibrium

As briefly mentioned above, the Saha equation is only valid for a plasma in LTE. It is therefore necessary to investigate the different possible equilibrium states and under which conditions they can be reached.

In the most restrictive case the system is in full thermodynamic equilibrium (also called detailed balance). It is then characterized by a small number of thermodynamic parameters, e.g. temperature T, pressure p and chemical potential μ. Detailed balance means all processes are in balance with their respective counter process, e.g. photo-ionization with radiative recombination. In this case the particle velocities are Maxwell distributed, the energy levels Boltzmann distributed, the emitted radiation given by the Planck formula for black bodies, and the ionization given by the Saha equation. All these balances are completely determined by the temperature.

In a real plasma these conditions are typically not fulfilled, as pressure and temperature gradients exist. If the gradient lengths are much larger than the free path lengths of particles and photons, a LTE exists. This is often the case in high density plasmas, where collisional processes establish the equilibrium. In this case the plasma can be described locally as an equilibrium state.

Even if the free path length of photons is larger, Maxwell- and Boltzmann-distributions and Saha equation might still be applicable if the collision rate is sufficiently high. However, the plasma is then no longer in radiative equilibrium. The emitted power is in this case not given by the Planck formula, but must be calculated from the transport equation (3.39).

For a thinner plasma with low collision frequency, the detailed balance of the ionization processes is no longer given and the plasma becomes non-thermal. The balance that forms then is known as Coronal equilibrium, as it was first described for the Suns corona. Ionization degrees and radiation emission can then be calculated from detailed rate equations taking into account all possible ionization and recombination processes with the corresponding cross sections and quantum levels.

In the case of laser-driven ion acceleration the plasma is typically dense as it is rapidly formed from a solid material. The temperature of the plasma electrons rises over the time of a few 10 ps-100 ps from meV to several keV. Therefore, at the early interaction, the assumption of a LTE is often valid, or at least only photons become non-thermal. At later times the electrons do not thermalize quickly enough and often form two populations

with different distribution functions, breaking the equilibrium description. However, at such times the plasma dynamics is mostly dominated by the laser field and kinetic descriptions of the electron and ion movements provide good approximations.

3.1.6. Radiative Processes in Plasmas

In order to calculate the radiation field inside a plasma and the energy that is lost from an isolated plasma due to radiation, it is instructive to first consider the different processes that emit or absorb radiation inside a plasma. For a more thorough treatment see e.g. Refs. [116, 140].

On a microscopic level there are three kinds of electronic transitions that can emit or absorb radiation in a plasma: bound-bound (bb), bound-free (bf), and free-free (ff).

Bound-bound transitions are interactions where an electron changes from one bound state to an other. As these bound states are discrete, the emission/absorption spectrum also shows discrete peaks. The emission from this process is then called line emission and the corresponding absorption process is line absorption.

When an electron is freed from the ion or recombines from the continuum, the process is bound-free. The absorption of a photon to free an electron from the ion is the photoelectric effect, also often called photoionization. The inverse process where an electron joins an ion in a bound state and emits a photon is radiative recombination.

Free-free transitions are collisions of electrons with ions without ionization or recombination. This process is bremsstrahlung and can either emit or absorb (inverse bremsstrahlung) a photon, depending on the collision parameters.

In general it is necessary to solve detailed rate equations for these processes with the material dependent cross sections and atomic properties in order to calculate the radiation field inside a plasma. However, in the case of a plasma in thermodynamic equilibrium, all processes are in equilibrium with their corresponding inverse. This means that the numbers of emitted and absorbed photons per unit volume and time are equal. The radiation field then only depends on the temperature T of the plasma and is given by the Planck functions for the spectral energy density scalar $U_{\nu P}$ and spectral radiation intensity $I_{\nu P}$:

$$I_{\nu P} = \frac{2h\nu^3/c^2}{\exp(h\nu/k_\mathrm{B}T) - 1} \tag{3.30}$$

$$U_{\nu P} = \frac{4\pi I_{\nu P}}{c}. \tag{3.31}$$

h is the Planck constant, c speed of light in vacuum, and k_B the Boltzmann constant.

The spectral radiation intensity I_ν describes the radiation energy per unit frequency crossing a unit area in unit time in one direction Ω. The spectral energy scalar $U_\nu = c^{-1} \int I_\nu \mathrm{d}\Omega$ is related to it by integration over the direction. For an isotropic radiation intensity, such as in a thermodynamic equilibrium, this integration yield the factor of 4π.

Integration of the spectral energy density over the frequency ν and half solid angle (one hemisphere) yields the Stefan-Boltzmann law for the one-sided (directed) flux F with the Stefan-Boltzmann constant σ_SB:

$$F = \sigma_\mathrm{SB} T^4 \tag{3.32}$$

$$\sigma_\mathrm{SB} = \frac{2\pi^5 k_\mathrm{B}^4}{15h^3c^2} = 5.6705 \cdot 10^{-8}\,\mathrm{J/m^2{\cdot}s \cdot K^4}. \tag{3.33}$$

Inside a plasma in equilibrium the incoming and outgoing flux at any surface are equal and the total flux is therefore zero. However, Equation (3.32) describes the outgoing flux at a (sharp) plasma boundary, where there is no returning flow and the equilibrium is broken.

A plasma in equilibrium is by definition optically dense, i.e. any emitted photon is quickly absorbed and only photons emitted at the boundary can escape the plasma. The opacity of a plasma κ_ν is defined as

$$\kappa_\nu = \frac{1}{l_\nu} = \sum_j n_j \sigma_{\nu j}, \tag{3.34}$$

where l_ν is the mean free path, n_j the density of particles of type j and $\sigma_{\nu j}$ the cross section for absorption or scattering. κ_ν has units of $\mathrm{cm^{-1}}$ and is a measure for the absorption in the plasma. The cross sections for bound transitions depend strongly on the atomic properties of the ion species, but the cross section for free-free processes can be calculated more easily. For example, the cross section of inverse bremsstrahlung (IB) is

$$\sigma_{\mathrm{ff}}^{\mathrm{IB}}(\nu) = \left(\frac{2^8\pi\alpha}{3\sqrt{3}}\right)(n_e a_{\mathrm{B}}^3)\left(\frac{I_{\mathrm{H}}}{k_{\mathrm{B}}T}\right)^{1/2}\left(\frac{I_{\mathrm{H}}}{h\nu}\right)^3 Z_{\mathrm{i}}^2 a_{\mathrm{B}}^2. \tag{3.35}$$

$\alpha = 1/137$ is the fine structure constant, $a_B = 5.29 \cdot 10^{-11}\,\mathrm{m}$ the Bohr radius, $I_H = 13.6\,\mathrm{eV}$ the ionization potential of Hydrogen and Z_{i} the ion charge state.

As most simple case for a bound-free transition it is also possible to calculate a cross section for the photoelectric effect (PE) for hydrogen-like atoms

$$\sigma_{\mathrm{bf}}^{\mathrm{PE}}(\nu) = \begin{cases} \left(\dfrac{64\pi^4 e m_e Z_{\mathrm{i}}^4}{3\sqrt{3}h^6 c n^5}\right)\dfrac{1}{\nu^3} \approx 7.9\cdot 10^{-18}\left(\dfrac{n}{Z_{\mathrm{i}}^2}\right)\left(\dfrac{I_{\mathrm{n}}}{h\nu}\right)^2\,[\mathrm{cm}^2] & h\nu > I_{\mathrm{n}} \\ 0 & h\nu < I_{\mathrm{n}}. \end{cases} \tag{3.36}$$

It is also possible to calculate the cross-sections for the MPI ionization processes for the part of the radiation spectrum with photon energies below the ionization potential the same way as in Section 3.1.1. However, these cross-sections are always smaller than the direct photoelectric effect and therefore negligible when considering leading order effects.

Counteracting the absorption described by the opacity are spontaneous and stimulated emission described by the emissivity j_ν [J/m^3], which depends on the atomic properties of the medium, degree of ionization, and temperature. Spontaneously emitted energy is defined as [116, Eq. 2.72]

$$\frac{\mathrm{d}E_{\mathrm{spon}}}{\mathrm{d}V\mathrm{d}t} = j_\nu \mathrm{d}\nu\mathrm{d}\mathbf{\Omega}, \tag{3.37}$$

and the energy emitted by stimulated emission as [116, Eq. 2.73]

$$\frac{\mathrm{d}E_{\mathrm{stim}}}{\mathrm{d}V\mathrm{d}t} = j_\nu\left(\frac{c^2 I_\nu}{2h\nu^3}\right)\mathrm{d}\nu\mathrm{d}\mathbf{\Omega}. \tag{3.38}$$

With these definitions, the spatio-temporal evolution of the radiation intensity I_ν is described by the transport equation [116, Eq. 2.77]

$$\frac{1}{c}\left(\frac{\partial I_\nu}{\partial t} + c\mathbf{\Omega}\cdot\nabla I_\nu\right) = j_\nu\left(1 + \frac{c^2 I_\nu}{2h\nu^3}\right) - \kappa_\nu I_\nu. \tag{3.39}$$

I_ν is a general spectral radiation intensity. In the case of a thermodynamic equilibrium this is given by the Planck spectral radiation intensity $I_{\nu P}$ (Equation (3.30)).

The emissivity j_ν can be estimated in a thermal equilibrium, as in this case the

ratio of spontaneous emission and absorption is a universal function of frequency and temperature:

$$\frac{j_\nu}{\kappa_\nu} = \frac{2h\nu^3}{c^2}\exp\left(-\frac{h\nu}{k_\mathrm{B}T}\right) = I_{\nu P}\left[1-\exp\left(-\frac{h\nu}{k_\mathrm{B}T}\right)\right] \tag{3.40}$$

$$j_\nu = \kappa'_\nu I_{\nu P} \tag{3.41}$$

$$\kappa'_\nu = \kappa_\nu\left[1-\exp\left(-\frac{h\nu}{k_\mathrm{B}T}\right)\right] \tag{3.42}$$

This is known as Kirchhoff's law and is based on the detailed balance between emission and absorption. It is valid even when the plasma is not in equilibrium, it only requires that a temperature T for the medium can be defined.

Kirchhoff's law allows to estimate the emissivity from the opacity and links it thereby to the cross sections of the different processes. For a finite low opacity plasma in which bound-bound and bound-free transitions play a significant role, it is therefore necessary to know the atomic structure of the constituents for a correct calculation of the radiation field.

As a lower bound for the total radiated power, the power radiated due to bremsstrahlung can be calculated as [140, Chapter 5]

$$\frac{dP(\lambda,T)}{d\lambda} = C_\mathrm{ff}\frac{N_e e^{-u}}{\lambda^2 T^{1/2}}\sum_{Z,z} N_{Z,z} z^2 \bar{g}_\mathrm{ff}\ \mathrm{J\ m^{-3}s^{-1}nm^{-1}}. \tag{3.43}$$

Here the photon wavelength λ is in nm, N_e is the electron density in $\mathrm{m^{-3}}$ and $N_{Z,z}$ the ion density of atomic number Z and effective charge state

$$z = n_0\left(\frac{I_{Z,z-1,n_0}}{I_\mathrm{H}}\right)^{1/2}. \tag{3.44}$$

I_H is the ionization energy of hydrogen and $I_{Z,z-1,n_0}$ the ionization energy of the excited state with quantum number n_0. The parameter u is given by

$$u = \frac{h\nu}{k_\mathrm{B}T} \tag{3.45}$$

and the constant C_ff by

$$C_\mathrm{ff} = 4\pi\frac{16}{3}\left(\frac{\pi}{6}\right)^{1/2}\frac{e^6 10^8}{c^2 m_e^{3/2} k_\mathrm{B}^{1/2}} = 2.051\cdot 10^{-19}. \tag{3.46}$$

$\bar{g}_{\mathrm{ff}}(z, \lambda, T)$ is the time averaged free-free hydrogenic gaunt factor for ions with charge Z. For a low-Z plasma at high temperatures it can be approximated by

$$\bar{g}_{\mathrm{ff}} = \frac{\sqrt{3}}{\pi} e^{u/2} K_0(u/2), \tag{3.47}$$

where K_0 is the modified Bessel function of the second kind.

Depending on the opacity, the energy an isolated plasma looses due to radiation can either be calculated from the Stefan-Boltzmann law (Equation (3.32)) or the power radiated by bremsstrahlung (Equation (3.43)). Both of these descriptions represent extreme cases, which are in practice smoothly connected. However, as this transition is complex to describe, with the opacity varying over the spectrum of the radiation and the spectrum shifting with temperature, selecting the appropriate extreme case as approximation is a necessary choice to simplify calculations.

3.2. Model of Long-Pulse Driven Expansion

To differentiate between the effect of the short pre-pulse and the rising edge, the model for the expansion will initially only consider the rising edge, and be expanded to include the pre-pulse in the next section (3.3). This is motivated by the fact that it is typically possible to remove pre-pulses from a laser-system by detailed analysis of the used optical components and removal of unwanted reflections, while changing the long rising edge is not so simple.

In a first step, an analytic approximation of the temporal evolution of the laser pulse is necessary, to allow for an easier numeric solution of the differential equations. For this the parametrization of the laser pulse Equations (2.2) to (2.3d) is used.

The measured intensity as well as the model over the last 90 ps before the main pulse is shown in Figure 3.11 for ATLAS (**a**) and PHELIX (**b**) parameters.

As mentioned Section 3.1.2, in both laser systems the ASE level is below the breakdown value. In the absence of pre-pulses with sufficient intensity to ionize the target, the breakdown will therefore occur at the beginning of the rising edge of the pulse when the intensity reaches $\sim 5 \cdot 10^{11}\,\mathrm{W/cm^2}$.

For the description of the interaction, the assumption of a constant absorption coefficient is made as an simplification, as the detailed mechanisms could only be modeled in extensive simulation codes. The absorption occurs over the cross-section of the target. As the absorption in a dense plasma (above the critical density) is much higher than in a thin

plasma, a good approximation is to use the critical density surface for the cross-section calculation. Therefore, the total power absorbed by the plasma P_{abs} will vary with the intensity and spatial extent as

$$P_{\text{abs}}(t) = \eta A_{\text{cross}}(t) I(t). \tag{3.48}$$

A_{cross} is the cross section area and η the absorption coefficient.

This energy is first absorbed by the electrons and then either ionizes atoms further via collisional ionization, as described by the Saha equation, or diffuses and increases the overall temperature of the plasma. As the pulse is assumed to change slowly over collision and thermalization time-scales (cp. also Section 3.1.3), the plasma is assumed to be in LTE and the Saha equation (Equation (3.12)) can be solved for each time step to yield the ionization equilibrium.

As the plasma is small and spatially isolated, energy lost due to radiation can have a significant contribution to the total energy balance. In the model this radiated power P_{rad} can be described by the two extreme cases of either an optically dense plasma with the Stefan-Boltzmann law (Equation (3.32)) and using the area of the critical surface as radiating area, or an optically thin plasma (Equation (3.43)) with infinite photon path length, which radiates bremsstrahlung. As the opacity of the plasma changes with density and temperature, it is not constant over the interaction and can also generally vary within the plasma. Higher density increases the opacity, while higher temperature typically reduces the cross-sections, depending on the dominant processes. Hence, the opacity of an initially cold high density plasma expanding and being heated will reduce during the interaction with the laser pulse. Therefore, it can be expected that in the initial phase the description of a black body will be a good approximation, while at later times the description using bremsstrahlung loss should become a better fit.

For the work performed by the expansion an adiabatic equation of state is assumed

$$VT^{\gamma-1} = \text{const.} \tag{3.49}$$

with $\gamma = 5/3$ for an ideal free electron gas. The work performed per unit time is then

$$\begin{aligned} P_{\text{ad}} &= \frac{\partial k_B T}{\partial t} = \frac{\partial k_B T}{\partial V}\frac{\partial V}{\partial R}\frac{\partial R}{\partial t} \\ &= \frac{k_B T}{V}(\gamma - 1) c_s (k_B T)\frac{\partial V}{\partial R}, \end{aligned} \tag{3.50}$$

with the speed of sound $\frac{\partial R}{\partial t} = c_s(k_B T)$.

This allows the complete system to be described by one differential equation for the temperature, collecting the different energy gain and loss mechanisms

$$\frac{\partial kT}{\partial t} = \frac{2}{3N}(P_{\text{abs}} - P_{\text{rad}} - P_{\text{ad}}). \tag{3.51}$$

Combining the different terms, Equation (3.51) becomes

$$\begin{aligned}\frac{\partial kT}{\partial t} =& \frac{2}{3N}\left[\eta A_{\text{cross}} I(kT, n_e, R) - P_{\text{bb/ff}}(kT, n_e, n_i, R)\right] \\ &+ \frac{kT}{V}(1-\gamma)c_s(kT)\frac{\partial V}{\partial R},\end{aligned} \tag{3.52}$$

with $P_{\text{bb/ff}}$ being the loss by Blackbody or Bremsstrahlung radiation respectively.

This expansion model assumes a single fluid quasi-neutral description, which combines electrons and ions. To investigate the applicability of this approach, the two-temperature model of Equations (3.14a) and (3.14b) is used without laser irradiation ($\frac{\partial U}{\partial t} = 0$) or change of ionization ($\frac{dn_{\text{fe}}}{dt} = 0$) to estimate the thermalization time of the plasma. If this time is shorter than the times over which the temperature changes due to the laser irradiation, the single fluid approach is assumed to be applicable. For an initial ion temperature of $k_{\text{B}}T_{il} = 0.2\,\text{eV}$ and three densities $n_e = 1, 10, 100\,\text{nc}$ the thermalization times over electron temperature $k_{\text{B}}T_e$ are shown in Figure 3.10.

For a highly overcritical ($n_e > 10\,\text{n}_\text{c}$) plasma the thermalization time is in the 1 ps-10 ps range up to an electron temperature of $k_{\text{B}}T_e \approx 100\,\text{eV}$. For a critical density plasma the thermalization time remains at 20 ps up to $k_{\text{B}}T_e \approx 30\,\text{eV}$. For higher temperatures the thermalization times increase strongly, as the collision frequency drops (see Equation (3.21)). For $n_e = 1\,\text{n}_\text{c}$ and $k_{\text{B}}T_e = 1\,\text{keV}$ the thermalization time reaches 1 ns.

As the expansion model describes an initially solid density plasma over tens to hundreds of ps, and the laser intensity also varies over the tens of ps time scale, we assume the single fluid approach to be valid up to temperatures of $\sim 100\,\text{eV}$. At higher temperatures or more rapidly changing laser intensities, the plasma thermalization is not fast enough and a two fluid description would be necessary.

The density model for the numerical solution to Equation (3.52) is a sphere with constant density $n = N/V$ for $r < R$ and zero density otherwise. This model simplifies the definition of the relevant areas and volumes by neglecting surface layer effects. The

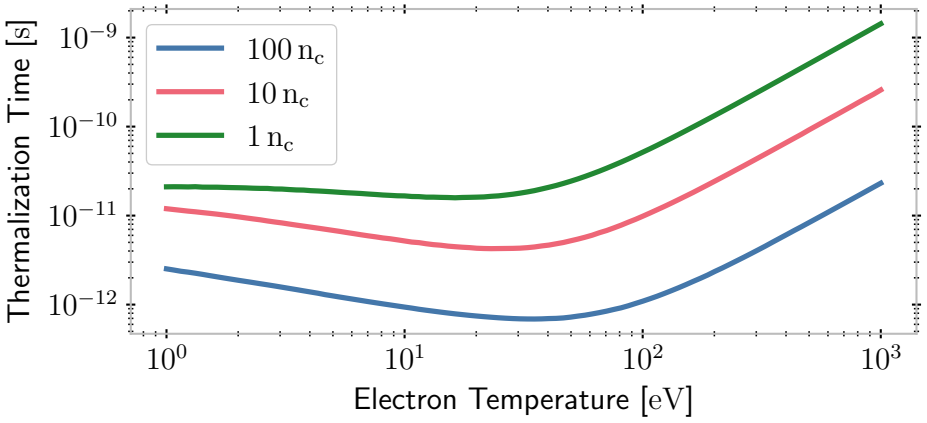

Figure 3.10.: **Plasma Thermalization Times**

areas and volumes are then:

$$A_{\text{cross}} = \pi R^2; \qquad A_{\text{surf}} = 4\pi R^2; \qquad V = \frac{4}{3}\pi R^3; \qquad \frac{\partial V}{\partial R} = 4\pi R^2 \tag{3.53}$$

In this model the absorption of the laser will drop abruptly to zero once the density falls below the critical density for the laser driver (for ATLAS at $\lambda = 800\,\text{nm}$ $n_c = 1.72 \cdot 10^{21}\,\text{cm}^{-3}$ and for PHELIX at $\lambda = 1054\,\text{nm}$ $n_c = 1.11 \cdot 10^{21}\,\text{cm}^{-3}$). In reality this transition will be smoothed by a gradual shrinking of the critical surface area during the expansion of the real plasma density profile. Also there will remain some absorption in the subcritical density plasma volume, which is neglected here. For the numerical solution an absorption coefficient of $\eta = 0.1$ is assumed as approximation of the different absorption mechanisms.

In Figure 3.11**c** the numerically calculated evolution of the plasma temperature is shown for both laser systems, once assuming Black-Body radiation and once assuming Bremsstrahlung radiation. Both models are shown as extreme cases, as a correct description of the opacity of the plasma as mentioned above is beyond this model. The ionization in **d** follows the temperature evolution as dictated by the Saha equation. Figure 3.11**e** shows the evolution of the plasma density, with the corresponding radius of the distribution shown in **f**. In the temperature plot, the point at which the plasma density falls below the critical density for the PHELIX laser is clearly visible as a sharp bend. This is due to the flat-top density profile assumption, which means that at this point the absorption suddenly vanishes. In the density profile, different phases can be identified. Initially the free electron density increases. In the following phase it is heated to follow the laser intensity and the ionization due to this heating increases the electron

density. After this, the ionization due to the rising temperature is able to compensate for the expansion of the plasma and the density remains constant while the intensity increases. Only after the ionization reaches the C^{4+} state this equilibrium is broken and the density decreases with the ever faster increasing radius. The expansion only slows down again after the plasma has become transparent and the radiative losses cool it.

3.3. Inclusion of Short Pre-Pulses

Pre-pulses are typically weaker copies of the main pulse, and have therefore a similar pulse duration. The effect of the pulse is assumed to be instantaneous ionization and isochoric heating depending on its peak intensity. Subsequent expansion can then be modeled in a self-similar manner assuming an adiabatic equation of state ($VT^{\gamma-1} = \text{cnst.}$ with $\gamma = 5/3$) and including radiative losses.

The experiments performed at ZEUS [75] showed, that the assumption of a self-similar plasma shape with spherical symmetry at long times after the interaction with the pulse is a valid description. Furthermore, they provide an experimental measurement of the expansion velocity and thereby for the temperature of the plasma. At a laser intensity of $I_{\mathrm{PP}} = 1 \cdot 10^{16}\,\mathrm{W/cm^2}$ the measured expansion velocity is $c_s = 3\,\mu\mathrm{m/ps}$. This is in good agreement with the numerical scaling derived in Ref. [141]:

$$c_s(I_{\mathrm{PP}}) = A \cdot \sqrt{I_{PP}} + B \tag{3.54}$$

with $A = 7 \cdot 10^{-8} d_0^{-1/2} \frac{\mu\mathrm{m/ps}}{\sqrt{\mathrm{W/cm^2}}}$ and $B = 2.4 \cdot 10^{-3}\,\mu\mathrm{m/ps}$ for an initial diameter d_0.
For this speed of sound, the temperature of the plasma can be calculated as

$$k_B T = 2 m_{\mathrm{ion}} c_s^2, \tag{3.55}$$

with ion mass m_{ion}.

As this model only depends on the pulse intensity and has only been verified for ultra-short pulses, it has to be expected that deviations from this scaling occur when the pulse duration is increased substantially, as the contained and then also absorbed energy will increase.

The temperature calculated from the intensity according to Equations (3.54) and (3.55), together with the unchanged initial radius, provides the initial condition for the model described previously by Equation (3.52). After the initial heating and ionization of the target by the short pre-pulse, it is further heated by the ASE radiation and expands

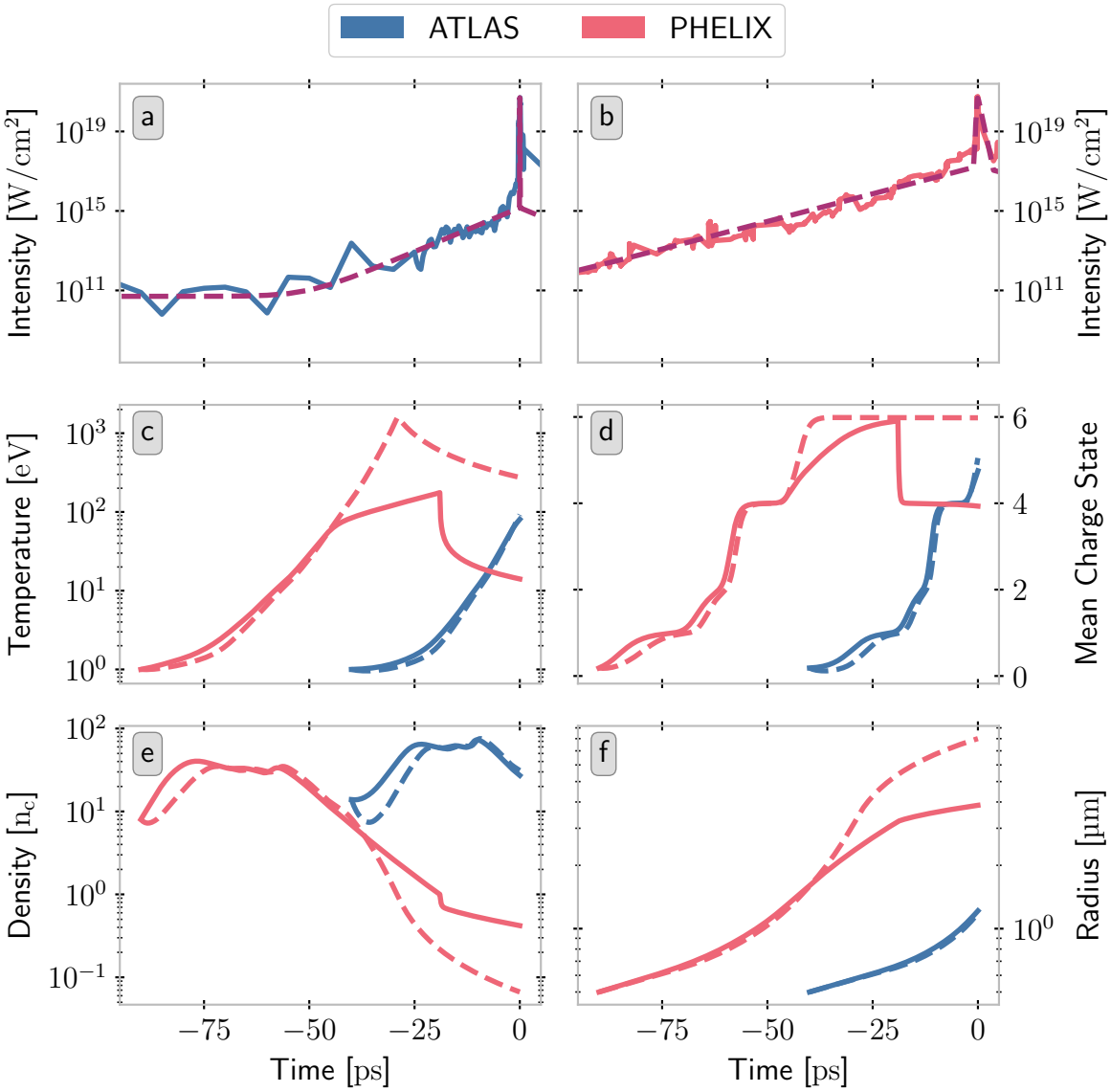

Figure 3.11.: **Model Results Neglecting Pre-Pulses**
Intensity of ATLAS (**a**) and PHELIX (**b**) over time as well as Temperature (**c**), ionization (**d**), free electron density (**e**), and radius (**f**) calculated by the model for these intensity curves starting when the intensity passes $10^{12}\,\mathrm{W/cm^2}$. The dashed in purple lines in **a** and **b** are the simplified intensity model used for the calculation, the solid lines are measured data. Dashed lines in **c-f** are calculated using the Bremsstrahlung model for the radiation loss, solid lines using the black body formula. Parameters relating to the ATLAS settings are shown in blue, those relating to PHELIX settings in red.

adiabatically while also loosing energy via radiation losses.

The key parameters of the model when including the pre-pulse of the respective laser system as initial condition are shown in Figure 3.12. Following the rapid heating by the pre-pulse the plasma cools over a few ps while expanding. After this first phase the expansion slows and during the rather low intensity ASE irradiation the temperature of the plasma stays nearly constant. The rising edge of the laser rapidly increases temperature and subsequently accelerates the expansion. The temperature increase stops for the PHELIX case at $\sim -50\,\mathrm{ps}$ when the plasma density falls below the critical density.

Compared to the model prediction without pre-pulse (Figure 3.11) the density drop below the critical density occurs 25 ps earlier. The final density at $t = 0$ does not change. This is due to the fact that the expansion slows again after the plasma becomes transparent and no more laser light is absorbed. Also the temperature of the plasma stays lower during the relevant interaction, as it becomes already transparent before the laser reaches the higher intensities.

In contrast, the final density for ATLAS parameters is reduced form $30\,\mathrm{n_c}$ to $3\,\mathrm{n_c}$ by a factor of ten compared to the model without pre-pulse. It also reaches a slightly higher temperature and ionization state. This is due to the larger cross section, which increases the total amount of energy absorbed by the plasma.

3.4. Summary

Combining the SSI model of Duchateau et al. from Section 3.1.2 with the simple numeric expansion model of Sections 3.2 and 3.3, a complete description of the plasma formation and expansion prior to the main pulse is possible.

The SSI model reveals that at an ASE intensity $< 10^{11}\,\mathrm{W/cm^2}$, the targets can be expected to remain in their solid state. Once the intensity rises, either during a short pre-pulse or at the beginning of the rising edge of the laser pulse, a plasma is ignited and begins to expand.

For the PHELIX parameters the expansion model agrees with the experimental observation of a plasma density below the critical density at the time of the main pulse. The fact that this density is not significantly affected by the introduction of a pre-pulse is in agreement with the observed relatively robust acceleration.

In the case of ATLAS, the density at $t = 0$ remains overcritical at $30\,\mathrm{n_c}$. Introduction of a pre-pulse reduces the density by a factor of 10, but it remains overcritical at $3\,\mathrm{n_c}$. This suggests that for an overcritical plasma the detailed contrast history is relevant and

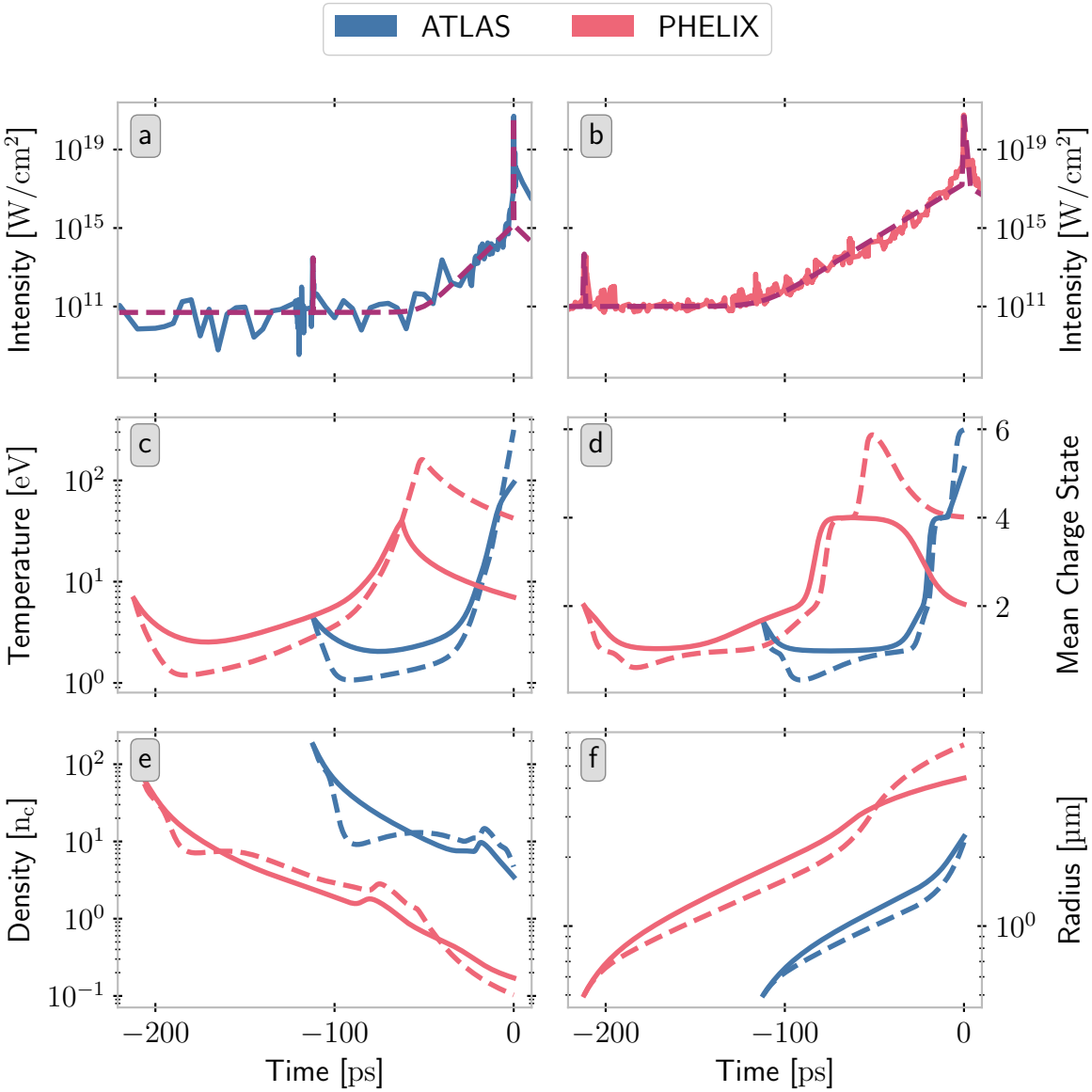

Figure 3.12.: **Model Results Including Pre-Pulses**
Intensity of ATLAS (**a**) and PHELIX (**b**) over time as well as Temperature (**c**), ionization (**d**), free electron density (**e**), and radius (**f**) calculated by the model for these intensity curves starting with the corresponding pre-pulse. The dashed in purple lines in **a** and **b** are the simplified intensity model used for the calculation, the solid lines are measured data. Dashed lines in **c-f** are calculated using the Bremsstrahlung model for the radiation loss, solid lines using the black body formula. Parameters relating to the ATLAS settings are shown in blue, those relating to PHELIX settings in red.

plasma conditions are sensitive to small variations. This agrees with the observation in the experiments at JETi, that the acceleration was very sensitive to the laser parameters.

4. Radiation Hydro Dynamic Simulation

4.1. Numerical Plasma Modeling in the RALEF Code

In order to simplify the description and reduce the computational cost, a plasma can be described as a fluid rather then a discrete particle ensemble (for a more thorough derivation see for example Ref. [136]). This is done by introducing the phase space distribution function $f(\mathbf{x}, \mathbf{v}, t)$. It describes the distribution of the particles in the phase space ($\mathbf{x}$, $\mathbf{v}$) as a function of time t. As particles are conserved, the typical continuity equation for fluids has to be obeyed

$$\frac{\partial f}{\partial t} + \frac{\partial}{\partial \mathbf{x}}(\dot{\mathbf{x}} f) + \frac{\partial}{\partial \mathbf{v}}(\dot{\mathbf{v}} f) = 0. \tag{4.1}$$

Combining this with the general equations of motion for this fluid in collective fields $\mathbf{E}$ and $\mathbf{B}$, yields the Vlasov equation, which is the typical starting point for numeric plasma descriptions:

$$\frac{\partial f}{\partial t} + \mathbf{v}\frac{\partial f}{\partial \mathbf{x}} + \frac{q}{m}\left(\mathbf{E} + \frac{\mathbf{v} \times \mathbf{B}}{c}\right)\frac{\partial f}{\partial \mathbf{v}} = 0. \tag{4.2}$$

With the addition of Maxwell's equations, this provides a complete description of a collisionless plasma. To make it easier to implement however, it is suitable to consider different moments of the Vlasov equation instead.

It can be noted, that the macroscopic plasma parameters density ρ, velocity $\mathbf{u}$ and pressure p themselves are the zeroth, first, and second moment of the phase space distribution averaged over the velocity.

The zeroth and first moments of the Vlasov equation then provide the corresponding conservation equations for mass and momentum, which can be augmented by energy conservation to form a usable set of fluid equations:

$$\frac{\partial \rho}{\partial t} + \nabla(\rho \mathbf{u}) = 0, \tag{4.3a}$$

$$\frac{\partial}{\partial t}(\rho \mathbf{u}) + \nabla(\rho \mathbf{u} \times \mathbf{u}) + \nabla p = 0, \tag{4.3b}$$

$$\frac{\partial}{\partial t}(\rho E) + \nabla\left[(\rho E + p)\mathbf{u}\right] = Q_T + Q_r + Q_{\text{dep}}. \tag{4.3c}$$

E is here the mass-specific total (internal + kinetic) energy and the right hand side of Equation (4.3c) describes different source terms. $Q_T = -\nabla(\mathbf{h}_T)$ is the energy change due to thermal conduction transported by the energy flux $\mathbf{h}_T$, $Q_r = -\nabla(\mathbf{h}_r)$ due to thermal radiation energy flux $\mathbf{h}_r$, and Q_{dep} the power deposited by external sources (e.g. laser irradiation).

These equations provide the core of the Radiative Arbitrary Lagrange-Eulerian Fluid dynamics (RALEF) code [142–144], which solves them (supplemented by equations for radiation transport) on a 2D coordinate system either in Cartesian or axi-symmetric cylindrical geometry. While the following equations are generally applicable, the concrete form and choice of equations and approximations is the same as used by RALEF.

The thermal energy flux is given by

$$\mathbf{h}_T = -\kappa \nabla T, \tag{4.4}$$

with the temperature of the plasma T and heat conduction coefficient κ, and the radiation energy flux by integration of the spectral intensity I_ν

$$\mathbf{h}_r = \int_0^\infty d\nu \int_{4\pi} d\mathbf{\Omega} I_\nu \mathbf{\Omega}. \tag{4.5}$$

In the quasi-static approximation the transfer equation for the spectral intensity is

$$\mathbf{\Omega} \nabla I_\nu = k_\nu (B_\nu - I_\nu), \tag{4.6}$$

where $\mathbf{\Omega}$ is the propagation direction, k_ν the spectral absorption coefficient (corrected for induced emission), and B_ν the radiation source function. A more detailed treatment of these parameters can be found for example in Ref. [140]. As described in Section 3.1.6, in the case of LTE, the source function is just the black-body spectral Planck intensity Equation (3.30).

The absorption of the laser is modeled on the one hand by the complex refractive index, which yields absorption from the Fresnel equations, and on the other hand by an

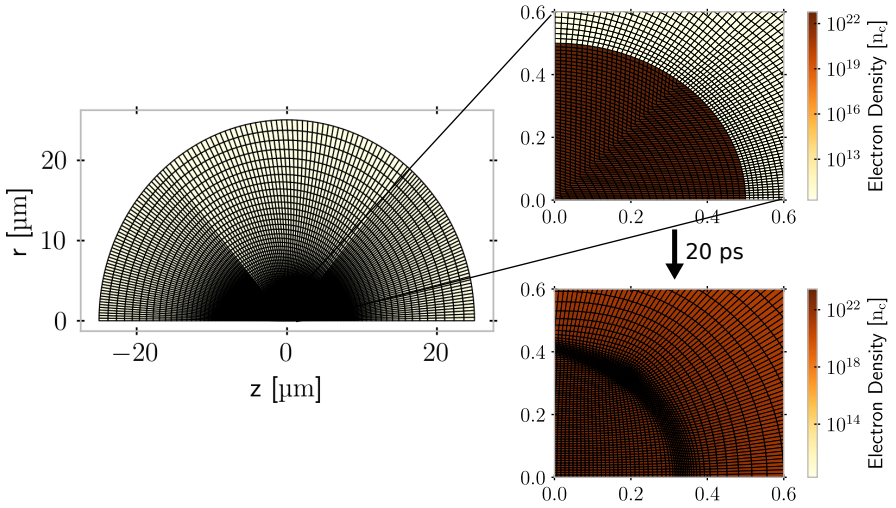

Figure 4.1.: **RALEF Simulation Setup**
Visualization of the setup of the RHD simulations performed by RALEF.

implementation of inverse Bremsstrahlung for collisional absorption.

The plasma in RALEF is described it as a single fluid. This means that some effects which occur at high temperatures and irradiation intensities can not be reproduced by it. As this is the same approach as used for the expansion model, the limit of $T \lessapprox 100\,\mathrm{eV}$, which was estimated in Section 3.2 in Figure 3.10, can be expected to apply here as well. Therefore, care has to be taken when interpreting results where the temperature rises above this value.

4.2. Simulation Setup

Simulations were performed for two different laser setups, representing the different conditions of the ATLAS and PHELIX system respectively.

The simulations utilize the radial symmetry of the problem to reduce the geometry to a cylindrical two-dimensional grid. The z axis is in this case along the laser propagation direction, and the r axis perpendicular to it. The adaptive grid has a semi circular shape with 25 µm radius with the target placed in the center. The laser enters the simulation volume from the right. Figure 4.1 shows the setup with a magnified view of the target in the top right. In the lower right is the same view shown after 20 ps simulation time to visualize the change in electron density and the way the grid changes to adapt to the plasma parameters.

As a computational simplification, the target is modeled as purely carbon ions at

	ATLAS-1	PHELIX-1	ATLAS-2	PHELIX-2
τ_{CC} [ps]	4.9	7.8	4.9	7.8
I_{CC} [W/cm^2]	$1.45 \cdot 10^{15}$	$1.79 \cdot 10^{17}$	$1.45 \cdot 10^{15}$	$1.79 \cdot 10^{17}$
t_{PP} [ps]	-	-	-112	-212
I_{PP} [W/cm^2]	-	-	$3 \cdot 10^{13}$	$5 \cdot 10^{13}$
I_{ASE} [W/cm^2]	-	-	$5 \cdot 10^{10}$	$1 \cdot 10^{11}$
d_{FWHM} [µm]	5	5	5	5
λ [nm]	800	1054	800	1054
T [ps]	[-40, 4]	[-90, 8]	[-113, -1]	[-213, -1]

Table 4.1.: **Simulation Parameters**
Parameters of the temporal contrast as defined for Equation (2.2), focal spot size, central wavelength, and total simulated time interval for the performed simulations.

$1\,\mathrm{g/cm^{-3}}$, instead of an equal mixture of carbon and hydrogen. This reduces the maximum number of electrons available in the system from $1.70 \cdot 10^{11}$ to $1.58 \cdot 10^{11}$ by 7 % and is therefore an insignificant approximation. Initially the plasma has a temperature of 124 meV with a corresponding average ionization degree of 1.2 and is therefore already opaque to the laser.

The temporal laser profile is again modeled by Equations (2.2) to (2.3d) as the sum of ASE, rising edge, and pre-pulse contributions. The main pulse is excluded, as only the dynamics leading up the it are of interest. Simulations are started once without considering the pre-pulses (ATLAS-1, PHELIX-1) at the point where the intensity passes $10^{12}\,\mathrm{W/cm^2}$, and once starting with the pre-pulse (ATLAS-2, PHELIX-2), also taking into account the ASE irradiation following this initial interaction. The parameters of the resulting four simulation cases are listed in Table 4.1, where the suffix -1 denotes simulations without pre-pulse and -2 with pre-pulse.

In the spatial dimension the laser has a Gaussian intensity profile $I(r) = I_0 \exp\{-\frac{4\ln(2)r^2}{d_{FWHM}}\}$ with a FWHM diameter of d_{FWHM}. It enters the simulation domain from the positive z side and travels in negative z direction.

4.3. Simulation Results

In Figure 4.2**a**, lineouts of the density along the laser axis are shown over the simulation time, visualizing the dynamics. The contours of three symbolic densities, $n_e = 1, 10, 200\,\mathrm{n_c}$, are shown as overlay. They represent the classical critical density, an approximation of the relativistic critical density $\gamma \mathrm{n_c}$ and the solid density respectively. In the left column, the simulations without pre-pulse (ATLAS-1 and PHELIX-1) are shown. They show a strong shock feature forming at the irradiated side, which travels into the otherwise undisturbed plasma bulk. As the ratio of ablation to radiation pressure scales as c/c_s [114, chapter 1.4], this is dominantly driven by ablation rather than radiation. Here c is the speed of light and c_s the speed of sound. A second shock forms later at the target rear side. This formation occurs once the plasma has heated sufficiently at the back side to create significant ablation. The ablation pressure then drives the shock into the target. As heating of the target back side can only occur by thermal transport through the target, it is cooler than the front and the shock amplitude and velocity are lower. At some point both shock waves collide inside the plasma. In the ATLAS-1 case this only occurs at the very end of the simulation, at which point the main pulse would arrive, interacting with plasma which has a peak density of more than solid density. On the other hand, for the PHELIX-1 case, the collision of the shocks happens already at $-40\,\mathrm{ps}$, with the plasma very quickly dispersing afterwards. The speed of the disintegration at this time can however not be relied upon, as the laser intensity and plasma temperature are no longer in the parameter regime, in which the simulations approach is applicable.

In the simulation cases starting with a short pre-pulse (ATLAS-2 and PHELIX-2), a somewhat different behavior can be observed. Directly after the interaction with the pre-pulse, also a shock forms at the target front and travels towards the center. However, as there is now little additional heating by the low intensity ASE radiation, this shock disperses more strongly than in the previous case and its peak density dropping over time. A noteworthy difference between the ATLAS-2 and PHELIX-2 cases is the resulting density shape. While it forms a shape similar to an additional flat-top with $n_e \approx 100\,\mathrm{n_c}$ on top of the initial density in the ATLAS-2 case, the PHELIX-2 case exhibits a saw-tooth like pattern in the logarithmic scale, i.e. an exponential rise. This dynamic in the PHELIX-2 case is accompanied by a stronger compression and deformation of the target, as seen by in the shape of the critical density contour. The different behavior could originate from the difference in duration or energy of the pre-pulse, or a combination of both.

In addition to this first shock, a second shock from the front forms when the laser intensity rises again, driven by the then increasing intensity and heating. This second shock behaves similarly to the one in the case without pre-pulse, as it is driven by the same intensity increase. Shortly after its onset, again a shock from the heated target back is launched. As the second front side shock is faster then the one launched by the pre-pulse, it catches up to it, creating a higher density spike. In the ATLAS-2 case this again happens just around $t = 0$, with all three shocks overlapping forming a density spike of $n_e \sim 10^3\,\mathrm{n_c}$. For PHELIX-2, the case is slightly different, as the first shock manages to traverse through the complete target in the first 100 ps after the pre-pulse. At the target rear reflects and begins to travel back toward the target. Just after turning around, it is caught up to by the second shock form the front side, overlapping at the edge of the initial target volume. In last tens of ps the target again disintegrates, when the simulation parameters leave the applicable regime.

In Figure 4.2**b** the same slices as in **a** are shown for the temperature of the plasma. Comparing them with the density nicely illustrates how the heat travels with the shock into the plasma, heating it up to the penetration depth of the shock. It also shows how increased temperature at the target rear side coincides with the shock from the back. Further, it makes it more clearly visible how the first shock wave in the cases with pre-pulse dissipates its energy. The shock front in fact cools down as it travels through the bulk and heats the bulk material. This effect is masked for the shocks driven by the rising edge of the laser pulse, as the increasing energy absorption from the exponentially rising intensity dominates the temperature evolution and provides the shock with sufficient energy.

While these shocks are important parts of the dynamic and on first glance dominate the behavior, their evolution occurs in a volume with far higher than critical density. This dynamic is therefore inaccessible to the laser pulse, and the interaction will be dominated by the behavior of the critical density iso-surface. Despite the compression inside the target, the critical surface expands and can reach up to a factor of two of the initial radius, in particular in the transverse dimension (cp. Figures B.1 and B.4). This increases the cross-section of the interaction by up to a factor of four.

A more detailed discussion of the simulation parameters can also be found in Appendix B. This includes further simulation parameters like heating rate, charge state, and fluid velocities as well as discussion of the behavior along the radial dimension. As these parameters behave as expected, with strong heating at the critical density surface and ionization following the temperature according to the Saha equation, they will not

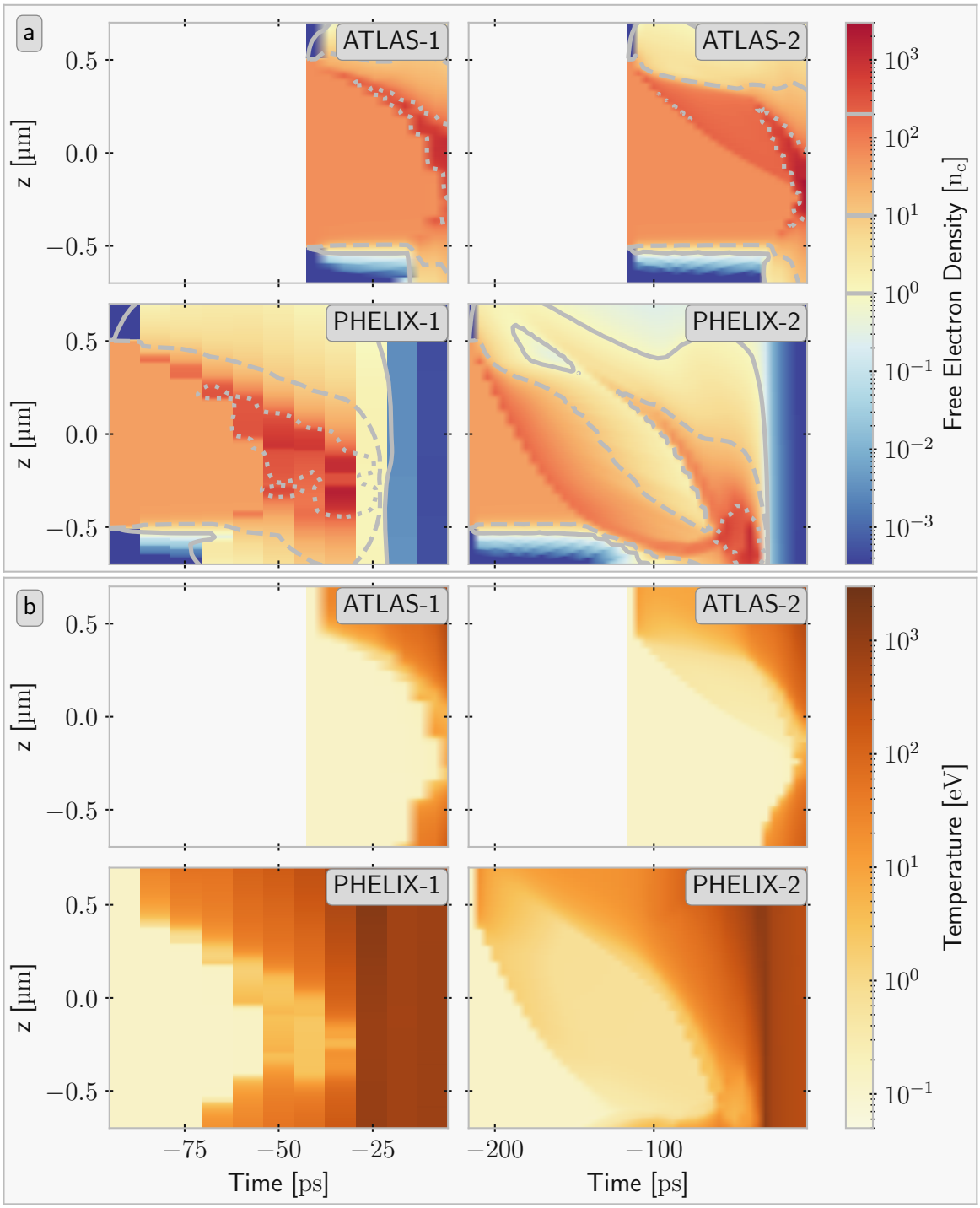

Figure 4.2.: **RHD Free Electron Density and Temperature Streaks**
Lineouts of the free electron density (**a**) and temperature (**b**) along the laser axis over time for the four simulation cases of Table 4.1. The solid, dashed, and dotted lines in **a** correspond to $1\,n_c$, $10\,n_c$, and $200\,n_c$ respectively. They mark the classical, estimated relativistic, and solid density.

be shown here.

In order to compare the simulations to the model developed in the previous chapter, it is necessary to calculate mean values of key plasma parameters. Mean Temperature T_{mean} and mean charge state Z_{mean} can be calculated as average over the fluid density distribution $n(\vec{r})$ in the simulation volume V with the integral over the fluid density $N = \int_V n(\vec{r})\mathrm{d}V$:

$$T_{\text{mean}} = \frac{1}{N}\int_V n(\vec{r})T(\vec{r})\mathrm{d}V \tag{4.7a}$$

$$Z_{\text{mean}} = \frac{1}{N}\int_V n(\vec{r})Z(\vec{r})\mathrm{d}V. \tag{4.7b}$$

Calculating a representative density is less straight forward. Averaging over the complete simulation volume would yield a constant value, as the significant changes are redistributing the fluid inside the simulation domain. On the other hand, just taking the maximum value would result in the shock dominating the evolution and completely disregarding the expansion of the critical surface. We choose to calculate the variance of the density distribution. The 2D radial variance σ_ρ in the z-r plane is defined as

$$\sigma_\rho = \frac{1}{N_e}\int_{-\infty}^{\infty}\int_{-\infty}^{\infty}\rho^2(r,z)n_e(r,z)drdz, \tag{4.8}$$

with $\rho^2 = (r-r_0)^2 + (z-z_0)^2$ being the distance from the center of the distribution (r_0, z_0) and $N_e = \int_V n_e(\vec{r})dV$ the total number of electrons. Equation (4.8) is evaluated in cylindrical coordinates for a flat top distribution with radius ρ_0 as $\sigma_\rho = \frac{\rho_0}{\sqrt{2}}$. Therefore, the equivalent radius of the distribution with σ_ρ is defined as $\rho_{\text{equiv}} \coloneqq \sqrt{2}\sigma_\rho$. The equivalent free electron density is then calculated by distributing all free electrons N_{fe} in a flat-top distribution with this radius

$$n_{e,\text{equiv}} = \frac{3N_{\text{fe}}}{4\pi\rho_{\text{equiv}}^3}. \tag{4.9}$$

Mean temperature and equivalent free electron density for all simulation cases are shown in Figure 4.3. **a** shows the intensity on the target over time, where the dashed lines mark the beginning of the simulations without pre-pulses (ATLAS-1, PHELIX-1). The equivalent free electron density is shown in **b** and the mean temperature in **c**.

In the PHELIX case without pre-pulse the equivalent free electron density drops over $\sim 70\,\text{ps}$ from the initial value of $35\,\text{n}_\text{c}$ to $n_{e,\text{equiv}} \leq 1\,\text{n}_\text{c}$. This point where the plasma becomes sub-critical is 30 ps before arrival of the main pulse. In the same time the mean

temperature rises to $T_{\mathrm{mean}} = 1\,\mathrm{keV}$. After the equivalent free electron density is below the critical density, the temperature drops. This is consistent with a reduced absorption in the sub-critical plasma.

When including the pre-pulse of PHELIX, the equivalent free electron density drops over the first 100 ps to $n_{e,\mathrm{equiv}} \approx 3\,\mathrm{n_c}$ where it stagnates. This is the point where the initial shock wave reflects from the target rear side and additional ablation begins at target front and rear, as shown in Figure 4.2. Around $t = -50\,\mathrm{ps}$ the density drops again, this time below the critical density. The mean temperature is initially raised to $T_{\mathrm{mean}} \approx 2\,\mathrm{eV}$ by the pre-pulse and then stagnates there during the ASE irradiation. Once the rising edge of the intensity begins, the temperature increases exponentially to $T_{\mathrm{mean}} \approx 1\,\mathrm{keV}$ before the target becomes sub-critical. At this point it again drops, this time to $T_{\mathrm{mean}} \approx 300\,\mathrm{eV}$.

In the case of ATLAS without pre-pulse the equivalent electron density also directly begins to drop. Over the 40 ps of the rising edge it falls to $n_{e,\mathrm{equiv}} \approx 20\,\mathrm{n_c}$ and the plasma remains overcritical until the arrival of the main pulse at $t = 0$. The temperature increases in this time exponentially up to $T_{\mathrm{mean}} \approx 100\,\mathrm{eV}$.

Taking into account the pre-pulse, the equivalent electron density remains initially unchanged for 70 ps. The pre-pulse raises the mean temperature to $T_{\mathrm{mean}} \approx 0.6\,\mathrm{eV}$, where it stagnates until the beginning of the rising edge of the laser intensity. In the rising edge the mean temperature rises exponentially up to $T_{\mathrm{mean}} \approx 200\,\mathrm{eV}$ while the equivalent free electron density drops to $n_{e,\mathrm{equiv}} \approx 11\,\mathrm{n_c}$.

Comparing the two cases without pre-pulse, the effect of the longer and more intense rising edge of PHELIX is apparent, resulting in a sub-critical density plasma for PHELIX and a still significantly overcritical plasma for ATLAS. Also the effect of the pre-pulse strongly differs between both laser systems. While it launches a slowly traveling shock wave which has no significant impact on the equivalent free electron density in the ATLAS case, it leads to an exponential drop in density in the PHELIX case. This shows that not only the pre-pulse intensity is relevant for the dynamics, but also the total energy content of the pre-pulse, which is ~ 10 larger in at PHELIX than ATLAS. Another observation is, that the ASE irradiation after the pre-pulse, while tens to hundreds of ps long, has little to no effect on the plasma. During this phase, the mean temperature stagnates in both cases and the dynamics launched by the short pre-pulse play out until the equivalent free electron density stagnates as well.

Remarkably, in both laser systems the pre-pulse has only a small impact on the final density distributions. At PHELIX, it changes the time when the plasma becomes

sub-critical by $\sim 20\,\mathrm{ps}$, but as the absorption is significantly reduced after this point and the plasma cools, a similar final distribution can be expected. However, as the laser parameters at the end of the simulation reached the regime where the simulation approach is no longer applicable, this can not be directly confirmed by the simulation. In the ATLAS case, the resulting final equivalent free electron density is only reduced by a factor of ~ 2, remaining in both cases well above the critical density.

To further investigate the heating dynamics, the dependence of the mean temperature on the incident intensity is shown in Figure 4.3**d**. The behavior is very similar for all simulation cases, following approximately a power law. For comparison, an exemplary scaling proportional to the square root of the intensity is shown as gray dashed line. The different offsets of the simulations can likely be explained by the changing cross-section, when the plasma expands transversely, changing the total absorption.

As the absorption coefficient is a free parameter in the expansion model, it is of interest to determine the amount of energy that is absorbed by the plasma in the simulation. This is done by integrating over the heating rate q, which is directly accessible from the simulation code, to yield the total absorbed power $P_{\mathrm{abs}} = \int_V q(\vec{r})\mathrm{d}V$ at each simulation time step. The absorption coefficient $\eta = \frac{P_{\mathrm{abs}}}{P_{\mathrm{inc}}}$ is then calculated by dividing the absorbed power by the total incident power $P_{\mathrm{inc}} = 2\pi \int_0^\infty I(r)\mathrm{d}r$ from the laser pulse definition. Results of this calculation for each simulation time step are shown in Figure 4.4.

As this calculation is done by integration over the complete laser cross-section, the total laser power used for the normalization also includes all light that passes the target at the side without actually interacting with it. The effective area of the laser spot is $28\,\mu\mathrm{m}^2$, while the area of the initial target is $0.79\,\mu\mathrm{m}^2$. Therefore, 97 % of the laser energy passes the target without interaction. This changes as the target expands, but the size of the target, as defined by the critical density, stagnates in the transversal dimension at $r_{\mathrm{targ}} \approx 1\,\mu\mathrm{m}$ (cp. Figure B.1). At this expansion, the area of the laser focus is still nine times larger than the target cross-section.

In the simulations with pre-pulse the absorption coefficient is nearly constant at $\eta \approx 5\,\% - 8\,\%$ during the duration of the ASE. As soon as the rise in intensity begins, the absorption coefficient drops to $\eta \approx 1\,\%$. In the simulations without pre-pulse, which only model this rising edge, the absorption is around $\eta \approx 0.5\,\%$.

Correcting these values for the interaction cross-section, the effective absorption of the plasma η_{eff} can be estimated. During the ASE irradiation this is of the order of $\eta_{\mathrm{eff}} \gtrapprox 50\,\%$. In the rising edge of the pulse this drops to $\eta_{\mathrm{eff}} \approx 10\,\%$.

This supports the assumption of a constant absorption of 10 %, which was made in the

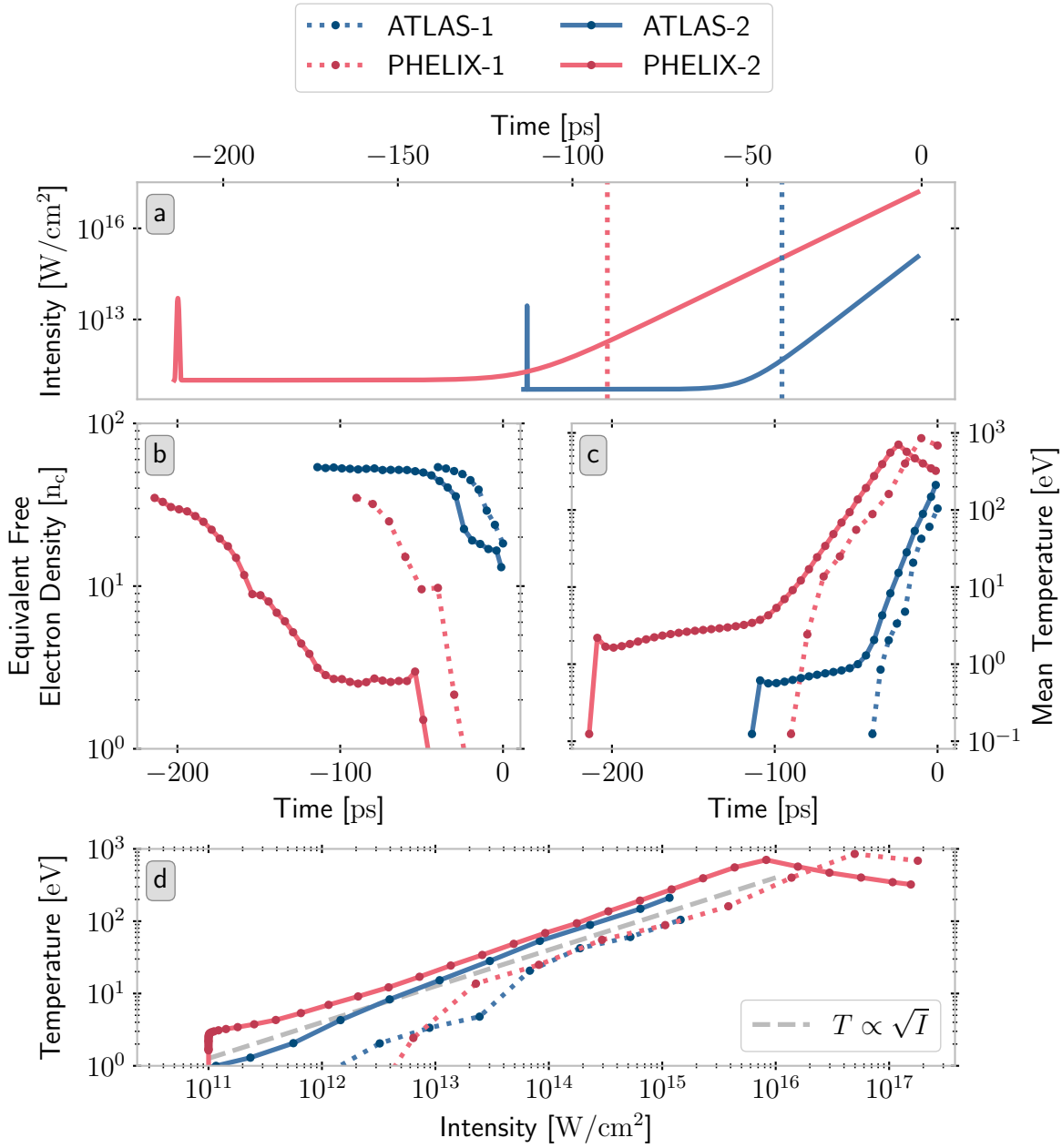

Figure 4.3.: **Results of the RALEF Simulations**
Input intensity profile (**a**), equivalent free electron density (**b**), and plasma temperature (**c**) over time as well as plasma temperature over intensity (**d**). Blue corresponds to simulations with ATLAS parameters, red to PHELIX parameters. Dotted lines are without pre-pulse and solid lines including the pre-pulse. The dotted lines in **a** indicate the point, at which the simulations without pre-pulse start, the dashed gray line in **d** indicates a scaling with the square root of the intensity.

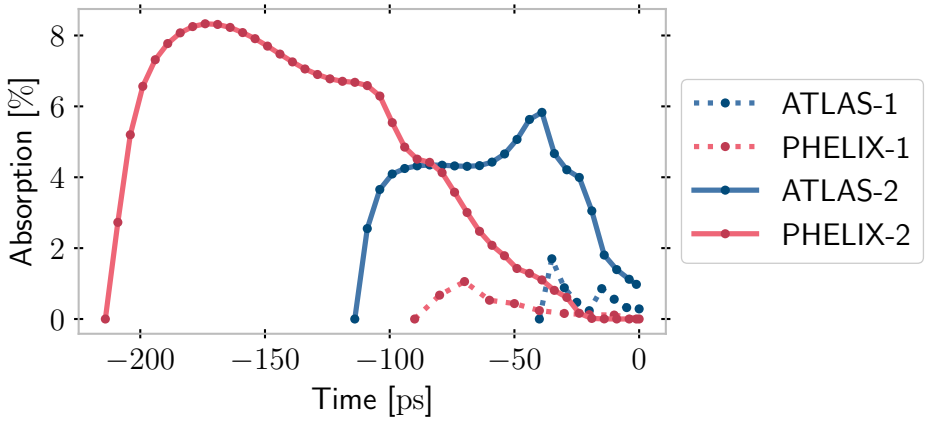

Figure 4.4.: **Absorption Coefficient**
Absorption coefficient over time extracted from the RALEF simulations for the four simulation cases.

expansion model. While the absorption during the ASE irradiation is larger, the intensity and energy content during this phase is so much lower than in the rising edge, that the error is assumed to be small. Another observation is that the absorption drops abruptly towards zero once the target becomes transparent, thereby supporting the simplifying assumption of zero absorption in the transparent plasma in the model.

4.4. Simulation Summary

The RHD simulations reveal that the plasma develops complex shock dynamics, driven by short pre-pulses as well as the rising edge of the laser pulse. Despite this, it is possible to define an equivalent free electron density to allow for easier comparison between the different simulation cases and the expansion model.

As expected, the simulations show a clear difference in the dynamics between the ATLAS and PHELIX cases. This is caused by higher energy content of the PHELIX pre-pulse and rising edge. As a result of this, the plasma in the PHELIX case becomes sub-critical tens of ps before the main pulse, which is in agreement with the experimental observation of Hilz et al. [74]. In the ATLAS case the plasma remains overcritical with an equivalent free electron density $n_{e,\mathrm{equiv}} > 10\,\mathrm{n_c}$.

For both laser systems the simulations reveal only minor changes of the final densities and temperatures, when including the pre-pulse and ASE irradiation. The mean temperature follows the irradiating intensity with an approximate power law relation for all simulation cases.

5. Discussion

The experiments performed with levitating micro-targets at CALA yielded unexpected yet interesting results. The energies and particle numbers of the accelerated protons fell short from values expected from scaling the experimental results previously obtained at JETi. The interpretation of the transmitted light gives important insight into the plasma conditions at the time of the interaction. In particular, this diagnostic allows to reconstruct the position of the target with respect to the laser focus. This reveals that no ions were accelerated with target and laser perfectly overlapping and the actual intensity of the laser on target was reduced by more than a factor of five. For this intensity in the range of $10^{19}\,\mathrm{W/cm^2}$-$10^{20}\,\mathrm{W/cm^2}$, the observed proton energies around 8 MeV cut-off are in fact expected from targets which are not expanded to the ideal conditions.

This observation can indicate either the presence of yet unknown offsets between the observed position of the attenuated laser pulse and the actual position of the full power focus or an insufficiently good temporal pulse contrast. As it was already tried to compensate for all known offsets in the focus position, the point of plasma ignition and the subsequent expansion were investigated.

In order to estimate the point where the plasma is ignited, the Solid-State Ionization model of Duchateau et al. is adapted to the target and laser parameters of the relevant experiments at ATLAS and PHELIX. The results of this model indicate that ASE intensity in both cases is insufficient to ignite the plasma due to multi-photon ionization. This transition only occurs either during a short pre-pulse, which is present in both laser systems, or at the beginning of the rising edge of the main pulse. Therefore, two possible initial conditions for the expansion of the plasma exist. Either it is ignited during the interaction with the short pre-pulse, and then subsequently heated by ASE and the exponentially rising edge, or it is only ionized sufficiently at the start of the rising edge, when the intensity increases to more than $5 \cdot 10^{11}\,\mathrm{W/cm^2}$.

The plasma expansion is estimated from an analytical model and benchmarked against RHD simulations to investigate the dynamics following the ionization.

A first comparison can be made for the case of a single short pulse of moderate intensity, such as a pre-pulse, without any other irradiation. For this the expansion model is compared to RHD simulations which were performed for the parameters of the ZEUS

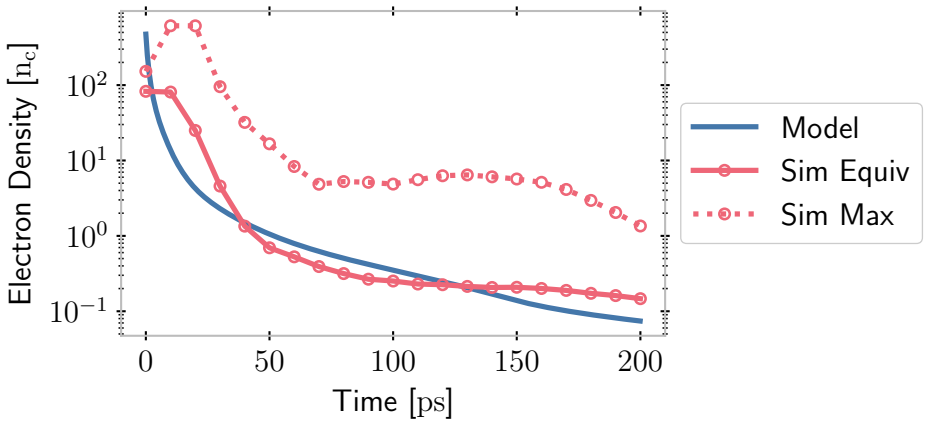

Figure 5.1.: **Plasma Expansion after a Pre-Pulse**
Electron density over time for the model (blue) and RHD simulation (red) after interaction with a single pulse of $1 \cdot 10^{16}\,\mathrm{W/cm^2}$ intensity. The red solid line is the equivalent free electron density of the simulation and the dotted line the maximum density.

laser. The pulse of ZEUS emulates a pre-pulse at a larger system, with a peak intensity of $10^{16}\,\mathrm{W/cm^2}$ and 60 fs-65 fs FWHM pulse duration at 790 nm central wavelength. The target is again a solid density ($\rho = 1\,\mathrm{g/cm^3}$) sphere of CH in the model and pure carbon in the simulation. In the RHD simulation the interaction of the target with the pulse and the subsequent expansion over 200 ps is modeled. The expansion model starts with the initial condition given by a $1 \cdot 10^{16}\,\mathrm{W/cm^2}$ laser pulse at $t = 0$ and then evolves without any further laser irradiation. For the radiation loss the bremsstrahlung model is used. In Figure 5.1 the prediction of the expansion model (blue line) is shown as well as the equivalent (solid red line) and maximum (dotted red line) free electron density from the simulation. The expansion model agrees well with the equivalent free electron density in the simulation, while the maximum free electron density of the simulation remains at larger values as expected. For later times the density in the model decreases faster than in the simulation. This indicates that the energy loss in the model is slightly underestimated and it can be expected that the model consistently underestimates the density.

This benchmarks shows that the approximation of the short pre-pulse effect in the expansion model provides a reasonable estimate, keeping in mind its limitations.

Results of benchmark using the ATLAS and PHELIX cases are shown in Figure 5.2, where **a** and **c** show the cases without pre-pulse and **b** and **d** the cases with pre-pulse. A first observation is the remarkably good agreement between the relatively simple expansion

model and the simulations. Larger deviations mainly occur at the very beginning of the evolution and originate from the artificial initial conditions of the model as well as the simulation. However, mean temperature as well as equivalent free electron density evolution follow similar trends. For the PHELIX case the point where the equivalent free electron density falls below the critical density is slightly shifted between model and simulation, likely because the expansion model assumption of a flat-top distribution is too simple. Any realistic density will have some peak that remains above the critical density for a longer time. Despite this, the mean temperature and equivalent free electron density predictions match well up to the point where the simulated intensity passes $10^{16}\,\mathrm{W/cm^2}$ and the assumptions for the simulation and expansion model are no longer satisfied.

Significant differences between expansion model and simulation are observed in the equivalent free electron density in the ATLAS case with pre-pulse (blue lines in **d**). Here the equivalent free electron density in the simulation remains constant at nearly solid density, while it initially drops to $n_{e,\mathrm{equiv}} \approx 10\,\mathrm{n_c}$ in the model. This discrepancy can be explained by the modeling of the interaction with the pre-pulse. While the simulation models this explicitly, taking into account localized absorption and subsequent dynamics, the numeric model only incorporates an averaged approach. In the model the energy deposited by the laser during the pre-pulse is evenly distributed into the complete target, heating it uniformly and then modeling the expansion over the ps range. This initial heat is converted into the adiabatic expansion and part of it is radiated, resulting in the initial sharp drop in density and temperature, before reaching a plateau. In the simulation on the other hand, the energy in mainly deposited in the traveling shock wave, while the rest of the target remains cold. Therefore, no significant expansion is triggered until the shock has passed through the target and dissipated its energy into the bulk plasma.

The good agreement between the numerical model and the simulations stimulates confidence in their predictions. They show, that neither just the rising edge of the pulse, nor the combination of the pre-pulse together with ASE and rising edge is sufficient to reduce the plasma density below the critical density with ATLAS parameters. In the case without pre-pulse the resulting final density of $30\,\mathrm{n_c}$ at $t = 0$ should be more than sufficient to support efficient acceleration, and also when taking into account the pre-pulse, the density remains at $\sim 10\,\mathrm{n_c}$ with an expected peak at higher values.

Together with the fact that there are a number of different error sources regarding the laser focus optimization, like aberrations and drifts, this suggests that the target position distribution observed in the ATLAS experiments is caused by so far undetected systematic offsets, rather then an insufficient laser contrast.

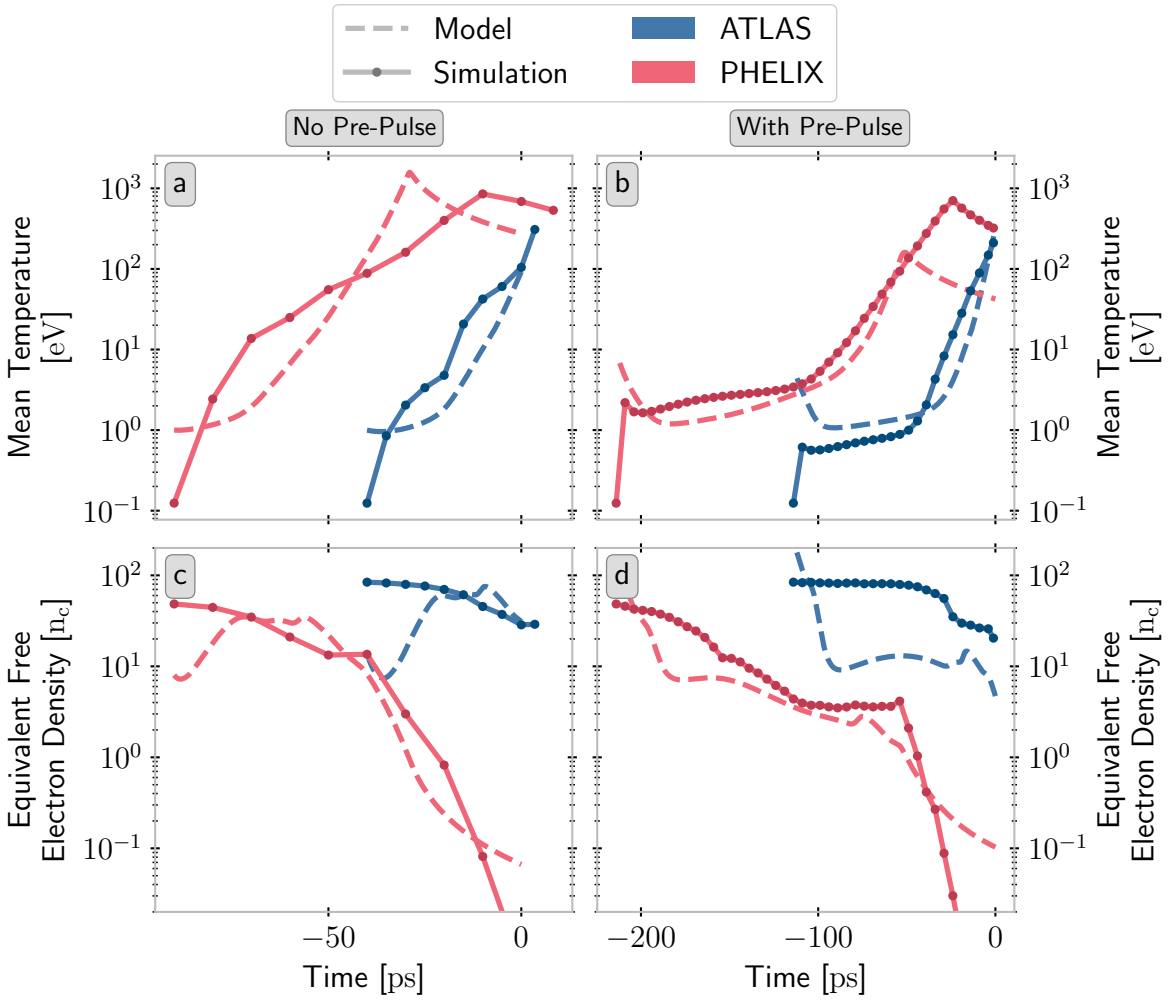

Figure 5.2.: **Comparison of the Numerical Model and RHD Simulations** Mean temperature (**a, b**) and equivalent free electron density (**c, d**) of the expansion model of Chapter 3 plotted over the corresponding quantities extracted from the RALEF simulations (Chapter 4). The left column (**a, c**) shows the cases without pre-pulse (ATLAS-1, PHELIX-1), the right column (**b, d**) with pre-pulse (ATLAS-2, PHELIX-2). Dashed lines are the model predictions and solid lines the simulation.

6. Conclusion and Outlook

In the core of this a simplified model for material breakdown and subsequent plasma expansion has been developed in order to investigate the impact of a real temporal laser contrast on ion acceleration from microscopic isolated polystyrene targets. The ionization model suggests a breakdown intensity for ns long laser pulses of $5 \cdot 10^{11}\,\mathrm{W/cm^2}$ and thereby gives a limit for the ASE contrast that is required to avoid target breakdown nanoseconds before the main pulse. This threshold likely also holds for other target geometries such as foils.

With the expansion model, which can incorporate short pre-pulses as well as the exponential rising edge of the laser, it is possible to calculate average density and temperature of the target shortly before it interacts with the main pulse. The model compares well with RHD simulations, despite not being able to capture the dynamics of the shock wave, which forms at the irradiated side of the target due to ablation and radiation pressure.

Applying the model to the experimental conditions at the LION target area in CALA reveals, that the temporal contrast of the ATLAS-3000 system is in fact sufficient and by virtue of coincidence close to ideal for proton acceleration, because the predicted target density at interaction with the pulse peak is close to the relativistic critical density. It has therefore to be concluded that the observed systematic displacement of the target relative to the laser focus is real and does not resemble the premature disintegration of the target in the highest intensity regime. The reason for this displacement is so far unknown but there are meanwhile multiple effects identified, which result in a displacement between full power and attenuated focus position. For example, it was discovered that the optional filters of the laser attenuator introduce significant aberrations, on the same order of magnitude as the attenuator itself [108], which were not compensated in the experiments presented here.

The fact that model and simulation agree as well as they do suggests that the model can be used to draw conclusions for future experiments with isolated targets. In particular, it allows estimating whether a given temporal laser contrast will result in favorable conditions for ion acceleration or if additional measures, such as plasma mirrors, are necessary.

As an example, the same configuration which was used in the JETi experiments can be evaluated without the use of a plasma mirror and additional pre-pulse. In this case the energy that can be delivered onto the target can be increased by a factor of two [71], resulting in a peak intensity of $5 \cdot 10^{20}\,\mathrm{W/cm^2}$. The ASE level of JETi is lower than that of ATLAS even without plasma mirror and the rising edge is also steeper. This means that the ASE level is also insufficient to ignite the plasma and the expansion due to the rising edge will be less. However, the JETi has a pre-pulse ∼465 ps prior to the main pulse with an intensity of $3 \cdot 10^{13}\,\mathrm{W/cm^2}$ (see Figure 6.1**a**). Without plasma mirror, this pre-pulse will be sufficient to ignite the plasma and the expansion will start much sooner than in the case of ATLAS.

In Figure 6.1**b, c** the results of the model for the temperature and density are shown. Just after the pre-pulse the plasma is relatively warm and quickly cools down to around 1 eV. However, during the subsequent interaction with the ASE it heats up again over a time of 200 ps to a temperature of 10 eV. While this happens, the target expands continuously and the density drops at a constant rate, as the temperature is too low for significant additional ionization. Already more than 200 ps before arrival of the main pulse the density drops below the critical density. This means that while the ASE and rising edge intensities at JETi are sufficient, with the existing pre-pulse it is unlikely that experiments could reach the optimum conditions for ion acceleration.

To evaluate the significance of the pre-pulse, the model is also evaluated under the assumption that no relevant pre-pulses exist. In this case the target only breaks down in the last 20 ps before the main pulse (Figure 6.1**d**). Due to the low intensity in the rising edge, the temperature (**e**) only significantly increases in the last few ps prior to the main pulse. In the density this is seen as an increase due to the rising degree of ionization as the temperature increases towards 10 eV. Therefore, without additional pre-pulse above an intensity of $\sim 10^{13}\,\mathrm{W/cm^2}$, the JETi contrast would only lead to small expansion and a high density plasma. This would likely be too dense for the optimum ion acceleration and the contrast would therefore have to be worsened deliberately to reach optimum conditions. As it is effectively impossible to vary the parameters of the rising edge smoothly and controlled, an additional artificial pre-pulse as already used in Ref. [71] would be the best approach to realize this.

Beside the application to single laser systems, the model can be used to forecast general effects of the laser contrast. In Figure 6.2, the electron density at the time of the main pulse is shown for either only a rising edge in the contrast (**a**) or only a pre-pulse (**b**). Each case is parametrized by two variables, one for the corresponding temporal constant

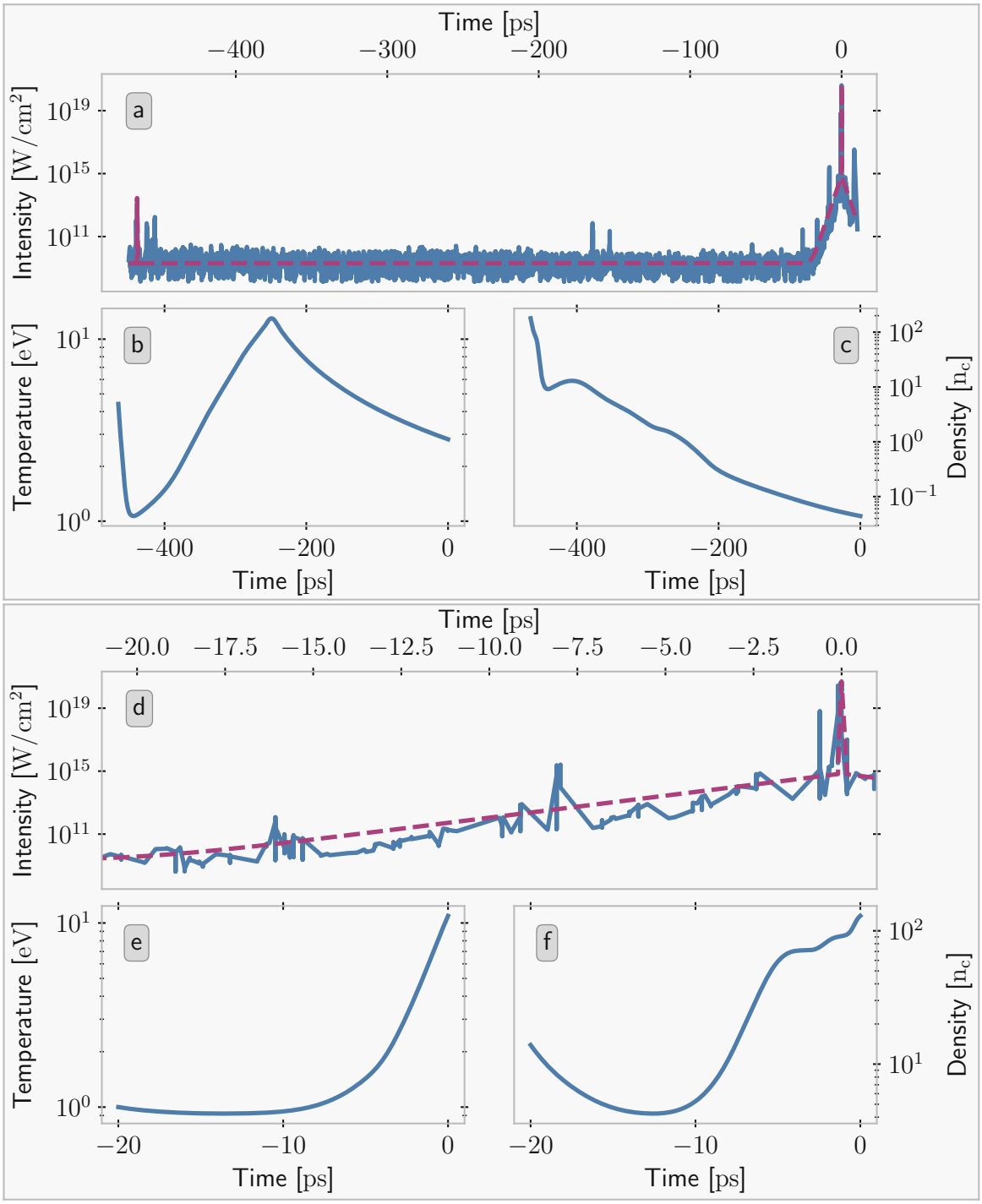

Figure 6.1.: **Expansion Model Applied to JETi Parameters**
Results of the numeric model when applied to the complete JETi contrast (**a-c**) and without short pre-pulses (**d-f**).**a** and **d** show the temporal contrast measurement obtained by a TOAC in blue and intensity input for the model in purple. In **b** and **e** the temperature evolution calculated by the model is shown and in **c** and **f** the density.

(τ and t_{pp} respectively) and one for the intensity (I_0 and I_{pp}). The positions of the three laser systems discussed previously (ATLAS, PHELIX, and JETi) are shown in both plots. In **b**, the JETi point is not shown, as it lies too far out of the otherwise relevant time scale. In addition, the Texas PetaWatt (TPW) laser system is shown as well, as it was also used for experiments with levitating micro-spheres [73]. The Dresden Laser Acceleration Source (DRACO) [4, 61] system is shown as well, as it has been used for experiments with mass limited jet targets in the past [145] and could be an interesting candidate for future experiments. As it does not have pre-pulses above $10^{13}\,\mathrm{W/cm^2}$, it is only shown in **a**. For all systems, it is assumed that no plasma mirror is used and the focus geometry is identical to the reported experiments.

As expected, there exists a clear trade-off for purely rising edge contrast between the highest point of the rising edge and the time constant of the exponential rise. For very steeply rising edges, the density is still highly over-critical up to relativistic intensities, at which point the acceleration process begins. On the other hand, moderate intensities over a longer time give a larger area where $n_e \approx \gamma \mathrm{n_c}$ and the acceleration is expected to be optimal. However, the area of optimum conditions is very small and the gradient from very high density to below critical density is steep. This makes tuning a systems parameters to the optimum conditions difficult. Despite this, TPW as well as ATLAS are already in or near the optimum conditions.

In the case of a good contrast with a single short pre-pulse the transition from a low density to a high density plasma is much smoother and the area where the plasma is in the range of $1\,\mathrm{n_c}$-$10\,\mathrm{n_c}$ is very large. This makes short pre-pulses an ideal tool to tailor the contrast of an otherwise clean system. At $-112\,\mathrm{ps}$ and $3 \cdot 10^{13}\,\mathrm{W/cm^2}$ the pre-pulse at ATLAS would also be close to ideal conditions, while the pre-pulse at PHELIX, despite lower intensity, results already in a classical critical density plasma.

As so far the experimental data to verify the model is sparse, a next step would be to perform experiments aimed at investigating the plasma dynamics shortly before the main pulse arrival. For this a pump-probe setup with a holographic probing approach similar to the one implemented in the ZEUS experiments would be well suited [75]. As pump laser a few hundred TW to PW system without plasma mirror and ideally a variable temporal contrast would be ideal. While there are some difficulties associated with probing a plasma irradiated at more than $10^{20}\,\mathrm{W/cm^2}$, in particular the very strong signal emitted from the interaction with the main pulse, it has already been shown that it is possible to perform such experiments e.g. in Ref. [145].

Pending experimental verification, there are some aspects of the model that could still

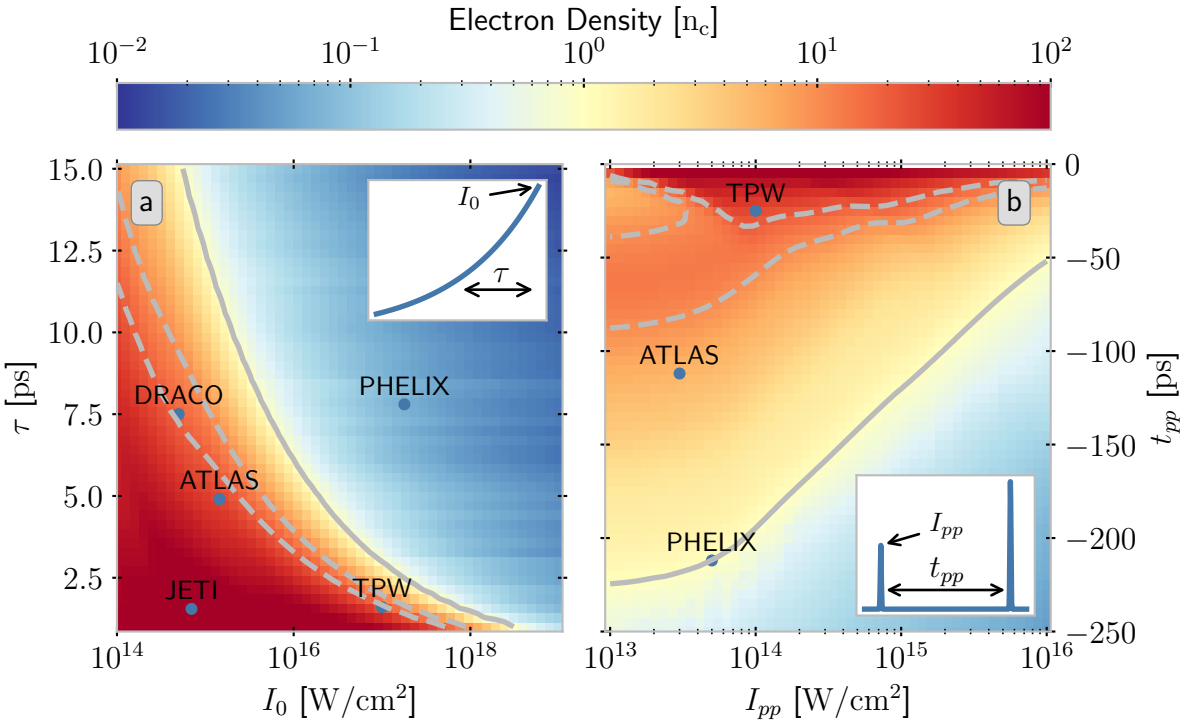

Figure 6.2.: **Contrast Limits**
Final density of the numerical model assuming only rising edge (**a**) or only pre-pulse (**b**) contributions for the relevant parameter spaces. The insets visualize the meaning of the parameters for the pulse shape. The solid line marks the critical density and the dashed lines with $10\,n_c$ and $20\,n_c$ the expected area of γn_c. The location of selected laser systems (ATLAS, TPW [73], JETI [71], PHELIX [74], DRACO [61]) in the parameter space is marked as circles.

be refined in order to improve the expected accuracy. First, the determination of the breakdown point could be improved by implementing the improvements to the SSI model which were already suggested by Duchateau in Ref. [133]. Further, the description of the radiation field inside the target and the loss due to radiation could be improved by taking into account the local opacity and using it to better calculate the radiative effects. However, as this requires more detailed knowledge of the target composition and the possible atomic transitions, it would make the model harder to adapt to different target materials. Last, the density distribution could be adapted from a simple flat-top to a more realistic model, which might even include the shock to some extent. However, this would complicate modeling of laser absorption and the radiation inside the plasma, increasing the computational effort and making interpretation of the model somewhat less intuitive.

So, while some improvements are still possible, the combination of the numeric model and RHD simulations provides a coherent picture of the interaction of an isolated plasma with a short ultra-high power laser pulse from the initial ionization up to the point of relativistic intensities. The predictions are in reasonable agreement with experimental observations and allow for extrapolation to other laser parameters. Thereby this work provides a solid basis for the design of future experiments with isolated micro targets and optimization of laser systems for ion acceleration.

Finally, we should note that experiments with isolated targets smaller than the laser focus reveal insights that can hardly be gained from experiments with foil targets. The possibility to probe the interaction without need for additional and typically complicated tools, such as off-harmonic synchronized probes [145], makes these targets an interesting modality to investigate the position and quality of the high power focus, probe the impact of the temporal laser contrast, and benchmark simulations.

Publications and Conference Contributions

Journal articles

- Gebhard, J., Doyle, L., **Balling, F.,** Kalis, J., Speicher, M., Schreiber, J., Sävert, A., Schäfer, G., Khademi, P., Liu, B., Zepf, M., Two-stage laser proton acceleration from levitating near-critical micro-plasmas. *In Preparation* (2024)

- He, L. R., Bachhammer, M, Liese, J, Schmidt, A, Praßelsperger, A, Hofrichter, I, Vaidyanathan, V, Doyle, L, **Balling, F,** Gerlach, S, Karsch, S, Schreiber, J, Variability Assessment of a Laser-Driven Water-Leaf Proton Source with Energies Beyond 20 MeV. en. *Submitted to Physical Review X* (2024)

- Rösch, T. F., Afshari, M., **Balling, F.,** Doyle, L., Gerlach, S., Hartmann, J., Prasselsperger, A., Morris, S., Schreiber, J., Transverse emittance growth of proton sources from laser-irradiated sub-µm-thin planar targets. *Physical Review E* **109.** Publisher: American Physical Society, 025201. doi:10.1103/PhysRevE.109.025201 (Feb. 2024)

- Gerlach, S., **Balling, F.,** Schmidt, A. K., Brack, F. E., Kroll, F., Metzkes-Ng, J., Reimold, M., Schramm, U., Speicher, M., Zeil, K., Parodi, K., Schreiber, J., Three-dimensional acoustic monitoring of laser-accelerated protons in the focus of a pulsed-power solenoid lens. en. *High Power Laser Science and Engineering* **11,** e38. ISSN: 2095-4719, 2052-3289. doi:10.1017/hpl.2023.16 (2023)

- Weiße, N., Doyle, L., Gebhard, J., **Balling, F.,** Schweiger, F., Haberstroh, F., Geulig, L. D., Lin, J., Irshad, F., Esslinger, J., Gerlach, S., Gilljohann, M., Vaidyanathan, V., Siebert, D., Münzer, A., Schilling, G., Schreiber, J., Thirolf, P. G., Karsch, S., Döpp, A., Tango Controls and data pipeline for petawatt laser experiments. en. *High Power Laser Science and Engineering* **11,** e44. ISSN: 2095-4719, 2052-3289. doi:10.1017/hpl.2023.17 (2023)

- Praßelsperger, A., **Balling, F.,** Wieser, H.-P., Parodi, K., Schreiber, J., Ion-bunch energy acoustic tracing by modulation of the depth-dose curve. en. *High Power Laser Science and Engineering* **11,** e42. ISSN: 2095-4719, 2052-3289. doi:10.1017/hpl.2023.18 (2023)

Conference proceedings

- **Balling, F.,** Gerlach, S., Schmidt, A.-K., Bagnoud, V., Hornung, J., Zielbauer, B., Parodi, K., Schreiber, J., *First tests of the I-BEAT detector as primary monitor for target normal sheath accelerated protons* in *Laser Acceleration of Electrons, Protons, and Ions VI* (eds Bulanov, S. S., Schroeder, C. B. & Schreiber, J.) (SPIE, Online Only, Czech Republic, Apr. 2021), 27. ISBN: 978-1-5106-4392-5 978-1-5106-4393-2. doi:10.1117/12.2592415

- Rösch, T. F., Tischendorf, L., Hartmann, J., Doyle, L., Flaig, L., Berndl, M., **Balling, F.,** Gerlach, S., Bortfeldt, J., Schreiber, J., *Optimization of a permanent magnet quadrupole doublet for laser-accelerated proton bunches at the Centre for Advanced Laser Applications* in *Laser Acceleration of Electrons, Protons, and Ions VI* (eds Bulanov, S. S., Schroeder, C. B. & Schreiber, J.) (SPIE, Online Only, Czech Republic, Apr. 2021), 26. ISBN: 978-1-5106-4392-5 978-1-5106-4393-2. doi:10.1117/12.2588720

- Hartmann, J., Rösch, T. F., **Balling, F.,** Berndl, M., Doyle, L., Flaig, L., Gerlach, S., Tischendorf, L., Schreiber, J., *Commissioning of the laser-driven ion acceleration beamline at the Centre for Advanced Laser Applications* en. in *Laser Acceleration of Electrons, Protons, and Ions VI* arXiv:2111.08461 [hep-ex, physics:physics] (Apr. 2021), 21. doi:10.1117/12.2592407

- Englbrecht, F., **Balling, F.,** Rösch, T. F., Würl, M., Lindner, F. H., Parodi, K., Schreiber, J., Characterization of online high dynamic range imaging for laser-driven ion beam diagnostics using visible light. en. *Current Directions in Biomedical Engineering* **3,** 343–346. ISSN: 2364-5504. doi:10.1515/cdbme-2017-0070 (Sept. 2017)

Conference contributions

- **Poster:** Laser-Driven Ion Acceleration Beamline at the Centre for Advanced Laser Applications. *Flash Radiotherapy and Particle Therapy conference*, virtual, 2021
- **Oral:** Three Dimensional Dose Reconstruction for Laser-Accelerated Ions: The I-BEAT Detector. *SPIE Optics+Optoelectronics Conference 11779*, virtual, 2021
- **Oral:** Three Dimensional Dose Reconstruction for Laser-Accelerated Ions: The I-BEAT Detector. *41st Workshop on High-Energy-Density Physics with Laser and Ion beams*, virtual, 2021
- **Poster:** Ionoacoustic Characterization of Broadband Laser-Driven Proton Sources. *Annual Meeting of the ErUM-FSP APPA*, virtual, 2021
- **Oral:** Development of the I-BEAT: Ionoacoustic Diagnostic for Laser-Driven Ion Sources. *Beam Line Optics and Instrumentation Workshop 4*, virtual, 2020

Supervised theses

- **Master's thesis** *Anna-Katharina Schmidt* Characterization of a Plasma-Acoustic Source for the Calibration of Ultrasonic Transducers (2021).
- **Master's thesis** *Ferdinand Gleixner* Numerical Studies of Ion Acceleration by Irradiation of Spatially Isolated Spheres with an Intense Laser Pulse (2021).
- **Master's thesis** *Moritz Roew* Development of a Novel Ion Energy Spectrometer Using Permanent Magnetic Quadrupoles (2022).
- **Master's thesis** *Vinay Shankar* Paul Trap: Target Monitoring (2023).
- **Bachelor's thesis** *Christine Frank* Development of an Optical Setup to Verify the Temporal Beam Drift of an Ultrashort Pulse Petwatt Laser System (2021).

Bibliography

1. Tajima, T. Laser Electron Accelerator. en. *Physical Review Letters* **43,** 267–270. ISSN: 0031-9007. doi:10.1103/PhysRevLett.43.267 (July 1979).
2. Sung, J. H. 42 PW, 20 fs Ti:sapphire laser at 01 Hz. en. *Optics Letters* **42,** 2058. ISSN: 0146-9592, 1539-4794. doi:10.1364/OL.42.002058 (June 2017).
3. Nakamura, K. Diagnostics, Control and Performance Parameters for the BELLA High Repetition Rate Petawatt Class Laser. *IEEE Journal of Quantum Electronics* **53,** 1–21. ISSN: 0018-9197, 1558-1713. doi:10.1109/JQE.2017.2708601 (Aug. 2017).
4. Schramm, U. First results with the novel petawatt laser acceleration facility in Dresden. *Journal of Physics: Conference Series* **874,** 012028. ISSN: 1742-6588, 1742-6596. doi:10.1088/1742-6596/874/1/012028 (July 2017).
5. Lureau, F. High-energy hybrid femtosecond laser system demonstrating 2 × 10 PW capability. en. *High Power Laser Science and Engineering* **8,** e43. ISSN: 2095-4719, 2052-3289. doi:10.1017/hpl.2020.41 (2020).
6. Esarey, E. Physics of laser-driven plasma-based electron accelerators. en. *Reviews of Modern Physics* **81,** 1229–1285. ISSN: 0034-6861, 1539-0756. doi:10.1103/RevModPhys.81.1229 (Aug. 2009).
7. Malka, V. Laser plasma accelerators. en. *Physics of Plasmas* **19,** 055501. ISSN: 1070-664X, 1089-7674. doi:10.1063/1.3695389 (May 2012).
8. Malka, V. Electron Acceleration by a Wake Field Forced by an Intense Ultrashort Laser Pulse. *Science* **298.** Publisher: American Association for the Advancement of Science, 1596–1600. doi:10.1126/science.1076782 (Nov. 2002).
9. Malka, V. Principles and applications of compact laser–plasma accelerators. en. *Nature Physics* **4.** Publisher: Nature Publishing Group, 447–453. ISSN: 1745-2481. doi:10.1038/nphys966 (June 2008).
10. Albert, F. Betatron oscillations of electrons accelerated in laser wakefields characterized by spectral x-ray analysis. en. *Physical Review E* **77,** 056402. ISSN: 1539-3755, 1550-2376. doi:10.1103/PhysRevE.77.056402 (May 2008).

11. Chen, L. M. Bright betatron X-ray radiation from a laser-driven-clustering gas target. en. *Scientific Reports* **3.** Publisher: Nature Publishing Group, 1912. ISSN: 2045-2322. doi:10.1038/srep01912 (May 2013).

12. Anania, M. P. An ultrashort pulse ultra-violet radiation undulator source driven by a laser plasma wakefield accelerator. en. *Applied Physics Letters* **104,** 264102. ISSN: 0003-6951, 1077-3118. doi:10.1063/1.4886997 (June 2014).

13. Esarey, E. Nonlinear Thomson scattering of intense laser pulses from beams and plasmas. *Physical Review E* **48.** Publisher: American Physical Society, 3003–3021. doi:10.1103/PhysRevE.48.3003 (Oct. 1993).

14. Ride, S. K. Thomson scattering of intense lasers from electron beams at arbitrary interaction angles. *Physical Review E* **52.** Publisher: American Physical Society, 5425–5442. doi:10.1103/PhysRevE.52.5425 (Nov. 1995).

15. Chen, S. MeV-Energy X Rays from Inverse Compton Scattering with Laser-Wakefield Accelerated Electrons. *Physical Review Letters* **110.** Publisher: American Physical Society, 155003. doi:10.1103/PhysRevLett.110.155003 (Apr. 2013).

16. Hegelich, M. MeV Ion Jets from Short-Pulse-Laser Interaction with Thin Foils. *Physical Review Letters* **89.** Publisher: American Physical Society, 085002. doi:10.1103/PhysRevLett.89.085002 (Aug. 2002).

17. Ma, W. Laser Acceleration of Highly Energetic Carbon Ions Using a Double-Layer Target Composed of Slightly Underdense Plasma and Ultrathin Foil. en. *Physical Review Letters* **122.** ISSN: 0031-9007, 1079-7114. doi:10.1103/PhysRevLett.122.014803 (Jan. 2019).

18. Macchi, A. Ion acceleration by superintense laser-plasma interaction. en. *Reviews of Modern Physics* **85,** 751–793. ISSN: 0034-6861, 1539-0756. doi:10.1103/RevModPhys.85.751 (May 2013).

19. Snavely, R. A. Intense High-Energy Proton Beams from Petawatt-Laser Irradiation of Solids. en. *Physical Review Letters* **85,** 2945–2948. ISSN: 0031-9007, 1079-7114. doi:10.1103/PhysRevLett.85.2945 (Oct. 2000).

20. Wilks, S. C. Energetic proton generation in ultra-intense laser–solid interactions. *Physics of Plasmas* **8,** 542–549. ISSN: 1070-664X. doi:10.1063/1.1333697 (Feb. 2001).

21. Prencipe, I. Efficient laser-driven proton and bremsstrahlung generation from cluster-assembled foam targets. *New Journal of Physics* **23,** 093015. ISSN: 1367-2630. doi:10.1088/1367-2630/ac1fcd (Sept. 2021).

22. Wang, W. Free-electron lasing at 27 nanometres based on a laser wakefield accelerator. en. *Nature* **595,** 516–520. ISSN: 0028-0836, 1476-4687. doi:10.1038/s41586-021-03678-x (July 2021).

23. Fourmaux, S. Single shot phase contrast imaging using laser-produced Betatron x-ray beams. en. *Optics Letters* **36,** 2426. ISSN: 0146-9592, 1539-4794. doi:10.1364/OL.36.002426 (July 2011).

24. Cole, J. M. Laser-wakefield accelerators as hard x-ray sources for 3D medical imaging of human bone. en. *Scientific Reports* **5.** Publisher: Nature Publishing Group, 13244. ISSN: 2045-2322. doi:10.1038/srep13244 (Aug. 2015).

25. Cole, J. M. Tomography of human trabecular bone with a laser-wakefield driven x-ray source. en. *Plasma Physics and Controlled Fusion* **58.** Publisher: IOP Publishing, 014008. ISSN: 0741-3335. doi:10.1088/0741-3335/58/1/014008 (Oct. 2015).

26. Kneip, S. Bright spatially coherent synchrotron X-rays from a table-top source. en. *Nature Physics* **6.** Publisher: Nature Publishing Group, 980–983. ISSN: 1745-2481. doi:10.1038/nphys1789 (Dec. 2010).

27. Kneip, S. X-ray phase contrast imaging of biological specimens with femtosecond pulses of betatron radiation from a compact laser plasma wakefield accelerator. en. *Applied Physics Letters* **99,** 093701. ISSN: 0003-6951, 1077-3118. doi:10.1063/1.3627216 (Aug. 2011).

28. Wenz, J. Quantitative X-ray phase-contrast microtomography from a compact laser-driven betatron source. en. *Nature Communications* **6,** 7568. ISSN: 2041-1723. doi:10.1038/ncomms8568 (July 2015).

29. Fedotov, A. Advances in QED with intense background fields. *Physics Reports. Advances in QED with intense background fields* **1010,** 1–138. ISSN: 0370-1573. doi:10.1016/j.physrep.2023.01.003 (Apr. 2023).

30. Bulanov, S. V. Oncological hadrontherapy with laser ion accelerators. *Physics Letters A* **299,** 240–247. ISSN: 0375-9601. doi:10.1016/S0375-9601(02)00521-2 (July 2002).

31. Bulanov, S. V. Feasibility of using laser ion accelerators in proton therapy. en. *Plasma Physics Reports* **28,** 453–456. ISSN: 1562-6938. doi:10.1134/1.1478534 (May 2002).

32. Fourkal, E. Intensity modulated radiation therapy using laser-accelerated protons: a Monte Carlo dosimetric study. en. *Physics in Medicine & Biology* **48,** 3977. ISSN: 0031-9155. doi:10.1088/0031-9155/48/24/001 (Dec. 2003).

33. Malka, V. Practicability of protontherapy using compact laser systems. en. *Medical Physics* **31,** 1587–1592. ISSN: 2473-4209. doi:10.1118/1.1747751 (2004).

34. Cobble, J. A. High resolution laser-driven proton radiography. en. *Journal of Applied Physics* **92,** 1775–1779. ISSN: 0021-8979, 1089-7550. doi:10.1063/1.1494128 (Aug. 2002).

35. Mackinnon, A. J. Proton Radiography of a Laser-Driven Implosion. *Physical Review Letters* **97.** Publisher: American Physical Society, 045001. doi:10.1103/PhysRevLett.97.045001 (July 2006).

36. Borghesi, M. Multi-MeV Proton Source Investigations in Ultraintense Laser-Foil Interactions. *Physical Review Letters* **92.** Publisher: American Physical Society, 055003. doi:10.1103/PhysRevLett.92.055003 (Feb. 2004).

37. Roth, M. Energetic ions generated by laser pulses: A detailed study on target properties. *Physical Review Special Topics - Accelerators and Beams* **5.** Publisher: American Physical Society, 061301. doi:10.1103/PhysRevSTAB.5.061301 (June 2002).

38. Patel, P. K. Isochoric Heating of Solid-Density Matter with an Ultrafast Proton Beam. *Physical Review Letters* **91.** Publisher: American Physical Society, 125004. doi:10.1103/PhysRevLett.91.125004 (Sept. 2003).

39. Snavely, R. A. Laser generated proton beam focusing and high temperature isochoric heating of solid matter. en. *Physics of Plasmas* **14,** 092703. ISSN: 1070-664X, 1089-7674. doi:10.1063/1.2774001 (Sept. 2007).

40. Antici, P. A compact post-acceleration scheme for laser-generated protons. en. *Physics of Plasmas* **18,** 073103. ISSN: 1070-664X, 1089-7674. doi:10.1063/1.3574361 (July 2011).

41. Tabak, M. Ignition and high gain with ultrapowerful lasers*. en. *Physics of Plasmas* **1,** 1626–1634. ISSN: 1070-664X, 1089-7674. doi:10.1063/1.870664 (May 1994).

42. Roth, M. Fast Ignition by Intense Laser-Accelerated Proton Beams. *Physical Review Letters* **86.** Publisher: American Physical Society, 436–439. doi:10.1103/PhysRevLett.86.436 (Jan. 2001).

43. Key, M. H. Status of and prospects for the fast ignition inertial fusion concept. en. *Physics of Plasmas* **14,** 055502. ISSN: 1070-664X, 1089-7674. doi:10.1063/1.2719178 (May 2007).

44. Hegelich, B. M. Experimental demonstration of particle energy, conversion efficiency and spectral shape required for ion-based fast ignition. en. *Nuclear Fusion* **51,** 083011. ISSN: 0029-5515. doi:10.1088/0029-5515/51/8/083011 (July 2011).

45. Norreys, P. A. Neutron production from picosecond laser irradiation of deuterated targets at intensities of. en. *Plasma Physics and Controlled Fusion* **40,** 175–182. ISSN: 0741-3335, 1361-6587. doi:10.1088/0741-3335/40/2/001 (Feb. 1998).

46. Kar, S. Beamed neutron emission driven by laser accelerated light ions. en. *New Journal of Physics* **18.** Publisher: IOP Publishing, 053002. ISSN: 1367-2630. doi:10.1088/1367-2630/18/5/053002 (Apr. 2016).

47. Higginson, D. P. Laser generated neutron source for neutron resonance spectroscopy. en. *Physics of Plasmas* **17,** 100701. ISSN: 1070-664X, 1089-7674. doi:10.1063/1.3484218 (Oct. 2010).

48. Higginson, D. P. Production of neutrons up to 18 MeV in high-intensity, short-pulse laser matter interactions. *Physics of Plasmas* **18,** 100703. ISSN: 1070-664X. doi:10.1063/1.3654040 (Oct. 2011).

49. Thornton, J. The detection and sizing of flaws in components from the hot-end of gas turbines using phase-contrast radiography with neutrons: a feasibility study. *NDT & E International* **36,** 289–295. ISSN: 0963-8695. doi:10.1016/S0963-8695(03)00007-0 (July 2003).

50. Seki, Y. A Simulation Study of Fast Neutron Imaging for Large-scale Concrete Structures. *Physics Procedia. 3rd International Meeting of the Union for Compact Accelerator-driven Neutron Sources, UCANS III, 31 July–3 August 2012, Bilbao, Spain & the 4th International Meeting of the Union for Compact Accelerator-driven Neutron Sources, UCANS IV, 23-27 September 2013, Sapporo, Hokkaido, Japan* **60,** 324–326. ISSN: 1875-3892. doi:10.1016/j.phpro.2014.11.043 (Jan. 2014).

51. Fuchs, J. Laser-driven proton scaling laws and new paths towards energy increase. en. *Nature Physics* **2,** 48–54. ISSN: 1745-2473, 1745-2481. doi:10.1038/nphys199 (Jan. 2006).

52. Wilks, S. C. Absorption of ultra-intense laser pulses. en. *Physical Review Letters* **69,** 1383–1386. ISSN: 0031-9007. doi:10.1103/PhysRevLett.69.1383 (Aug. 1992).

53. Palmer, C. A. J. Monoenergetic Proton Beams Accelerated by a Radiation Pressure Driven Shock. en. *Physical Review Letters* **106,** 014801. ISSN: 0031-9007, 1079-7114. doi:10.1103/PhysRevLett.106.014801 (Jan. 2011).

54. Haberberger, D. Collisionless shocks in laser-produced plasma generate monoenergetic high-energy proton beams. en. *Nature Physics* **8.** Number: 1 Publisher: Nature Publishing Group, 95–99. ISSN: 1745-2481. doi:10.1038/nphys2130 (Jan. 2012).

55. Chen, Y.-H. *Observation of monoenergetic protons from a near-critical gas target tailored by a hydrodynamic shock* in *Laser Acceleration of Electrons, Protons, and Ions III; and Medical Applications of Laser-Generated Beams of Particles III* **9514** (SPIE, May 2015), 28–33. doi:10.1117/12.2182094.

56. Tresca, O. Spectral Modification of Shock Accelerated Ions Using a Hydrodynamically Shaped Gas Target. en. *Physical Review Letters* **115,** 094802. ISSN: 0031-9007, 1079-7114. doi:10.1103/PhysRevLett.115.094802 (Aug. 2015).

57. Henig, A. Enhanced Laser-Driven Ion Acceleration in the Relativistic Transparency Regime. *Physical Review Letters* **103.** Publisher: American Physical Society, 045002. doi:10.1103/PhysRevLett.103.045002 (July 2009).

58. Hegelich, B. M. Laser-driven ion acceleration from relativistically transparent nanotargets. en. *New Journal of Physics* **15.** Publisher: IOP Publishing, 085015. ISSN: 1367-2630. doi:10.1088/1367-2630/15/8/085015 (Aug. 2013).

59. Jung, D. Beam profiles of proton and carbon ions in the relativistic transparency regime. en. *New Journal of Physics* **15.** Publisher: IOP Publishing, 123035. ISSN: 1367-2630. doi:10.1088/1367-2630/15/12/123035 (Dec. 2013).

60. Jung, D. Efficient carbon ion beam generation from laser-driven volume acceleration. en. *New Journal of Physics* **15.** Publisher: IOP Publishing, 023007. ISSN: 1367-2630. doi:10.1088/1367-2630/15/2/023007 (Feb. 2013).

61. Ziegler, T. Laser-driven high-energy proton beams from cascaded acceleration regimes. en. *Nature Physics.* Publisher: Nature Publishing Group, 1–6. ISSN: 1745-2481. doi:10.1038/s41567-024-02505-0 (May 2024).

62. Wagner, F. Maximum Proton Energy above 85 MeV from the Relativistic Interaction of Laser Pulses with Micrometer Thick CH 2 Targets. en. *Physical Review Letters* **116.** ISSN: 0031-9007, 1079-7114. doi:10.1103/PhysRevLett.116.205002 (May 2016).

63. Higginson, A. Near-100 MeV protons via a laser-driven transparency-enhanced hybrid acceleration scheme. en. *Nature Communications* **9.** ISSN: 2041-1723. doi:10.1038/s41467-018-03063-9 (Dec. 2018).

64. Ter-Avetisyan, S. Generation of a quasi-monoergetic proton beam from laser-irradiated sub-micron droplets. en. *Physics of Plasmas* **19,** 073112. ISSN: 1070-664X, 1089-7674. doi:10.1063/1.4731712 (July 2012).

65. Sokollik, T. Directional Laser-Driven Ion Acceleration from Microspheres. *Physical Review Letters* **103.** Publisher: American Physical Society, 135003. doi:10.1103/PhysRevLett.103.135003 (Sept. 2009).

66. Ter-Avetisyan, S. Quasimonoenergetic Deuteron Bursts Produced by Ultraintense Laser Pulses. en. *Physical Review Letters* **96,** 145006. ISSN: 0031-9007, 1079-7114. doi:10.1103/PhysRevLett.96.145006 (Apr. 2006).

67. Buffechoux, S. Hot Electrons Transverse Refluxing in Ultraintense Laser-Solid Interactions. en. *Physical Review Letters* **105,** 015005. ISSN: 0031-9007, 1079-7114. doi:10.1103/PhysRevLett.105.015005 (July 2010).

68. Zeil, K. Robust energy enhancement of ultrashort pulse laser accelerated protons from reduced mass targets. en. *Plasma Physics and Controlled Fusion* **56.** Publisher: IOP Publishing, 084004. ISSN: 0741-3335. doi:10.1088/0741-3335/56/8/084004 (July 2014).

69. Ostermayr, T. M. A transportable Paul-trap for levitation and accurate positioning of micron-scale particles in vacuum for laser-plasma experiments. en. *Review of Scientific Instruments* **89,** 013302. ISSN: 0034-6748, 1089-7623. doi:10.1063/1.4995955 (Jan. 2018).

70. Paul, W. Electromagnetic traps for charged and neutral particles. *Reviews of Modern Physics* **62.** Publisher: American Physical Society, 531–540. doi:10.1103/RevModPhys.62.531 (July 1990).

71. Gebhard, J. *Laser Ion-Acceleration from tailored Micro-Plasmas* en. PhD Thesis (LMU Munich, Munich, Germany, June 2022).

72. Gebhard, J. Two-stage laser proton acceleration from levitating near-critical microplasmas. *In Preparation* (2024).

73. Ostermayr, T. M. Proton acceleration by irradiation of isolated spheres with an intense laser pulse. *Physical Review E* **94.** ISSN: 2470-0045. doi:10.1103/physreve.94.033208 (Sept. 2016).

74. Hilz, P. Isolated proton bunch acceleration by a petawatt laser pulse. *Nature Communications* **9.** ISSN: 2041-1723. doi:10.1038/s41467-017-02663-1 (Jan. 2018).

75. Speicher, M. *Optical Probing of Laser-Induced Expansion of Levitating Microspheres* en. PhD Thesis (LMU Munich, Munich, Germany, May 2022).

76. *Texas Petawatt Laser Temporal Contrast* https://texaspetawatt.ph.utexas.edu/contrast.php (2024).

77. Gleixner, F. *Numerical Studies of Ion Acceleration by Irradiation of Spatially Isolated Spheres with an Intense Laser Pulse* MA thesis (LMU Munich, Munich, Germany, May 2021).

78. Maiman, T. H. Stimulated Optical Radiation in Ruby. en. *Nature* **187,** 493–494. ISSN: 0028-0836, 1476-4687. doi:10.1038/187493a0 (Aug. 1960).

79. McClung, F. J. Giant Optical Pulsations from Ruby. en. *Journal of Applied Physics* **33,** 828–829. ISSN: 0021-8979, 1089-7550. doi:10.1063/1.1777174 (Mar. 1962).

80. Weiner, A. M. *Ultrafast optics* en. ISBN: 978-0-471-41539-8 (Wiley, Hoboken, N.J, 2009).

81. Kerr, J. A new relation between electricity and light: Dielectrified media birefringent. en. *The London, Edinburgh, and Dublin Philosophical Magazine and Journal of Science* **50,** 337–348. ISSN: 1941-5982, 1941-5990. doi:10.1080/14786447508641302 (Nov. 1875).

82. Kerr, J. A new relation between electricity and light: Dielectrified media birefringent (Second paper). en. *The London, Edinburgh, and Dublin Philosophical Magazine and Journal of Science* **50,** 446–458. ISSN: 1941-5982, 1941-5990. doi:10.1080/14786447508641319 (Dec. 1875).

83. Bussière, B. Bulk laser-induced damage threshold of titanium-doped sapphire crystals. EN. *Applied Optics* **51.** Publisher: Optica Publishing Group, 7826–7833. ISSN: 2155-3165. doi:10.1364/AO.51.007826 (Nov. 2012).

84. Strickland, D. Compression of amplified chirped optical pulses. en. *Optics Communications* **55,** 447–449. ISSN: 00304018. doi:10.1016/0030-4018(85)90151-8 (Oct. 1985).

85. Yoon, J. W. Achieving the laser intensity of 55×10^{22} W/cm ^{2} with a wavefront-corrected multi-PW laser. en. *Optics Express* **27,** 20412. ISSN: 1094-4087. doi:10.1364/OE.27.020412 (July 2019).

86. Cerullo, G. Ultrafast optical parametric amplifiers. en. *Review of Scientific Instruments* **74,** 1–18. ISSN: 0034-6748, 1089-7623. doi:10.1063/1.1523642 (Jan. 2003).

87. Didenko, N. V. Contrast degradation in a chirped-pulse amplifier due to generation of prepulses by postpulses. en. *Optics Express* **16,** 3178. ISSN: 1094-4087. doi:10.1364/OE.16.003178 (2008).

88. Kiriyama, H. Experimental investigation on the temporal contrast of pre-pulses by post-pulses in a petawatt laser facility. en. *Optics Letters* **45,** 1100. ISSN: 0146-9592, 1539-4794. doi:10.1364/OL.384759 (Mar. 2020).

89. Roeder, S. How the laser beam size conditions the temporal contrast in pulse stretchers of chirped-pulse amplification lasers. en. *High Power Laser Science and Engineering* **10.** Publisher: Cambridge University Press, e34. ISSN: 2095-4719, 2052-3289. doi:10.1017/hpl.2022.18 (Jan. 2022).

90. Hillier, D. Ultrahigh contrast from a frequency-doubled chirped-pulse-amplification beamline. en. *Applied Optics* **52,** 4258. ISSN: 1559-128X, 2155-3165. doi:10.1364/AO.52.004258 (June 2013).

91. Obst, L. On-shot characterization of single plasma mirror temporal contrast improvement. en. *Plasma Physics and Controlled Fusion* **60,** 054007. ISSN: 0741-3335, 1361-6587. doi:10.1088/1361-6587/aab3bb (May 2018).

92. Trebino, R. Measuring ultrashort laser pulses in the time-frequency domain using frequency-resolved optical gating. en. *Review of Scientific Instruments* **68,** 3277–3295. ISSN: 0034-6748, 1089-7623. doi:10.1063/1.1148286 (Sept. 1997).

93. Oksenhendler, T. Self-referenced spectral interferometry. en. *Applied Physics B* **99,** 7–12. ISSN: 0946-2171, 1432-0649. doi:10.1007/s00340-010-3916-y (Apr. 2010).

94. Trisorio, A. Self-referenced spectral interferometry for ultrashort infrared pulse characterization. EN. *Optics Letters* **37.** Publisher: Optica Publishing Group, 2892–2894. ISSN: 1539-4794. doi:10.1364/OL.37.002892 (July 2012).

95. Iaconis, C. Spectral phase interferometry for direct electric-field reconstruction of ultrashort optical pulses. EN. *Optics Letters* **23.** Publisher: Optica Publishing Group, 792–794. ISSN: 1539-4794. doi:10.1364/OL.23.000792 (May 1998).

96. Dorrer, C. High-dynamic-range single-shot cross-correlator based on an optical pulse replicator. en. *Optics Express* **16,** 13534. ISSN: 1094-4087. doi:10.1364/OE.16.013534 (Sept. 2008).

97. Shah, R. C. Large temporal window contrast measurement using optical parametric amplification and low-sensitivity detectors. en. *The European Physical Journal D* **55,** 305–309. ISSN: 1434-6060, 1434-6079. doi:10.1140/epjd/e2009-00152-3 (Nov. 2009).

98. Wang, Y. Single-shot measurement of >1010 pulse contrast for ultra-high peak-power lasers. en. *Scientific Reports* **4.** Publisher: Nature Publishing Group, 3818. ISSN: 2045-2322. doi:10.1038/srep03818 (Jan. 2014).

99. Tavella, F. High-dynamic range pulse-contrast measurements of a broadband optical parametric chirped-pulse amplifier. en. *Applied Physics B* **81,** 753–756. ISSN: 1432-0649. doi:10.1007/s00340-005-1966-3 (Oct. 2005).

100. Luan, S. High dynamic range third-order correlation measurement of picosecond laser pulse shapes. en. *Measurement Science and Technology* **4,** 1426–1429. ISSN: 0957-0233, 1361-6501. doi:10.1088/0957-0233/4/12/018 (Dec. 1993).

101. Platt, B. C. History and Principles of Shack-Hartmann Wavefront Sensing. en. *Journal of Refractive Surgery* **17.** ISSN: 1081-597X. doi:10.3928/1081-597X-20010901-13 (Sept. 2001).

102. Chanteloup, J.-C. Multiple-wave lateral shearing interferometry for wave-front sensing. en. *Applied Optics* **44,** 1559. ISSN: 0003-6935, 1539-4522. doi:10.1364/AO.44.001559 (Mar. 2005).

103. Lindner, F. Towards swift ion bunch acceleration by high-power laser pulses at the Centre for Advanced Laser Applications (CALA). en. *Nuclear Instruments and Methods in Physics Research Section B: Beam Interactions with Materials and Atoms* **402,** 354–357. ISSN: 0168583X. doi:10.1016/j.nimb.2017.02.088 (July 2017).

104. Nubbemeyer, T. 1 kW, 200 mJ picosecond thin-disk laser system. en. *Optics Letters* **42,** 1381. ISSN: 0146-9592, 1539-4794. doi:10.1364/OL.42.001381 (Apr. 2017).

105. Hartmann, J. *Quantitative Ion Spectrometry and first laser-ion acceleration results at the Centre for Advanced Laser Applications* PhD thesis (Ludwig-Maximilians-Universität München, July 2022).

106. Frank, C. *Development of an Optical Setup to Verify the Temporal Beam Drift of an Ultrashort Pulse Petwatt Laser System* Bachelor Thesis (LMU Munich, Munich, Germany, Dec. 2021).

107. Hartmann, J. The spatial contrast challenge for intense laser-plasma experiments. *Journal of Physics: Conference Series* **1079,** 012003. ISSN: 1742-6588, 1742-6596. doi:10.1088/1742-6596/1079/1/012003 (Aug. 2018).

108. Schaefer, P. *Attenuation of a Petawatt Class Laser System* PhD thesis (LMU Munich, Munich, Germany, Sept. 2024).

109. Reinhardt, S. Test of pixel detectors for laser-driven accelerated particle beams. en. *Journal of Instrumentation* **6,** C12030–C12030. ISSN: 1748-0221. doi:10.1088/1748-0221/6/12/C12030 (Dec. 2011).

110. Reinhardt, S. A pixel detector system for laser-accelerated ion detection. en. *Journal of Instrumentation* **8,** P03008–P03008. ISSN: 1748-0221. doi:10.1088/1748-0221/8/03/P03008 (Mar. 2013).

111. Ashkin, A. Acceleration and Trapping of Particles by Radiation Pressure. *Physical Review Letters* **24.** Publisher: American Physical Society, 156–159. doi:10.1103/PhysRevLett.24.156 (Jan. 1970).

112. Ashkin, A. Observation of a single-beam gradient force optical trap for dielectric particles. EN. *Optics Letters* **11.** Publisher: Optica Publishing Group, 288–290. ISSN: 1539-4794. doi:10.1364/OL.11.000288 (May 1986).

113. Rohatschek, H. Direction, magnitude and causes of photophoretic forces. *Journal of Aerosol Science* **16,** 29–42. ISSN: 0021-8502. doi:10.1016/0021-8502(85)90018-7 (Jan. 1985).

114. Yamanaka, C. in *Physics of laser plasma* (eds Rubenčik, A. M. *et al.*) *Handbook of plasma physics* 3 (North-Holland, 1991). ISBN: 0-444-87426-7.

115. Drake, R. P. *High-Energy-Density Physics* ISBN: 978-3-319-67710-1 978-3-319-67711-8. doi:10.1007/978-3-319-67711-8 (Springer International Publishing, Cham, 2018).

116. Eliezer, S. *The interaction of high-power lasers with plasmas* en. ISBN: 978-0-7503-0747-5 (CRC Press, Taylor & Francis Group, Boca Raton London New York, 2002).

117. Gibbon, P. *Short pulse laser interactions with matter: an introduction* Reprinted. en. ISBN: 978-1-86094-135-1 (Imperial College Press, London, 2007).

118. Rosenbluth, M. N. *Handbook of plasma physics* eng. ISBN: 978-0-444-87426-9 (North-Holland, Amsterdam London New York [etc.], 1991).

119. Barjot, G. Multiphoton Ionization of Hydrogen and Rare Gases. en. *IEEE Journal of Quantum Electronics* **4,** 667–669. doi:10.1109/JQE.1968.1074955 (1968).

120. Keldysh, L. V. Ionization in the Field of a Strong Electromagnetic Wave. *Zh. Eksperim. i Teor. Fiz.* **47** (Nov. 1964).

121. *NIST Digital Library of Mathematical Functions* https://dlmf.nist.gov/, Release 1.2.1 of 2024-06-15. F. W. J. Olver, A. B. Olde Daalhuis, D. W. Lozier, B. I. Schneider, R. F. Boisvert, C. W. Clark, B. R. Miller, B. V. Saunders, H. S. Cohl, and M. A. McClain, eds.

122. Duchateau, G. Modeling the solid-to-plasma transition for laser imprinting in direct-drive inertial confinement fusion. en. *Physical Review E* **100,** 033201. ISSN: 2470-0045, 2470-0053. doi:10.1103/PhysRevE.100.033201 (Sept. 2019).

123. Dere, K. P. CHIANTI - an atomic database for emission lines: I. Wavelengths greater than 50 Å. *Astronomy and Astrophysics Supplement Series* **125,** 149–173. ISSN: 0365-0138, 1286-4846. doi:10.1051/aas:1997368 (Oct. 1997).

124. Zanna, G. D. CHIANTI—An Atomic Database for Emission Lines. XVI. Version 10, Further Extensions. en. *The Astrophysical Journal* **909.** Publisher: The American Astronomical Society, 38. ISSN: 0004-637X. doi:10.3847/1538-4357/abd8ce (Mar. 2021).

125. Rethfeld, B. Modelling ultrafast laser ablation. en. *Journal of Physics D: Applied Physics* **50.** Publisher: IOP Publishing, 193001. ISSN: 0022-3727. doi:10.1088/1361-6463/50/19/193001 (Apr. 2017).

126. Bernert, C. Transient Laser-Induced Breakdown of Dielectrics in Ultrarelativistic Laser-Solid Interactions. *Physical Review Applied* **19.** Publisher: American Physical Society, 014070. doi:10.1103/PhysRevApplied.19.014070 (Jan. 2023).

127. Du, D. Laser-induced breakdown by impact ionization in SiO2 with pulse widths from 7 ns to 150 fs. en. *Applied Physics Letters* **64,** 3071–3073. ISSN: 0003-6951, 1077-3118. doi:10.1063/1.111350 (June 1994).

128. Stuart, B. C. Laser-Induced Damage in Dielectrics with Nanosecond to Subpicosecond Pulses. en. *Physical Review Letters* **74,** 2248–2251. ISSN: 0031-9007, 1079-7114. doi:10.1103/PhysRevLett.74.2248 (Mar. 1995).

129. Stuart, B. C. Nanosecond-to-femtosecond laser-induced breakdown in dielectrics. *Physical Review B* **53.** Publisher: American Physical Society, 1749–1761. doi:10.1103/PhysRevB.53.1749 (Jan. 1996).

130. Chimier, B. Damage and ablation thresholds of fused-silica in femtosecond regime. *Physical Review B* **84.** Publisher: American Physical Society, 094104. doi:10.1103/PhysRevB.84.094104 (Sept. 2011).

131. Déziel, J.-L. Dynamical rate equation model for femtosecond laser-induced breakdown in dielectrics. *Physical Review B* **104.** Publisher: American Physical Society, 045201. doi:10.1103/PhysRevB.104.045201 (July 2021).

132. Bernert, C. *Plasma dynamics between laserinduced breakdown and relativistically induced transparency: An investigation of high-intensity lasersolid interactions by time-resolved offharmonic optical shadowgraphy* PhD thesis (Technical University Dresden, Dresden, Germany, 2023).

133. Pineau, A. Improved modeling of the solid-to-plasma transition of polystyrene ablator for laser direct-drive inertial confinement fusion hydrocodes. *Physical Review E* **104.** Publisher: American Physical Society, 015210. doi:10.1103/PhysRevE.104.015210 (July 2021).

134. Gibbon, P. Short-pulse laser - plasma interactions. en. *Plasma Physics and Controlled Fusion* **38,** 769. ISSN: 0741-3335. doi:10.1088/0741-3335/38/6/001 (June 1996).

135. Wang, D. Laser-induced damage thresholds of ultrathin targets and their constraint on laser contrast in laser-driven ion acceleration experiments. en. *High Power Laser Science and Engineering* **8,** e41. ISSN: 2095-4719, 2052-3289. doi:10.1017/hpl.2020.40 (Jan. 2020).

136. Kruer, W. L. *The physics of laser plasma interactions* en. ISBN: 978-0-8133-4083-8 (Boulder, Colo. [u.a.] Westview, 2003).

137. Rozmus, W. Skin effect and interaction of short laser pulses with dense plasmas. *Physical Review A* **42.** Publisher: American Physical Society, 7401–7412. doi:10.1103/PhysRevA.42.7401 (Dec. 1990).

138. Brunel, F. Not-so-resonant, resonant absorption. en. *Physical Review Letters* **59,** 52–55. ISSN: 0031-9007. doi:10.1103/PhysRevLett.59.52 (July 1987).

139. Gibbon, P. Collisionless absorption in sharp-edged plasmas. en. *Physical Review Letters* **68,** 1535–1538. ISSN: 0031-9007. doi:10.1103/PhysRevLett.68.1535 (Mar. 1992).

140. Rybicki, G. B. *Radiative processes in astrophysics* eng. ISBN: 978-0-471-82759-7 (J. Wiley and sons, New York Chichester Brisbane [etc.], 1979).

141. Zhou, M. L. The impact of femtosecond pre-pulses on nanometer thin foils for laser-ion acceleration. en. *Plasma Physics and Controlled Fusion* **59,** 055020. ISSN: 0741-3335, 1361-6587. doi:10.1088/1361-6587/aa66cf (May 2017).

142. Basko, M. M. en. in *Photon Sources for Lithograpy and Metrology* 149–195 (SPIE Press, Bellingham, Washington, 2023).

143. Basko, M. M. RALEF-2D: A 2D hydrodynamic code with heat conduction and radiation transport. en (2017).

144. Addessio, F. *CAVEAT: A computer code for fluid dynamics problems with large distortion and internal slip. Revision 1* tech. rep. LA–10613-MS-Rev.1, 10143914, ON: DE92014078 (May 1992), LA–10613–MS–Rev.1, 10143914, ON: DE92014078. doi:10.2172/10143914.

145. Bernert, C. Off-harmonic optical probing of high intensity laser plasma expansion dynamics in solid density hydrogen jets. en. *Scientific Reports* **12,** 7287. ISSN: 2045-2322. doi:10.1038/s41598-022-10797-6 (Dec. 2022).

Appendices

Appendix A.

Light Propagation and Fourier Optics

When trying to diagnose high power laser plasma interactions, a major challenge is the bright light emitted from the focus region. This makes direct high resolution imaging of the interaction volume basically impossible. A possible work around is to use the light transmitted around and through the target and gain insight into the plasma state from the diffraction patterns.

To be able to interpret these images, a model for the light propagation is necessary.

A.1. Fresnel-Kirchhoff Integrals

Any diffraction pattern can usually be described by the Fresnel-Kirchhoff diffraction formula

$$U(P_0) = \frac{A}{j\lambda} \iint_{\text{Aper}} \left\{ \frac{\exp\left[jk(r_{21} + r_{01})\right]}{r_{21} r_{01}} \left[\frac{\cos(\vec{n}, \vec{r_{01}}) - \cos(\vec{n}, \vec{r_{21}})}{2} \right] \right\} dS. \tag{A.1}$$

It relates the field U a point P_0 to the integral of the illuminating field with amplitude A over the aperture. λ is the wavelength of the light and k the wave vector. $\vec{n}$ is the normal vector on the aperture, $\vec{r_{01}}$ the vector from the point source to the aperture and $\vec{r_{21}}$ the vector from the aperture to the detector.

While this is a general formulation of diffraction, the calculation is inefficient, as it requires a full two-dimensional integration to be performed for each point in the detection plane.

Under certain conditions, approximations can be made which make the solution significantly easier.

A.2. Fresnel and Fraunhofer Approximation

For a moderate distance from the aperture the Fresnel-Kirchhoff formula can be simplified to the Fresnel approximation

$$\begin{aligned} U(\xi,\eta) =& \frac{e^{jkz}}{j\lambda z} \exp\left[j\frac{k}{2z}(\xi^2+\eta^2)\right] \iint \left\{U(x,y)\exp\left[j\frac{k}{2z}(x^2+y^2)\right]\right\} \\ & \times \exp\left[-j\frac{k}{z}(x\xi+y\eta)\right] dxdy \end{aligned} \tag{A.2}$$

The distance has to satisfy the condition

$$z \gg \left\{\frac{\pi}{4\lambda}\left[(x-\xi)^2+(y-\eta)^2\right]^2_{max}\right\}^{\frac{1}{3}}. \tag{A.3}$$

For even further distances, in the so called far field, the diffraction integral simplifies even further. The condition here is

$$z \gg \frac{k}{2}(\xi^2+\eta^2)_{max}. \tag{A.4}$$

In this case the quadratic phase term in the Fresnel propagator reduces to unity and the integral reduces to a Fourier transform of the initial field multiplied with a phase term:

$$U(\xi,\eta) = \frac{e^{jkz}}{j\lambda z} \exp\left[j\frac{k}{2z}(\xi^2+\eta^2)\right] \iint U(x,y)\exp\left[-j\frac{2\pi}{\lambda z}(x\xi+y\eta)\right] dxdy \tag{A.5}$$

A.3. Formulation using Fourier Transforms

To make the calculation of the Fresnel and Fraunhofer integrals easier they can be formulated in terms of Fourier transformations:

$$G(f_x,f_y) = \mathrm{FT}[g(x,y)] = \iint g(x,y)\exp\left[-j2\pi(f_x x+f_y y)\right] dxdy \tag{A.6}$$

$$g(x,y) = \mathrm{iFT}[G(f_x,f_y)] = \iint G(f_x,f_y)\exp\left[j2\pi(f_x x+f_y y)\right] df_x df_y \tag{A.7}$$

For the Fresnel integral it is instructive to first reformulate it as a convolution:

$$U(\xi,\eta) = \iint U(x,y)h(\xi - x, \eta - y)dxdy \tag{A.8}$$

with

$$h(x,y) = \frac{e^{jkz}}{j\lambda z} \exp\left[j\frac{k}{2z}(x^2+y^2)\right]. \tag{A.9}$$

Now the convolution theorem can be applied to express Equation (A.2) as

$$U(\xi,\eta) = \mathrm{iFT}\left\{\mathrm{FT}\left[U(x,y)\right] H(f_x,f_y)\right\} \tag{A.10}$$

with the Fresnel propagator

$$H(f_x,f_y) = \mathrm{FT}\left\{h(x,y)\right\} = e^{jkz}\exp\left[-j\pi\lambda z(f_x^2+f_y^2)\right]. \tag{A.11}$$

For the Fraunhofer integral the Fourier transform can be directly identified and it is then formulated as

$$U(\xi,\eta) = \frac{e^{jkz}}{j\lambda z}\exp\left[j\frac{k}{2z}(\xi^2+\eta^2)\right]\mathrm{FT}\left[U(x,y)\right]. \tag{A.12}$$

A.4. Discretization to FFT

For numerical calculation of light propagation it is often useful to sample the field on a regular grid. The propagation described above can then be performed with the discrete Fourier transformations:

$$\begin{aligned} G(f_x^i, f_y^k) &= \mathrm{DFT}[g(x,y)] \\ &= \sum_{n=0}^{N-1}\sum_{m=0}^{N-1} g(x_n,y_m)\exp\left[-j2\pi\frac{(f_x^i x_n + f_y^k y_m)}{N}\right] \end{aligned} \tag{A.13}$$

$$\begin{aligned} g(x_n, y_m) &= \mathrm{iDFT}[g(x,y)] \\ &= \frac{1}{N^2}\sum_{i=0}^{N-1}\sum_{k=0}^{N-1} G(f_x^i,f_y^k)\exp\left[j2\pi\frac{(f_x^i x_n + f_y^k y_m)}{N}\right] \end{aligned} \tag{A.14}$$

For the calculation of these transformations the highly efficient Fast-Fourier-Transform (FFT) algorithm exists, making these calculations very fast. In particular, compared to

direct numerical solving of the Fresnel-Kirchhoff integral the use of the FFT algorithm makes this orders of magnitude faster.

A.5. Numerical Results for Transmission Images

To simulate the transmission image the scalar field distribution is initialized with the experimentally recorded nearfield intensity and a uniform phase. From there the field is propagated to the focus with a direct Fourier transform, before being propagated to the target plane using the Fresnel approximation. There the effect of the target is applied as an intensity and phase change (cp. Section 2.4). Finally, the field is propagated to the screen plane using the Fraunhofer approximation.

In the following the simulated transmission images for different central densities are shown, after subtracting the transmission without target. In the left column the target is placed on the optical axis, in the middle column 2 µm from the axis, and in the right column 4 µm from the axis. For the different rows the target is placed at different up- and downstream positions, concretely at $-100\,\mu m$, $-50\,\mu m$, $0\,\mu m$, $50\,\mu m$, $100\,\mu m$ from top to bottom where zero is the focus position and the laser propagates in positive direction.

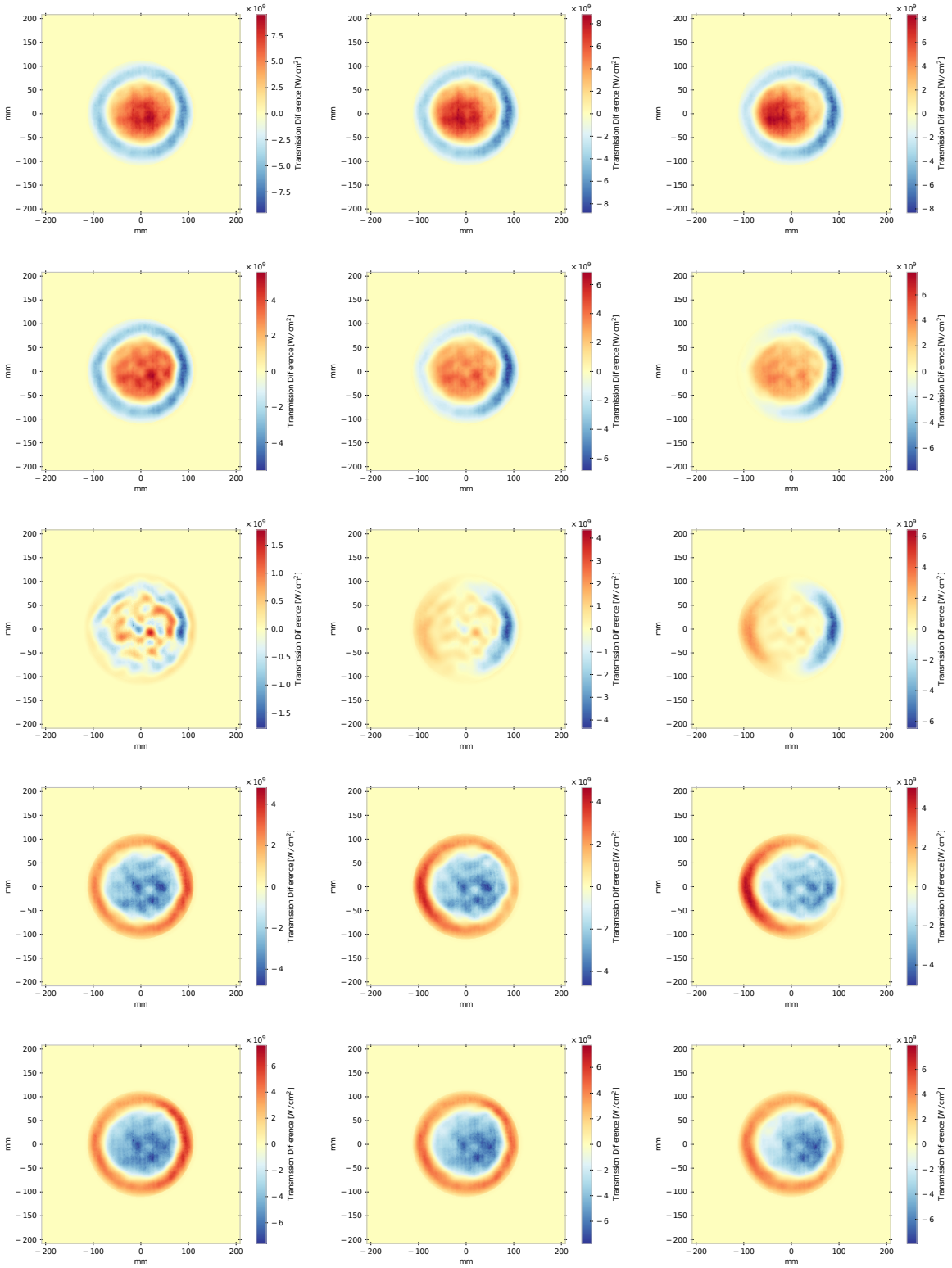

Figure A.1.: **Transmission Images for** $n_0 = 0.01\,\mathrm{n_c}$

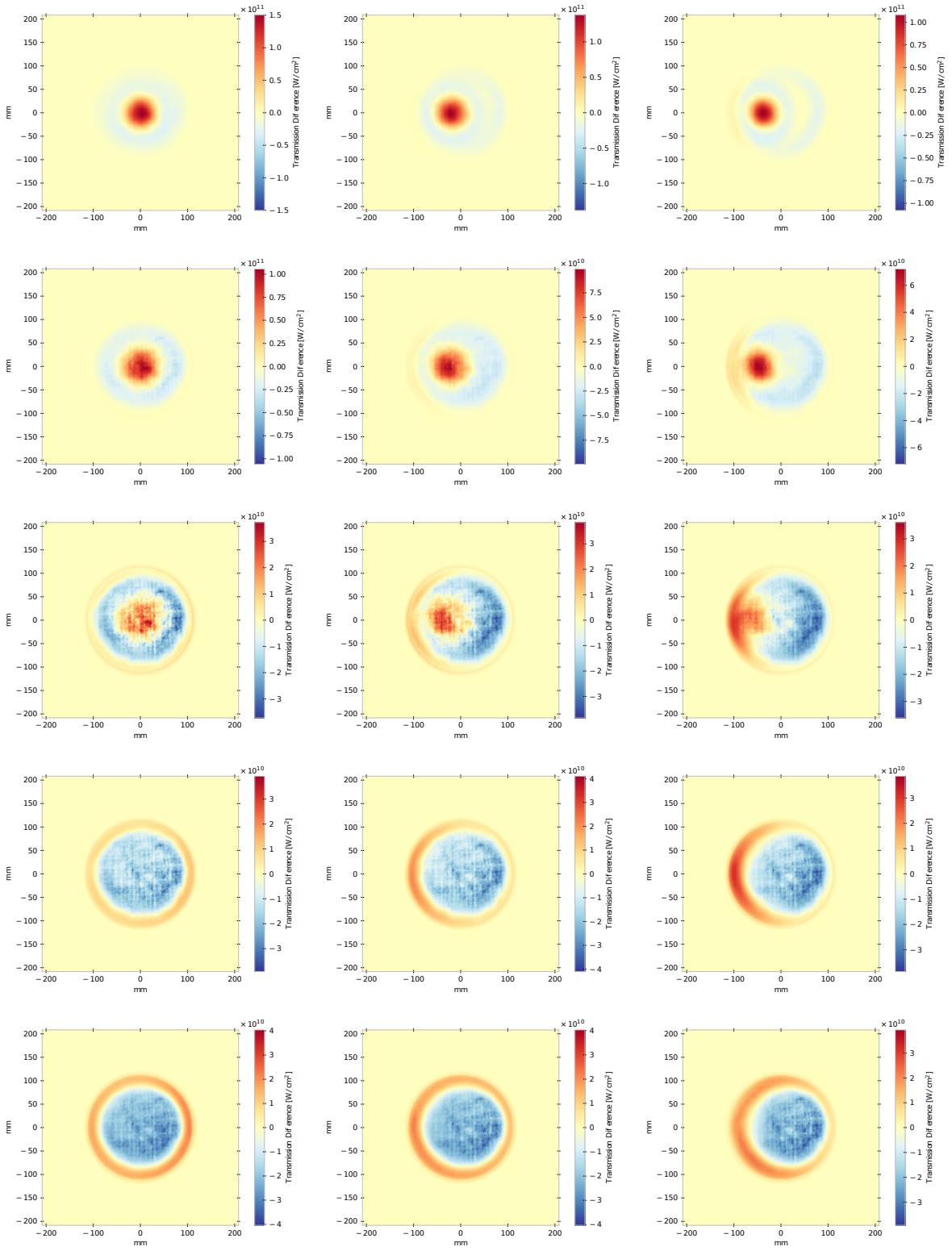

Figure A.2.: **Transmission Images for** $n_0 = 0.1\,\mathrm{n_c}$

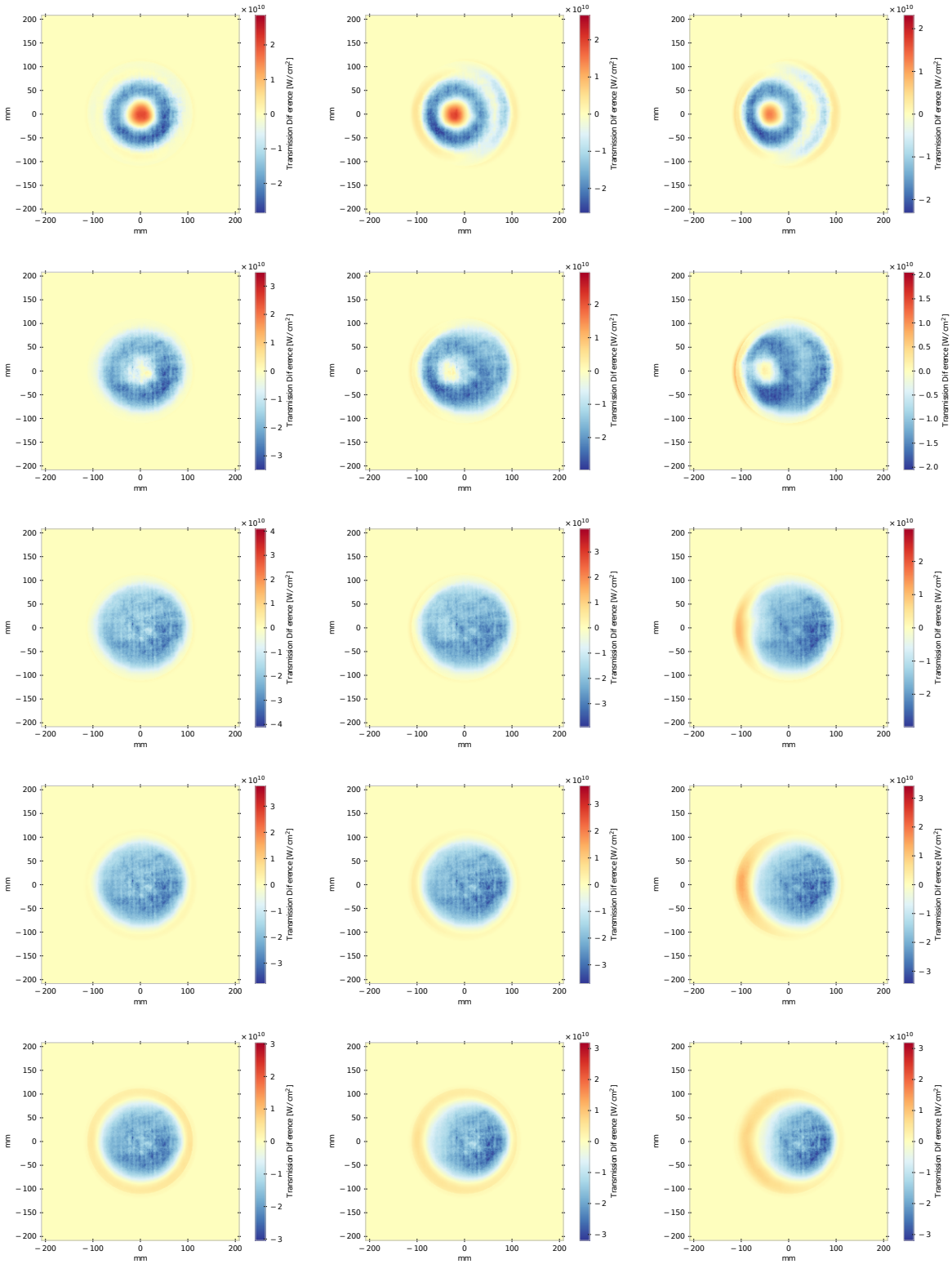

Figure A.3.: **Transmission Images for** $n_0 = 1\,\mathrm{n_c}$

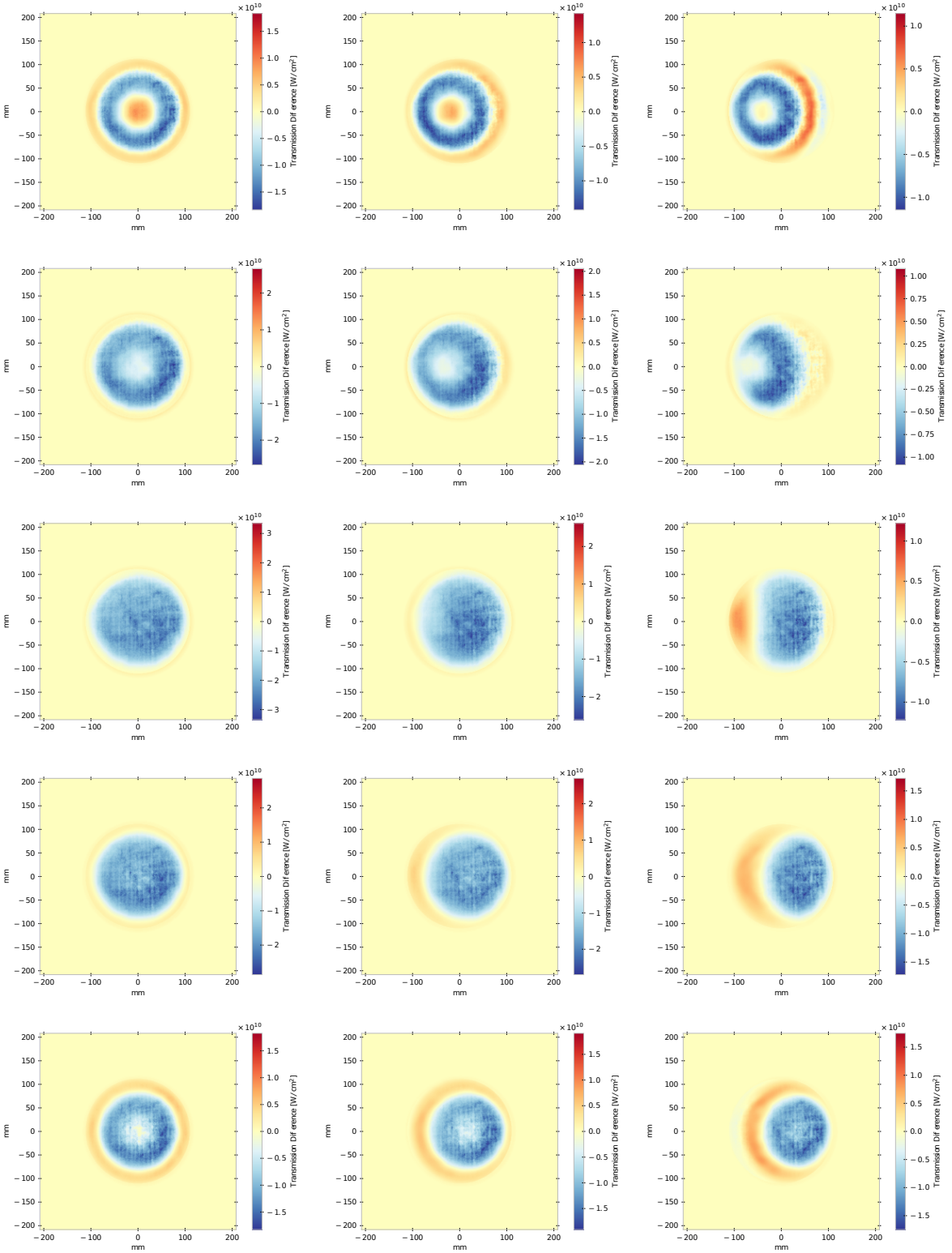

Figure A.4.: **Transmission Images for** $n_0 = 10\,\mathrm{n_c}$

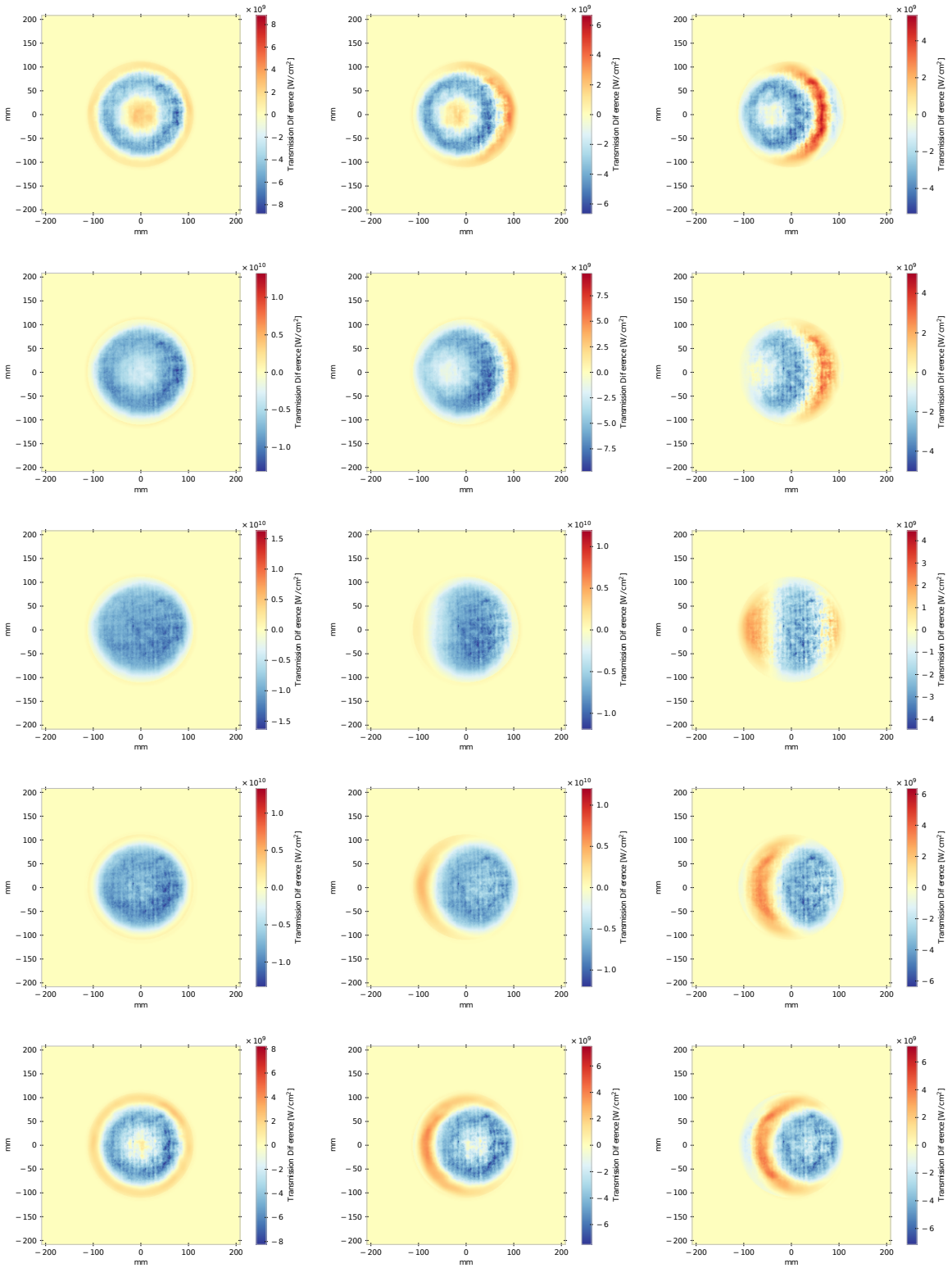

Figure A.5.: **Transmission Images for** $n_0 = 100\,\mathrm{n_c}$

Appendix B.

Detailed Simulation Results

B.1. Without Pre-Pulse

Electron Density and Laser Absorption

In Figure B.1 the lineouts of electron density and heating rate for both laser cases are shown for selected time steps. The top shows the lineouts for the ATLAS-1 parameters, the bottom for PHELIX-1 parameters (for parameter definitions see Table 4.1). The left column are lineouts along the radial dimension at the z = 0 position, the right column along the axial dimension at r = 0.

In both cases a few features typical for a laser impinging on a solid density target can be observed. First, the density steepens around the critical density, because here the laser can no longer penetrate the target. At this point the radiation pressure is balanced by the thermal pressure of the plasma. As a result, a shock forms and travels towards the center of the target. A low density corona forms outside the critical density volume from the plasma flowing quickly outward. This ablation increases the pressure towards the target center and aids in forming and maintaining the shock.

On the plasma front side the critical surface quickly expands over the first few ps but then stagnates, having achieved a balance between the thermal pressure of the plasma acting outward and radiation and ablation pressure of the incident laser acting towards the center.

In the PHELIX case the plasma diffuses below the critical density after $t \approx -20\,\mathrm{ps}$, becoming transparent to the laser. Subsequently, the peak density falls rapidly over these last 20 ps to less than $1\,\%\mathrm{n_c}$. At this point the plasma is nearly homogeneously distributed over the simulation volume.

In the laser heating rate (Figure B.1) the laser penetration into the target is clearly visible. The absorption peaks sharply at the critical density, as expected. For the PHELIX parameters it is also visible how the density falling below the critical density leads to a transparent target with significantly reduced absorption. It should be noted

that already at $-20\,\mathrm{ps}$ the laser has surpassed an intensity of $10^{16}\,\mathrm{W/cm^2}$ where the simulation approach is no longer applicable. This is discussed in more detail later.

Temperature and Ionization

Figure B.2 displays the temperature of the plasma and reveals that the part where the density is below the critical density with the laser penetrating is quickly heated to a uniform temperature above 100 eV. The highly dense part of the plasma is heated more slowly and stays at a core temperature of $\sim 10\,\mathrm{eV}$ over tens of ps.

The mean charge state (also Figure B.2) follows closely the temperature evolution as dictated by the Saha equation. It should be noted that the ionization in the highly overdense volume of the plasma only reaches a value of 3. This means that the strong increase of the density compared to the initial density is mainly due to a traveling shock wave and not due to additional ionization.

Fluid Velocity

As can already be seen in the density distributions, the plasma exhibits an ablation front and a shock traveling into the plasma. The structure of the ablation and the shock can be seen even more clearly in the velocity distribution. As an example, the velocity map of the ATLAS simulation case for the time $t = -15\,\mathrm{ps}$ is shown in the top of Figure B.3. The fluid elements outside the ablation front flow rapidly away from the target, with increasing velocity the lower the density is. This is particularly pronounced on the laser irradiated side of the target, where the ablation front forms a half-sphere with $\sim 0.4\,\mu\mathrm{m}$ radius. On the ablation front, the velocity changes direction and a $\sim 0.1\,\mu\mathrm{m}$ thin shell travels towards the center of the plasma, creating the shock. This behavior is maintained until the shock reaches the center of the target. After this point, all fluid elements flow outward and the density decreases rapidly.

The two lower rows of Figure B.3 show lineouts of the radial and axial velocity components along the respective axis. The inversion of the velocity direction at the ablation front is clearly visible for both components and also on the side of the plasma that is downstream of the laser. At the same time, the velocity of the out-flowing plasma is only increasing marginally up to nearly $1\,\mu\mathrm{m/ps}$. At late times in the PHELIX case, the shock has traversed the target center and the velocity starts to follow a step-like form, with the zero-crossing at the target center of mass. This also nicely visualizes how the target center of mass shifts over time, due to the pressure imbalance by the additional radiation pressure of the laser on the target front surface and higher ablation pressure

due to the one-sided heating.

B.2. With Pre-Pulse

When including the short pre-pulses with parameters identical to the expansion model and starting the simulation at the onset of the pre-pulse, the initial plasma dynamics are significantly altered. The temporal profile of the pulse is modeled as the sum of a single pre-pulse, a constant ASE pedestal and the exponentially rising edge, which is identical to the case without pre-pulse. This profile is shown in Figure 4.3**a**, where the dotted lines indicate the time, at which the simulations without pre-pulse start. The simulation results at late times $t \gtrsim -20\,\mathrm{ps}$ for the PHELIX case are again not trustworthy, as the intensity becomes too large for the code to correctly represent the interaction.

The immediate effect of the pre-pulse is to nearly instantaneously heat the target front locally and launch a shock wave into the target. This can be seen in the electron density lineouts in Figure B.4. The temperature lineouts also reveal that the temperature spike travels through the target in unison with the density shock. So, apart from the front, the target remains relatively undisturbed and does not expand significantly and nearly all of the absorbed energy is contained in the shock. During irradiation by the ASE at rather low intensity, the shock slowly travels through the target, dissipating its energy into the bulk. As the pre-pulse at PHELIX contains fifteen times more energy than the ATLAS, the shock velocity and temperature are higher by a factor of ~ 4 and the target front side expands faster than in the ATLAS-2 case. This results in a saw-tooth like density distribution in the logarithmic plot, i.e. an undisturbed target back side and an exponential fall in density on the front side in the PHELIX-2 case.

With the onset of the rising edge the dynamics change in both cases. The shock amplitude increases due to increasing ablation pressure and the target is heated throughout the complete volume. Driven by this rise in temperature the back side starts to expand significantly, while on the front side the critical density surface is balanced by the ablation and radiation pressure of the interaction. As the shock in the PHELIX case has nearly passed through the target by the time the rising edge becomes relevant, the center of mass of the newly rising density is located about 0.5 µm downstream of the initial target position, having moved effectively the complete target bulk. In the case of the ATLAS parameters, the shift is less, due to the slower shock velocity and the generally lower energy contained in the laser.

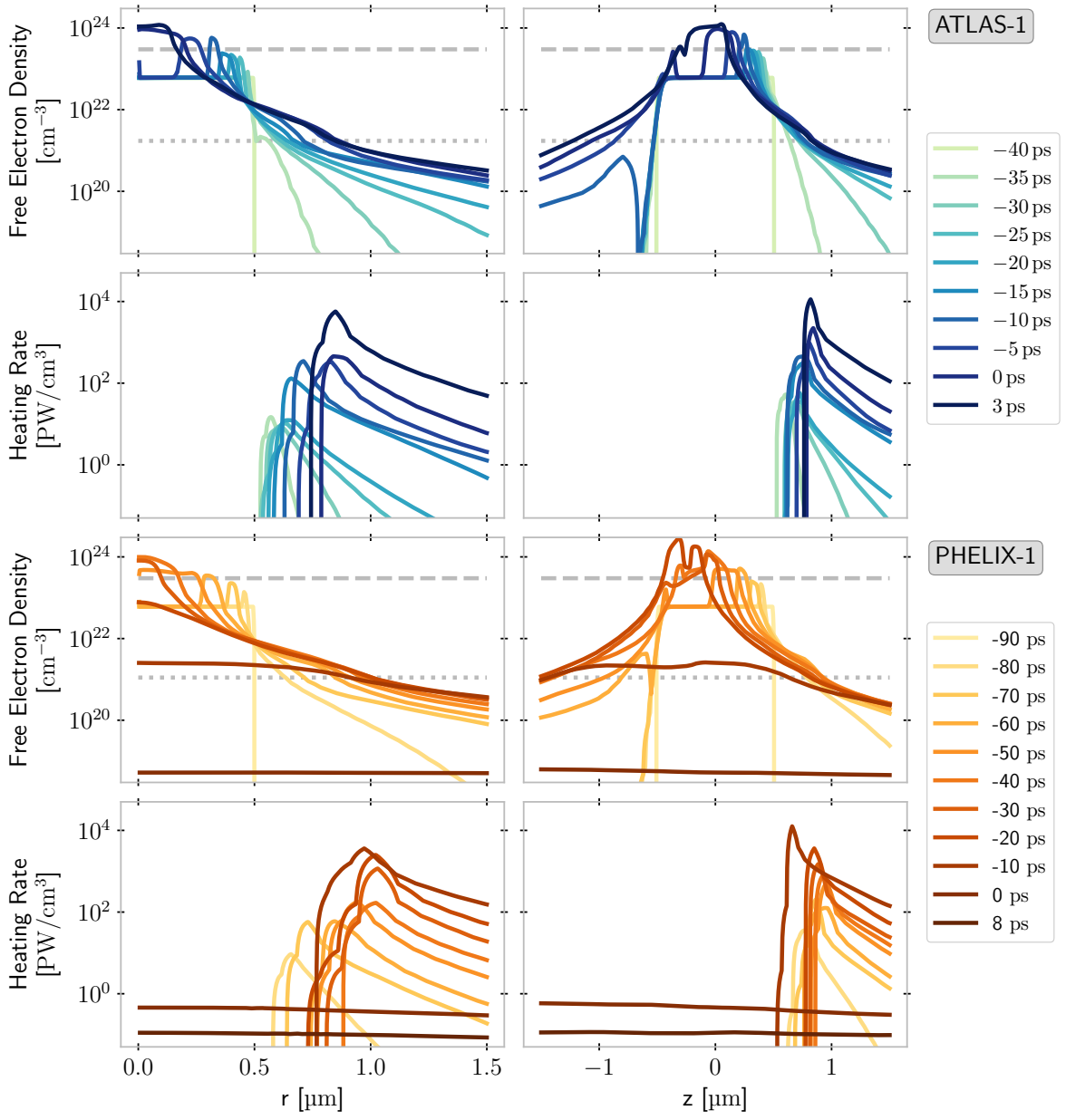

Figure B.1.: **Electron Density and Heating Rate Lineouts Without Pre-Pulse** Lineouts of the free electron density and laser heating rate taken along the radial (left) and axial (right) coordinate for the ATLAS-1 (green-blue) and PHELIX-1 (orange-brown) simulations at each time step. The dashed gray line corresponds to the free electron density of a fully ionized plasma at solid density, the dotted line marks the critical density.

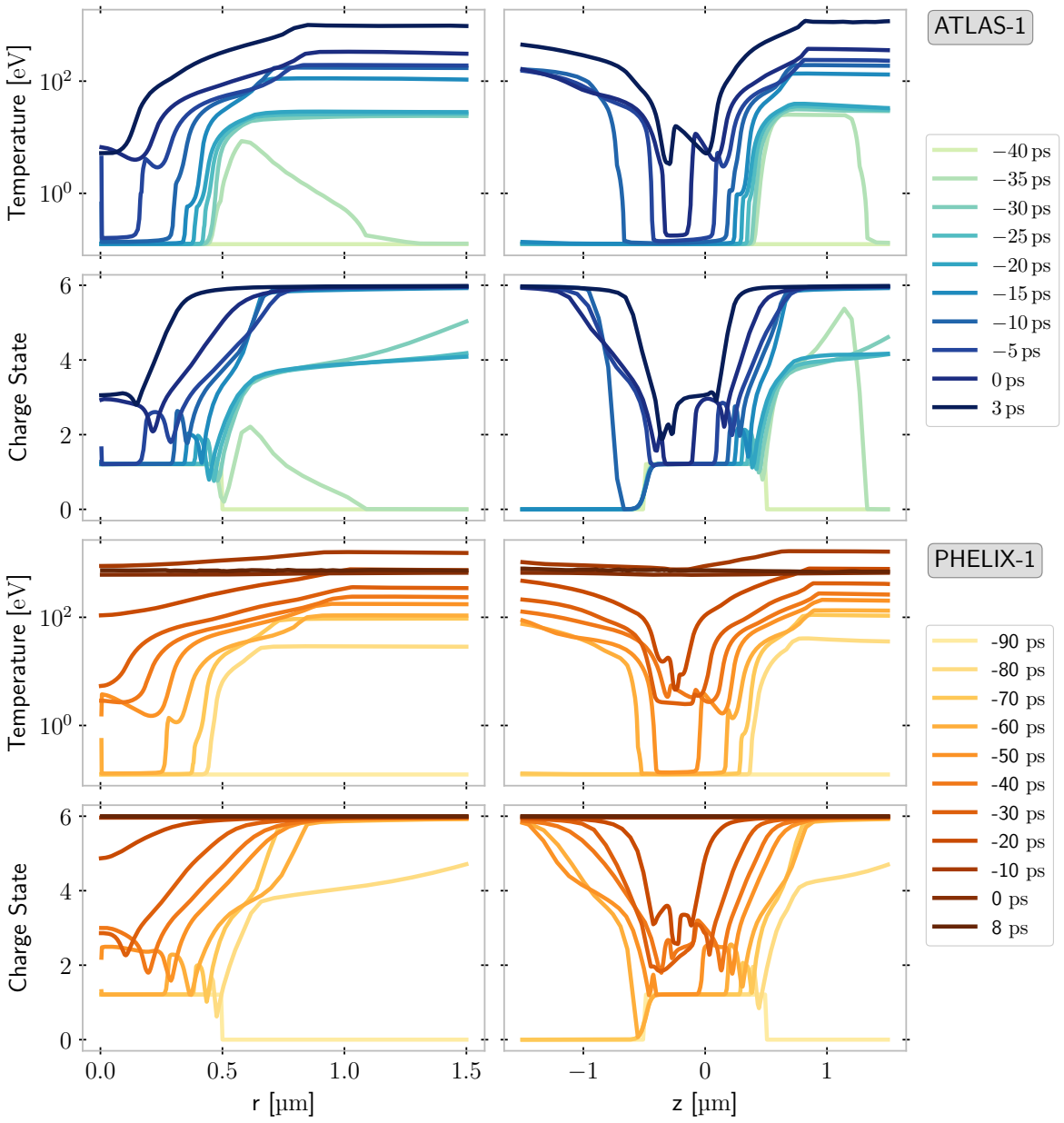

Figure B.2.: **Electron Temperature and Mean Charge State Lineouts without Pre-Pulse**
Lineouts of the electron temperature and mean charge state taken along the radial (left) and axial (right) coordinate for the ATLAS-1 (green-blue) and PHELIX-1 (orange-brown) simulations at each time step.

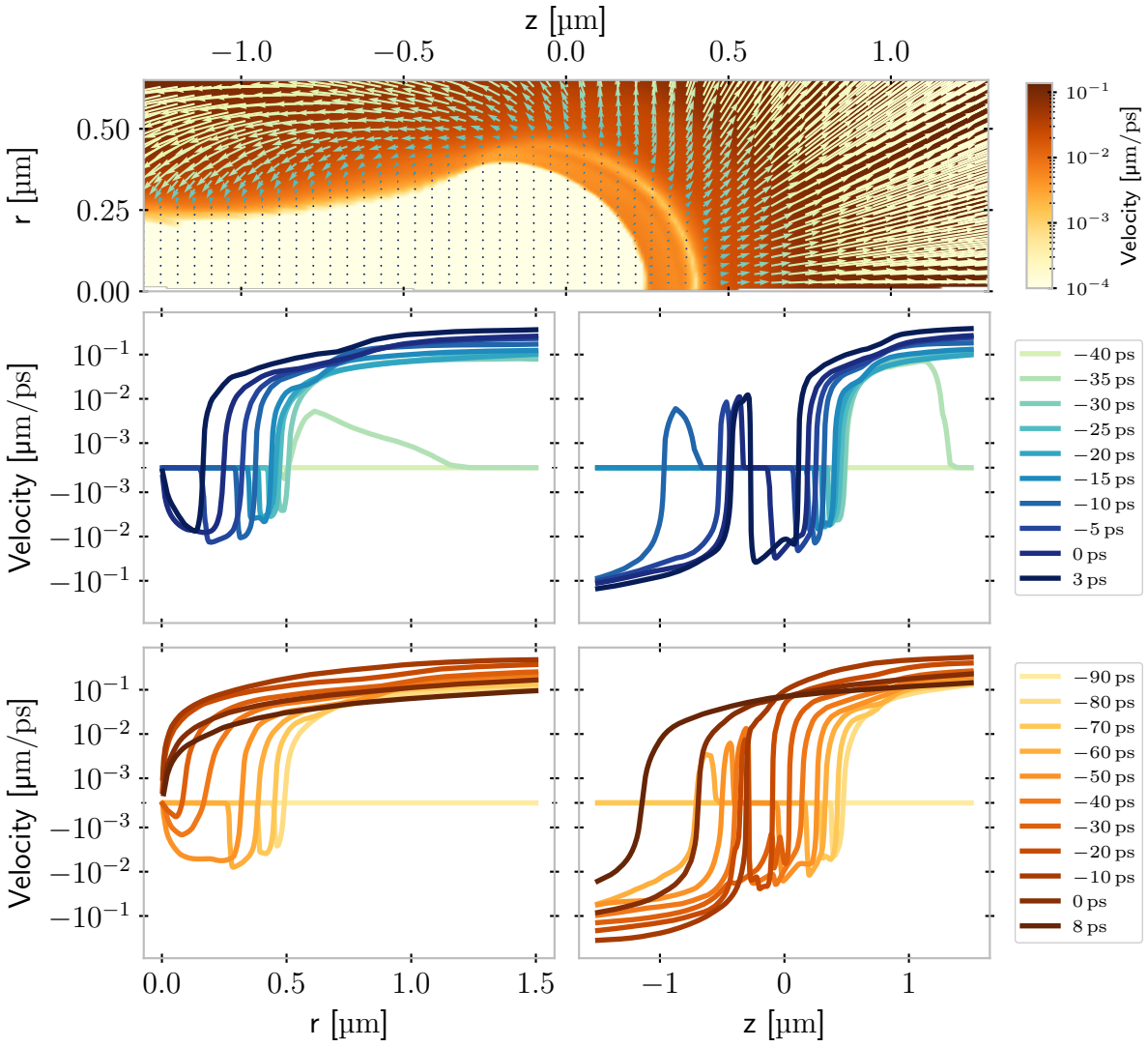

Figure B.3.: **Fluid Velocity**
Map of the fluid velocity at $t = -15\,\mathrm{ps}$ (top) and lineouts of the velocity (lower two rows) along the radial (left) and axial (right) axis for multiple points during the simulation. The green-blue lineouts correspond to ATLAS-1 parameters, the orange-brown lineouts to PHELIX-1 parameters.

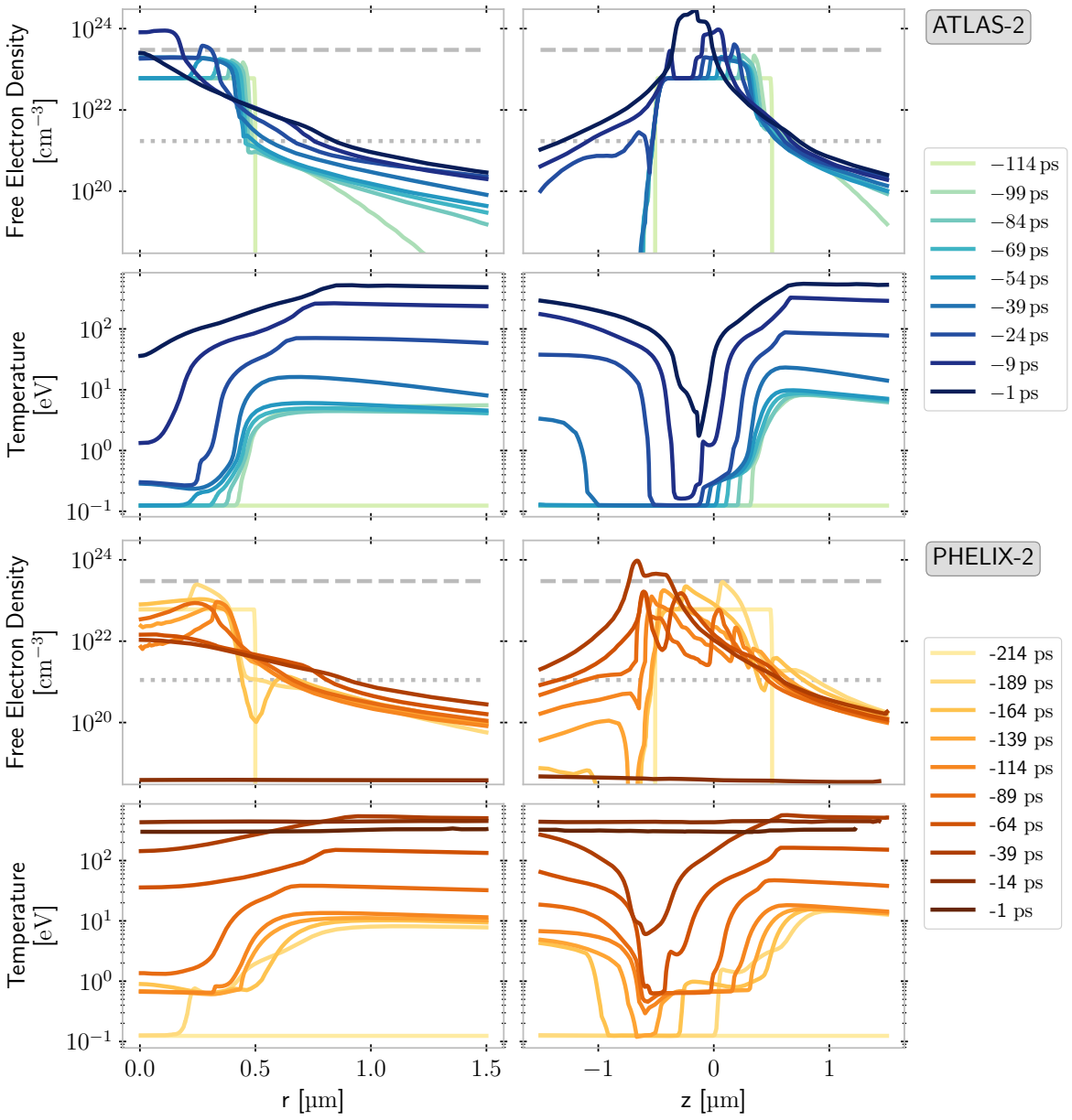

Figure B.4.: **Electron Density and Temperature Lineouts with Pre-Pulse** Lineouts of the electron density and plasma temperature along the radial (left) and axial (right) coordinate for the ATLAS-2 (left, green-blue) and PHELIX-2 (right, orange-brown) simulation cases at selected time steps. The gray dashed and dotted lines in the electron density plots correspond to the solid and critical density respectively.

Acknowledgments

Finally, I want to thank everyone who supported and guided me during my PhD journey. First and foremost I want to thank Jörg for the many hours of fruitful discussions and for not showing his doubts in my experiments. Without his guidance this thesis would not have been possible. He always encouraged me to follow my own ideas while keeping me on track.

I am also very grateful to the recent AG Schreiber alumni, Johannes, Martin, Jens, and Thomas, for teaching me how to do ion acceleration experiments and basically everything I know, already since my Masters thesis. Jo and Martin finally were the ones to snare me in the 'trap', so that I continued working on it for my PhD.

Next I want to thank the I-BEAT family, Sonja and Anna, for a great first PhD year with lots of fun during our Covid beamtimes in Dresden and Darmstadt. Anna in particular I want to thank for being a great first Master student and for keeping the infamous ZEUS humor alive also in her PhD. Sonja has been a great support throughout, from our time as 'I-BEAT parents' over our first 'young and wild' beamtimes up to the points where I was doubting the whole endeavor. I am very thankful for her support.

Our LION 'DÄD' Lenny was always a great support in all aspects, from optics over electronics to software development. And of course he taught me the Tango. He is really the Jack of all trades.

Further, I also want to thank the next generation of I-BEATs, Alex and Julia, as well as the Mäuse, Michi and Flo, and Lianren for their support during my beamtimes. They made the many long nights a fun experience.

The members of our sister cave in HF, Laura, Max, Erin-Grace, and of course Peter, I want to thank for many interesting discussions and widening my horizon beyond protons.

I also thank Anna Tauschwitz for performing the RALEF simulations and helping with their interpretation.

Of course, this thesis would not have been possible without the incredible support by our technical team. Nik and Olli were always happy to advice and lend a hand for everything related to vacuum and optics. And without the relentless work of Flo Saran and Hans Wirth the CALA facility would break apart in weeks. I am particularly grateful to our laser god Gregor for everything he did for me and us. For his patience when

teaching how to turn on and operate the laser, his support in implementing changes, and his fast and efficient problem solving whenever something went wrong. I also thank everyone in the mechanical workshop, in particular Rolf Öhm and Stefan Rößl, for their help and patience when I was learning mechanical design and their flexibility with short term alterations.

I also want to thank all the great students I had the pleasure of supervising, Anna, Ferdinand, Moritz, Vinay, and Christine, for their incredible work and support with my experiments. I was very lucky to have such great students.

Besides the members of the chair I want to thank my writing group, Philipp, Clara, Julia, and Lena, for going through the final phase with me and keeping up my motivation and productivity. Without our days in the library, the writing would have taken twice as long.

Finally I want to thank my family for supporting me through my studies and enabling me to make it as far as I have. And I thank my girlfriend Simone for making sure I have enough balance to my work and always having my back when things were tough.